

QUANTUM DOT ROLLED-UP MICROTUBE AND EDGE EMITTING LASERS

by

Sishir Bhowmick

A dissertation submitted in partial fulfillment
of the requirements for the degree of
Doctor of Philosophy
(Electrical Engineering)
in The University of Michigan
2013

Doctoral Committee:

Professor Pallab K. Bhattacharya, Chair
Professor L. Jay Guo
Professor Jamie D. Phillips
Associate Professor Kevin P. Pipe

© Sishir Bhowmick 2013
All Rights Reserved

DEDICATION

To my mother

ACKNOWLEDGMENT

First of all, I would like to express my gratitude to my parents and the rest of my family for their love and support throughout my life. I would like to express my sincere gratitude to my thesis advisor Prof. Pallab Bhattacharya, for giving me the opportunity to work on cutting-edge research. The thesis would not have been possible without him. His unique way of handling challenges and sheer persistence has been and will remain as a constant source of inspiration for the rest of my life. I also want to thank other members of my doctoral committee: Professors L. Jay Guo, Kevin Pipe, and Jamie Phillips, for their time, insightful comments, and valuable suggestions.

I would like to thank Dr. Guan Huang, Dr. Debashish Basu, Dr. Wei Guo and Dr. Chi-sen Lee, and Dr. Junseok Heo for their help in getting me acquainted with epitaxial growth, device fabrication and characterization. I am also thankful to Dr. Ayan Das, Dr. Hyun Kum, and Dr. Meng Zhang for their constant support. I would like to mention Shafat Jahangir, my roommate for the whole time. We shared a lot of good time together and I wish him success in his life. I am thankful Animesh Banerjee, Thomas Frost and Jimmy Chen for their support on both technical and non technical matters. I would like to extend my gratitude to Saniya Deshpande, Bo Xiao, Ethan Stark and Zunaid Baten for their cooperation..

Excellent support of the Lurie nanofabrication facility staffs is greatly appreciated. My special thanks to Dennis Schweiger whose generous help and cheerful

demeanor have helped me come out of many difficult situations. I would also like to thank Dennis Grimard, Greg Allion, David Sebastian, Antony Sebastian, Russ Clifford, Matthew Oonk, Sandrine Martin and Pilar Herrera-Fierro for their mentorship and help in device fabrication.

I would like to extend my gratitude to Lisa Vogel, Melanie Caughey, Laura Jarels, Frances Doman, Deb Swartz, and Beth Stalnaker for administrative support throughout my graduate career. I wish to acknowledge the Air Force Office of Scientific Research (AFOSR), the National Science Foundation (NSF), and KAUST for funding this research.

TABLE OF CONTENTS

DEDICATION	ii
ACKNOWLEDGMENT	iii
LIST OF FIGURES	viii
LIST OF TABLES	xiv
LIST OF APPENDICES	xv
ABSTRACT	xvi
CHAPTER	
I. INTRODUCTION	1
1.1 Optical Interconnects	2
1.2 Properties of Quantum Dots.....	3
1.3 Quantum Dot Laser.....	6
1.3.1 Tunnel Injection and P-doping in Quantum Dot Lasers – Physics and Technology	7
1.4 Objective of the Thesis	10
1.5 Dissertation Overview	14
II. MBE GROWTH OF SELF-ORGANIZED QUANTUM DOTS	17
2.1 Stranski-Krastanaw Growth of Self-Organized Quantum dots.....	17
2.2 Growth and Optimization of InAs Quantum Dots on GaAs Substrate.....	20
2.2.1 Effect of Temperature	21
2.2.2 Effect of V/III Ratio.....	23
2.3 Growth and Optimization of InAs/ $\text{In}_{0.53}\text{Al}_{0.24}\text{Ga}_{0.23}\text{As}/\text{InP}$ Quantum Dots.....	24
2.3.1 Effect of Temperature	26
2.3.2 Effect of V/III Ratio.....	27
2.4 Growth InAs/GaAs of Quantum Rings.....	31
2.4.1 Application of Quantum Rings in Intersubband Photodetectors.....	33
2.4.1 Quantum Ring Intersubband Detectors for the 1-3 THz Range.....	35

2.5 Summary	44
III. THRESHOLD CHARACTERISTICS OF ROLLED-UP MICROTUBE LASER	46
3.1 Introduction	46
3.2 Experimental	49
3.3.1 Device Heterostructure and Fabrication	49
3.3.2 Spectral Emission Characteristics and Modal Behavior	51
3.3 Lasing Characteristics, Modal Gain and Threshold Condition	54
3.3.1 Modal Gain	55
3.3.2 Bending Loss	58
3.3.3 Radiation Loss	58
3.3.4 Substrate Loss	60
3.3.5 Dependence of Threshold on Diameter	64
3.4 Summary	65
IV. ROLLED-UP MICROTUBE DIRECTIONAL COUPLER	66
4.1 Introduction	66
4.2 Device Heterostructure and Fabrication	68
4.3 Directional Coupler Characteristics	70
4.4 Liquid Sensing Application	72
4.5 Summary	74
V. ROLLED-UP MICROTUBE PHOTOTRANSCEIVER	75
4.1 Introduction	75
4.2 Device Heterostructure and Fabrication	76
4.3 Experimental Results	79
4.5 Summary	83
VI. HIGH PERFORMANCE $\text{InAs/In}_{0.53}\text{Ga}_{0.23}\text{Al}_{0.24}\text{As/InP}$ QUANTUM DOT $1.55\ \mu\text{M}$ TUNNEL INJECTION LASER	84
6.1 Introduction	84
6.2 Epitaxial Growth and Fabrication of QD Lasers	89
6.3 Results and Discussion	92
6.3.1 Statics Characteristics	92
6.3.2 Dynamic Characteristics	96
6.4 Summary	103
VII. CONCLUSION AND SUGGESTIONS FOR FUTURE WORK	105
7.1 Summary of the Present Work	105
7.2 Suggestion for the Future Work	107
7.2.1 Electrically Injected Rolled-up Microtube Laser	107

7.2.2 Investigation of Gain-lever Effect in InAs/In _{0.53} Ga _{0.23} Al _{0.24} As/InP Quantum Dot Laser.....	109
APPENDICES	111
BIBLIOGRAPHY	134

LIST OF FIGURES

Figure

1.1:	Optical network for on-chip and off-chip using dense WDM.....	2
1.2:	Comparison of the energy level of atoms, bulk semiconductors and quantum dots (modified from Ref.[13])	4
1.3:	Density of states (DOS) and electron density $\rho(E)$ versus energy with respect to the conduction band edge for different dimensional structures: (a) bulk (3-D); (b) quantum well (2-D); (c) quantum wire (1-D); and (d) quantum dot (0-D). The shade areas denote carrier densities with identical quasi-Fermi levels. (modified from Ref.[13])	5
1.4:	Schematic tunnel injection scheme. Cold electrons are tunneled into the ground state of the QDs by phonon assisted tunneling	8
1.5:	Schematic illustration of modulation p-doping of the quantum dot.....	9
1.6:	(a) and (b) schematic of the formation of an InGaAs/GaAs microtube on a GaAs substrate; (c) Optical microscopy image of an InGaAs/GaAs microtube formed on GaAs	11
1.7:	(a) Controlled transfer of an InGaAs/GaAs microtube on to the facet of a single mode fiber [44]; (b) schematic of a phototransceiver circuit consisting of an electrically injected microtube laser, a microtube detector and a waveguide connecting them.....	12
1.8:	(a) Threshold current density vs. temperature characteristics of quantum dot lasers [55]; (b) small signal modulation characteristics [56]	14
2.1:	Schematics representation of (a) Frank–van der Merwe (FM) growth mode; (b) Volmer-Weber (V-W) growth mode; (c) Stranski-Krastanov (S-K) growth mode.....	18
2.2:	Test structure for quantum dot calibration. Top quantum dot layer is left uncapped in order to facilitate atomic force microscopy (AFM) imaging	20

2.3:	Atomic force microscopy (AFM) images of the 2.5 monolayer InAs/GaAs quantum dot layers grown at (a) 495 °C; (b) 510 °C; (c) 530 °C with a group V/III ratio of 40.	21
2.4:	Photoluminescence spectra of the InAs/GaAs quantum dots grown at different temperatures with a group V/III ratio of 40.....	22
2.5:	Atomic force microscopy images of the 2.5 monolayer InAs/GaAs quantum dot layers grown at 510 °C; with a group V/III ratio of (a) 35; (b) 40; (c) 45.	23
2.6:	Photoluminescence spectra of the 2.5 monolayer InAs/GaAs quantum dot layers grown at 510 °C with different group V/III ratios..	24
2.7:	Test structure for InAs/In _{0.53} Ga _{0.23} Al _{0.24} As quantum dot calibration. Top quantum dot layer is left uncapped in order to facilitate atomic force microscopy (AFM) imaging.....	25
2.8:	X-ray diffraction image of InAlGaAs layer grown on (001) InP substrate.....	26
2.9:	Atomic force microscopy images of the 5 monolayer InAs/In _{0.53} Ga _{0.23} Al _{0.24} As quantum dot layers grown at (a) 480 °C; (b) 495 °C; (c) 510 °C with a group V/III ratio of 18.....	27
2.10:	Photoluminescence spectra of the InAs/In _{0.53} Ga _{0.23} Al _{0.24} As quantum dots grown at at different temperatures with a group V/III ratio of 18.....	28
2.11:	Atomic force microscopy images of the 5 monolayer InAs/In _{0.53} Ga _{0.23} Al _{0.24} As quantum dot layers grown at 495 °C with group V/III ratio of (a) 13; (b) 18; (c) 23; (d) quantum dots grown with same growth condition but with a 5Å GaAs grown just before the growth of InAs quantum dots.	29
2.12:	Photoluminescence spectra of the InAs/In _{0.53} Ga _{0.23} Al _{0.24} As quantum dots grown at temperature 495 °C with different group V/III ratio.	30
2.13:	Schematic of the formation mechanism of self-organized quantum ring	32
2.14:	AFM image of quantum rings grown by insitu annealing of self-organized quantum dots	32
2.15:	XTEM image of an In(Ga)As quantum ring grown by MBE [99].....	33
2.16:	Schematic band diagram of QD and QR showing a reduced intraband transition energy for the latter	34

2.17:	Photoluminescence spectra of quantum rings and their precursor quantum dots	35
2.18:	(a) AFM image of InAs quantum rings formed by post-epitaxy thermal annealing of quantum dots. Inset shows a magnified image and dimensions; (b) calculated ground state energy in the quantum ring as a function of ring height for ring width $W = 15$ nm. Inset shows the schematic of the quantum ring and calculated bound state in a quantum ring with $W = 15$ nm and $H = 1.25$ nm. The transition energy of 7.89 meV corresponds to 1.91 THz.....	37
2.19:	Heterostructure schematic of QRID grown by MBE. It has 10 layers of InAs quantum rings in the active region and a single $Al_{0.2}Ga_{0.8}As$ barrier at the end; (b) dark current characteristics at two different temperatures (4.2 K and 80 K). Inset shows the conduction band profiles in the active region for forward and reverse bias.....	39
2.20:	Measured spectral responsivity of QRID for (a) different reverse biases measured at 5.2 K, and (b) 1V bias measured at 5.2 K. The inset to (b) shows the responsivity at 10 K under 1 V bias	42
3.1:	(a) Schematic representation of a free-standing rolled-up microtube. The left inset shows heterostructure of device with two layers of InAs quantum dots buried in the GaAs matrix. The bridge part of the microtube is schematically magnified in the right inset. It shows the inside and outside notches and the corrugation at the outside notch; (b) optical microscopy image of a fabricated rolled-up microtube showing the suspended bridge. The scanning electron microscopy (SEM) in the inset shows the corrugation in the bridge region of the microtube.....	47
3.2:	(a) Room-temperature micro-photoluminescence from the as-grown InAs quantum dot bilayers heterostructure; (b) microphotoluminescence spectra of the rolled-up microtube device of diameter ~ 9 μm for different incident powers. Theoretically calculated mode energies indicated in the figure show excellent agreement with the measured data..	50
3.3:	(a) Schematic of the microtube showing the direction of light propagation, E-field and H-field for the azimuthal mode. The calculated mode profile shown in the inset indicates most of the radiation originates from the notches of the microtube; (b) schematic of equivalent planar waveguide near the notch..	52
3.4:	Theoretically calculated modal gain versus carrier density in a InAs quantum dot layer.....	54

3.5:	(a) Schematic cross section of a microtube showing different wall thickness (w_1 and w_2) at different positions along the tube periphery. The r -direction is the outward direction from origin at the center of the ring to the wall and the z -direction is the direction out of the paper; (b) calculated bending loss as a function of diameter for different wall thicknesses.....	57
3.6:	(a) Schematic representation of scattering losses at the step discontinuity of a notch of the microtube; (b) radiation loss as a function of output waveguide thickness.....	59
3.7:	(a) Dependence of the microtube cavity quality factor Q on the separation of the tube from the substrate; (b) substrate loss in the microtube cavity versus separation from substrate. The dashed lines are guides to the eye.....	61
3.8:	Schematics (a) Comparison of radiation loss at a step notch and bending loss in the microtube cavity as a function of tube diameter; (b) calculated threshold gain versus diameter in the microtube laser..	62
3.9:	(a) Output light intensity versus incident pump power for different diameter quantum dot microtube lasers; (b) variation of threshold carrier density in active region of the lasers with microtube diameter.....	63
4.1:	(a) Schematic representation of rolling mechanism; (b) schematic representation of GaAs-based heterostructure and the rolled-up microtube coupler. The heterostructure is grown by MBE and has two layers of InAs quantum dots embedded in the GaAs matrix; (c) scanning electron microscopy (SEM) image of a microtube coupler with the inset showing an enlarged region of the microtubes.....	67
4.2:	Schematic of the measurement procedure. The output objective lens is swept along the z -direction to obtain the luminescence spectra at different positions on the input and coupled microtubes.	69
4.3:	(a) Measured photoluminescence spectra at different positions on the coupled microtube in air; (b) integrated photoluminescence intensity vs. distance on the input and output microtube. Solid lines are calculated intensities using the finite difference time domain technique.....	71
4.4:	Calculated variation of coupling length l_c vs. the microtube separation.	72
4.6:	(a) Measured photoluminescence spectra from coupled microtube at a distance of 25 μm in air and isopropyl alcohol (IPA) as the coupling media. The spectra are displaced arbitrarily along the vertical axis for clarity; (b) integrated photoluminescence intensities vs. distance along the axis of the coupled microtube in air and IPA. Dashed lines are guides to the experimental data	73

5.1:	(a) Schematic of rolled up microtube heterostructure grown by molecular beam epitaxy. Two layers of self-organized InAs quantum dots are contained in the active region; (b) schematic of the monolithically integrated microtube phototransceiver consisting of the laser, photoconductive detector and dielectric waveguide; (c) scanning electron microscope image of the fabricated phototransceiver	77
5.2:	Measured transmission loss in the a-Si/SiO ₂ waveguide for different waveguide lengths	78
5.3:	(a) Measured room temperature photoluminescence spectrum from the as-grown microtube heterostructure; (b) room temperature microphotoluminescence spectra from the rolled-up microtube laser for two different excitation powers. The inset shows the output light intensity of the microtube laser as a function of excitation power.....	80
5.4:	(a) Dark current-voltage characteristics of the microtube detector. Inset shows the photoconductive gain of the microtube detector as a function of bias; (b) variation of photocurrent in the microtube detector as a function of pump power in the microtube laser. Inset shows detector photocurrent due to scattered light in the control OEIC for comparison; (c) variation of photocurrent in the microtube detector for different excitation powers in the microtube laser	82
6.1:	Atomic force microscopy (AFM) image of InAs/In _{0.53} Ga _{0.23} Al _{0.24} As/InP quantum dots grown by molecular beam epitaxy. The dot density is estimated to be $5 \times 10^{10} \text{ cm}^{-2}$	85
6.2:	(a) Schematic of the tunnel injection quantum dot laser heterostructure; (b) calculated mode profile	87
6.3:	Room temperature photoluminescence (PL) spectrum of InAs/In _{0.53} Ga _{0.23} Al _{0.24} As/InP quantum dots; (b) gain spectrum of the quantum dot laser measured from the near-threshold laser spectrum (shown in the inset) using the Hakki-Paoli technique.....	90
6.4:	(a) Measure light-current characteristics of a broad area quantum dot laser. Inset shows the lasing spectrum at $I = 1.3I_{th}$; (b) L-I-V characteristics of a $3 \mu\text{m} \times 390 \mu\text{m}$ ridge-waveguide laser showing the roll-over at high injection	93
6.5:	(a) Threshold current density vs. temperature characteristics of the broad-area quantum dot laser; (b) variation of peak wavelength with temperature for broad area lasers of varying cavity lengths.....	95

6.6:	(a) Measured variation of peak wavelength of broad area lasers with different cavity lengths; (b) variation of inverse differential slope efficiency with cavity length; (c) variation of threshold current with inverse cavity length.....	97
6.7:	Measured small signal modulation response of ridge waveguide tunnel injection quantum dot laser. The solid curves are calculated modulation responses (see text) The -3db modulation bandwidth measured for $I = 67$ mA is 14.4 GHz.....	98
6.8:	Data obtained from analysis of small-signal modulation resonance of QD lasers: (a) variation of damping factor with resonance frequency; (b) variation of resonance frequency with current injection.....	100
6.9:	Measured chirp of quantum dot laser as a function of small-signal modulation frequency; (b) measured α -parameter as a function of emission wavelength.....	102
7.1:	(a) Schematic heterostructure of the electrically injected microtube laser; (b) Schematic of the fabrication mechanism.....	108
7.2:	Schematic of the multisection laser device for gain lever operation.....	111

LIST OF TABLES

Table

2.1:	InAs/GaAs quantum dot properties under different growth conditions.....	24
2.1:	InAs/ $\text{In}_{0.53}\text{Al}_{0.24}\text{Ga}_{0.23}\text{As}$ /InP quantum dot properties under different growth conditions.....	31
7.1:	Calculation of threshold carrier densities from excitation power.....	64

LIST OF APPENDICES

Appendix

A:	Measurement Setups	111
	A1: Photoluminescence Measurement Setup	111
	A2: Laser Current-Voltage Characteristics Measurement Setup	113
	A3: Laser L-I Measurement Setup	114
	A4: Small Signal Modulation Measurement: Scheme 1	115
	A5: Small Signal Modulation Measurement: Scheme 2	116
	A6: Laser Spectrum, Gain and Chirp Measurement Setup	117
	A7: Far Field Measurement Setup.....	118
B:	Quantum Dot Ridge Waveguide Laser Processing	119
C:	MATLAB Code for Waveguide Modes and Confinement Factor.....	127

ABSTRACT

Infrared lasers emitting at 1.3 and 1.55 μm are the workhorses for fiber optic communication. Commercial lasers used at these wavelengths are generally GaAs and InP based quantum well lasers which suffer from undesirable characteristics including higher threshold, limited small-signal modulation bandwidth and most notably poor temperature stability. Due to their unique optoelectronic properties, lasers incorporating quantum dots can have superior characteristics compared with those incorporating equivalent quantum wells. The three-dimensional confinement of carriers in the quantum dots produces an atomic-like density of states which results in better temperature stability, chirp-free high speed operation, and higher modulation bandwidth in the lasers and therefore makes them a favorable candidate for practical applications.

A novel InAs/GaAs quantum dot rolled-up microtube laser formed by an epitaxial strain-driven mechanism has been investigated. The spectral output has been analyzed and is understood in the framework of mode confinement and scattering at the corrugated regions at the notches and mode propagation as in a cylindrical ring resonator. Simplified analytical expressions have been derived for the scattering (radiation) loss at the microtube notches, the bending loss, and the substrate loss and their values have been calculated as a function of tube diameter. The threshold condition for a microtube laser has been derived from which it is found that the threshold excitation (power) is inversely proportional to the microtube diameter.

A rolled-up microtube active directional coupler made of twin microtubes is demonstrated. The microtube is made of an InGaAs/GaAs strained bilayer with InAs self-organized quantum dots inserted in the GaAs layer. The directional coupler can work in both active and passive modes and therefore can be excited with light of any wavelength. The coupling characteristics have also been measured in isopropyl alcohol, instead of air, as the surrounding media to demonstrate the potential of the device as a sensor.

A quantum dot rolled-up microtube optoelectronic integrated circuit operating as a phototransceiver has been demonstrated. The phototransceiver consists of an optically pumped microtube laser and a microtube photoconductive detector connected by a Si/SiO₂ waveguide. The rolled-up microtube detector exhibits a very low dark current of 9 μ A for a bias of 5V and the maximum responsivity of the phototransceiver circuit is 34 mA/W.

To extend the advantage of quantum dots to 1.55 μ m, the growth of self-organized InAs quantum dots on In_{0.53}Ga_{0.23}Al_{0.24}As/InP has been investigated. Quantum dot lasers incorporating modulation p-doping of the active region and a tunnel injection structure for electrons operating at 1.56 μ m have been demonstrated. The lasers are characterized by high temperature stability with characteristics temperature $T_0 = 227$ K and 100 K for the temperature range $5^\circ\text{C} \leq T \leq 45^\circ\text{C}$ and $45^\circ\text{C} < T \leq 75^\circ\text{C}$, respectively. The modal gain per dot layer is 14.5 cm^{-1} and the differential gain derived from both light-current and small-signal modulation measurements is $\sim 0.8 \times 10^{-15}\text{ cm}^2$. The maximum measured -3 dB small-signal modulation bandwidth is 14.4 GHz and the gain compression factor is $5.42 \times 10^{-17}\text{ cm}^2$. The lasers exhibit a very small chirp of 0.6 \AA for a modulation frequency of 10 GHz and a near zero α -parameter at the peak of the laser emission.

Chapter I

Introduction

Next generation computing and communication systems require small weight and volume and power dissipation to follow Moore's law which predicts that the number of components on a chip doubles approximately in two years [1]. In order to sustain the aggressive scaling, modern computer chip designs are now focused on multi-core design rather than increasing the clock speed. However, this cannot continue indefinitely because of the complexity of the architecture, time delay and cross talk associated with the metal interconnects. A potential solution to this problem is a combination of both electronic and photonic components on the chip where electronic elements are used for processing and control applications while photonic devices are used in transmission and sensing. This potential has fueled continued interest in the field of silicon photonics [2-5]. Since silicon is an indirect bandgap material and hence has poor light emitting properties, on-chip optoelectronic components need to be integrated on silicon with efficient and cost effective manner. This requirement imposes urgency on developing a high performance coherent light source which can be integrated on Si. Such a light source is essential for optical interconnects [6, 7] in 2-D and 3-D complementary metal oxide semiconductor (CMOS) electronic circuits, which would eliminate crosstalk and RC signal delays and enable high-speed data transfer across a chip as well as for long distance analog and digital optical communication links using fiber optics. Furthermore,

an integrated laser is a core component in the emerging “lab on a chip” technologies where detection of chemical and biochemical species are accomplished by optical signal processing [8].

1.1 Optical Interconnects

Fiber optic communication links have replaced electrical wires due to their ability to deliver higher data rates over longer distances. The initial driving force for the introduction of the optical fiber link was the need for increased bandwidth for interactive multimedia services, which have strained the capacity of traditional wired networks limited by capacitive time delay and crosstalk. Optical signals have gradually penetrated

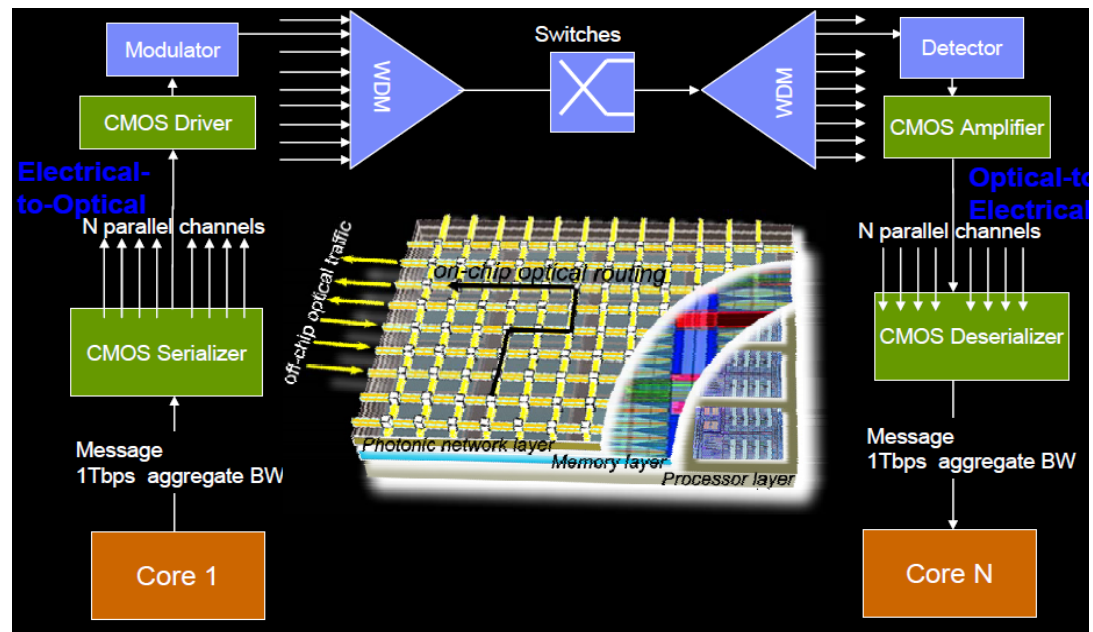


Figure 1.1: Optical network for on-chip and off-chip using dense WDM.

into home networks, personal computers, and consumer electronics, represented by FTTH (fiber-to-the-home) services and S/PDIF (Sony/Philips digital interconnect

format) digital audio format. On the other hand, as a result of the incorporation of the multi-core architecture in state of the art microprocessor chips, there is an urgent need for large bandwidth (exceeding 200 GB/s) in the CPU for high-end applications. A large bandwidth in excess of 100 GB/s is also required for memory applications. Electrical interconnects are rapidly becoming non-suitable to provide that large bandwidth required for those applications [9, 10]. To overcome this bottleneck, optical interconnects are being actively investigated as a potential solution to address the limitations of electrical interconnects. For example, IBM proposed a future 3D-integrated chip consisting of several layers, as illustrated in Fig. 1.1. In this device, the photonic layer is responsible for providing point-to-point broad bandwidth optical links between different cores and off-chip traffic. The most important part of the optical interconnect network on chip is the light source with high performance and low cost. Semiconductor lasers and light emitting diodes (LEDs) are deemed to be highly desirable sources by virtue of their compactness and amenability to integration into dense arrays.

1.2 Properties of Quantum Dots

Lasers with low dimensional quantum confined heterostructures such as quantum wells (QWs), quantum wires and quantum dots (QDs) in the active region have higher gain and differential gain due to their altered density of states. For these reasons, in theory, lower dimension heterostructures should be more favorable in the active region of the laser. The success of two-dimensional quantum well lasers [11, 12] generated interest in lower-dimensional heterostructures, i.e., quantum wires and quantum dots. The schematic energy level in atoms, bulk semiconductors and quantum dots is shown in

Fig 1.2. In bulk semiconductor material, broad energy bands with allowed states, enable the transition/or scattering of carriers in the energy range comparable to the lattice temperature (~ 26 meV at 300 K) via lattice vibration (phonon). The tails of the carrier distribution which are determined by the product of Fermi-Dirac distribution and the

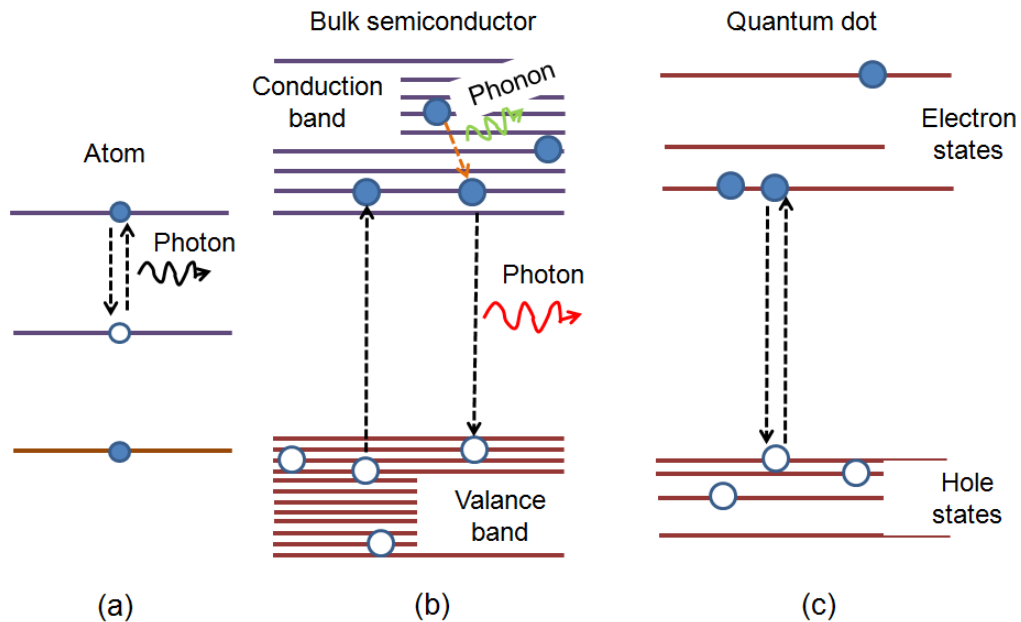


Figure 1.2 Comparison of the energy level of atoms, bulk semiconductors and quantum dots (modified from Ref.[13]).

density of states, approach zero near the conduction and valence band edges and have a peak $(1/2) \cdot kT$ into the conduction band and valance bands. The absence of carrier near the band edge decreases the gain and is responsible for the degraded performance of the bulk active region lasers. In addition, hot-carrier effects such as Auger recombination, temperature dependence of the threshold current, and frequency chirp are also direct consequences of the presence of energy bands. In quantum dots, the energy spectra exhibit discrete levels instead of bands. It is similar to the electron energy quantization in atoms. Therefore, quantum dots could be imagined as artificial atoms. As illustrated in

Fig.1.3, the DOS would remarkably increase and become less temperature dependent with dimensionality reduction. QDs provide the most desirable characteristics of atom-like discrete energy levels with delta-function DOS and efficient overlap of electron-hole

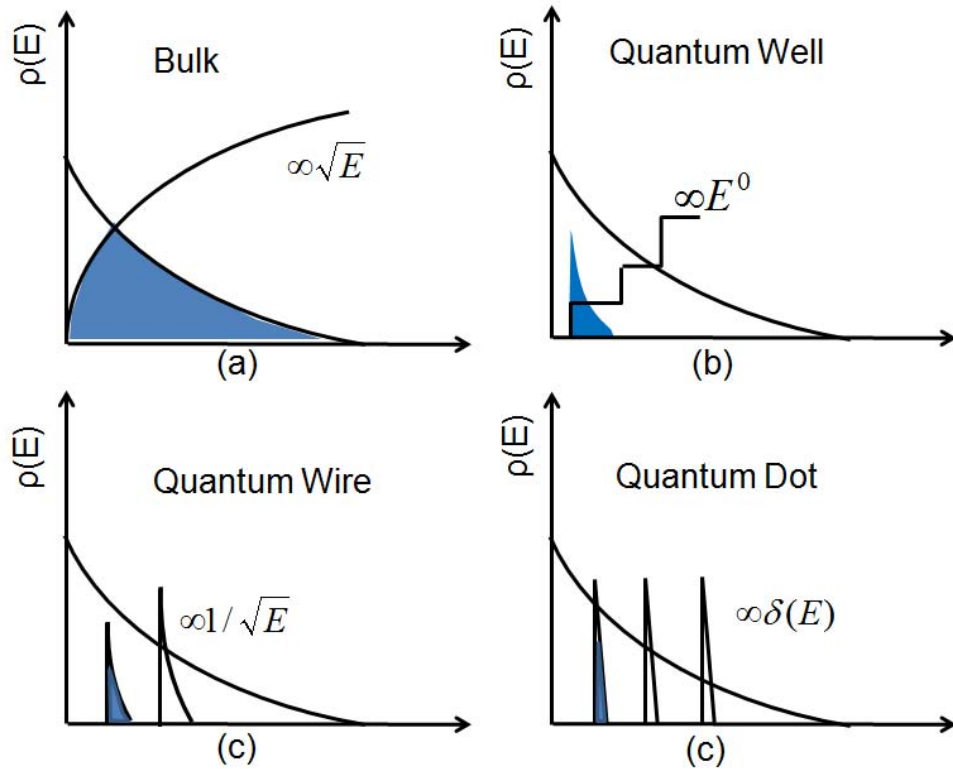


Figure 1.3 Density of states (DOS) and electron density $\rho(E)$ versus energy with respect to the conduction band edge for different dimensional structures: (a) bulk (3-D); (b) quantum well (2-D); (c) quantum wire (1-D); and (d) quantum dot (0-D). The shade areas denote carrier densities with identical quasi-Fermi levels. (modified from Ref.[13]).

wavefunctions [14-16]. These advantages provide QD optoelectronic devices significant performance advantages and unique characteristics [13]:

- 1) High DOS and efficient overlap of carrier wavefunctions give rise to high gain and high differential gain in QD lasers;

- 2) Large gain and differential gain enable low threshold current density, J_{th} , and large output power;
- 3) Large differential gain also allows for higher modulation frequency for extremely high speed operation, low linewidth enhancement factor α , and low/no dynamic chirp;
- 4) Discrete energy spectrum reduces phonon scattering for high temperature stability;
- 5) Higher tolerance for defects and radiation due to electron and hole localization;
- 6) Tunable wavelength of emission and absorption by changing QD size reduces dependence on materials (heterostructure bandgaps).

1.3 Quantum Dot Laser

Quantum dot (QD) lasers have been expected to outperform bulk, quantum well (QW) and quantum wire lasers since the first theoretical predication and experimental demonstration by Arakawa and Sakaki in 1982 [14]. Due to the three-dimensional quantum confinement of the electrons and holes in a quantum dot with size equal to or below the exciton Bohr radius, semiconductor lasers with quantum dot active regions are expected to have a low threshold current density [17-19], high characteristic temperature [20-21], high material gain [17], and large modulation bandwidth [22].

The first electrically injected edge-emitting quantum dot laser was demonstrated in 1994 using self-assembled quantum dots in the active region [23]. The laser was an AlGaAs/GaAs GRIN-SCH laser with 1-mm-long cavity length, its threshold current density is 120 A/cm^2 at 77 K. The characteristic temperature is 350 K between 50 and 120 K. Bhattacharya's group at the University of Michigan was one of the first groups to report room temperature operation and the modulation properties of QD lasers [24, 25].

Significant progress on the performance of quantum dot lasers has been made since then. In 1999, quantum dot lasers crossed a significant milestone by achieving lower threshold current density than the state of the art quantum well lasers [26]. The threshold current density was only 26 A/cm². In 2004, Fathpour et. al used p-doped quantum dots to obtain an nearly temperature insensitive ($T_0 = \infty$) quantum dot laser characteristics in the temperature range from 5 to 75°C [21]. As a result, quantum dot lasers have become a candidate for practical laser applications.

1.3.1 Tunnel Injection and p-doping in Quantum Dot Lasers – Physics and Technology

Bhattacharya, et al. first conceptualized the tunnel injection scheme in semiconductor lasers to alleviate the hot carrier problem, enhance modulation bandwidth, and demonstrated for the first time with quantum well lasers [27]. In the case of self-organized QDs which are formed on a two-dimensional wetting layer during epitaxy [28], the wetting layer and the localized QD states form an electronically coupled system. At room temperature, the injected electrons predominantly reside in the wetting layer due to its much higher number of available states, and the system cannot be described by equilibrium quasi-Fermi statistics [29]. This leads to a hot carrier problem in QD lasers, inducing gain compression and degrading high-speed performance [30-32]. The hot carrier distribution also increases undesirable parasitic recombination outside of the QDs [33, 34], resulting in increased temperature dependence of the threshold current and output slope efficiency.

This problem can be alleviated by tunneling “cold” electrons into the lasing

states of quantum-well/dots from an adjacent injector layer, as shown in Fig. 1.4. Using this technique, cold carriers (electrons) are injected into the lasing states from an adjacent injector well through a tunnel barrier by phonon-assisted tunneling. As a

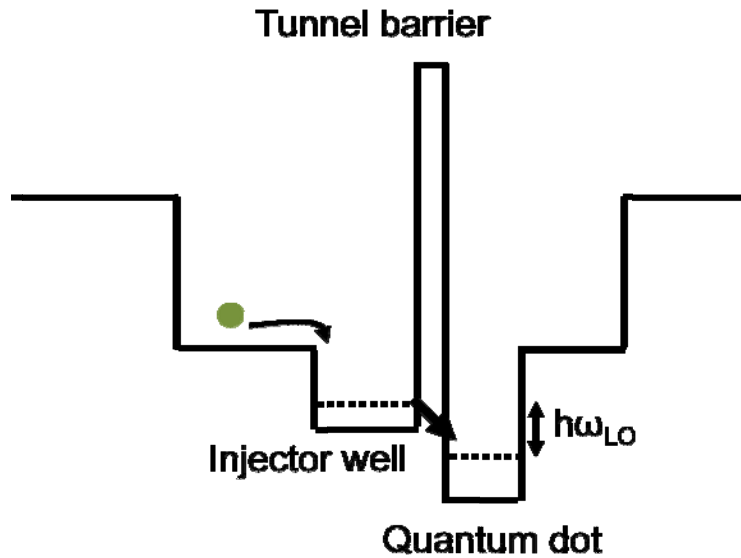


Figure 1.4: Schematic tunnel injection scheme. Cold electrons are tunneled into the ground state of the QDs by phonon assisted tunneling.

result, both the carrier heating in the active region and carrier leakage into the optical confinement layer are minimized. The only requirement is that the tunneling rate should be less than/or comparable to the lasing emission rate. Differential transient spectroscopy measurements confirm the tunnel injection time to be <2 ps in the TI-QD/QW laser heterostructures with temperature insensitivity. Enhanced modulation bandwidth and reduced Auger recombination and chirp were demonstrated in TI-quantum well lasers [34, 35]. Efficient tunneling of electrons from the injector well into the dots has been confirmed by femtosecond differential transmission spectroscopy measurements, which show an extremely fast tunneling time, ~ 1.7 ps [36]. Experiments showed QD TI lasers exhibit small-signal-modulation up to 30GHz, chirp < 0.1 Å, and nearly-zero α -factor,

etc. The energy separation of the hole states in QDs is less than the phonon energy, which induces thermal broadening of the hole distribution and temperature-sensitive operation. p-doping of the quantum dots can provide excess holes to fill the ground state at high temperatures, as illustrated in Fig. 1.5. The energy separation of the hole states in the QDs is less than the phonon energy, which induces thermal

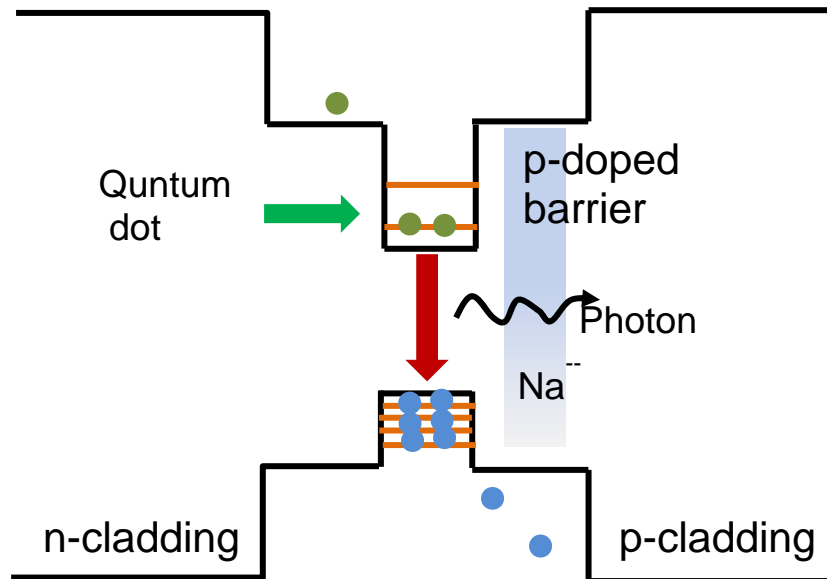


Figure 1.5: Schematic illustration of modulation p-doping of the quantum dot.

broadening of the hole distribution and temperature-sensitive operation. The excess holes provided by *p*-doping ensures that the hole ground states are filled and less injected electrons are needed for population inversion [34, 37]. Thereby, both the gain and the differential gain will increase, and the gain saturation associated with the thermal broadening of injected hole is reduced. Introduction of *p*-doping also form a natural barrier to help reduce the number of electrons which escape and leak into the GaAs barrier layer, which further reduces undesirable carrier recombination loss outside of the QDs.

P-doping in QDs is achieved by modulation doping in the barrier region. Considering the relatively-low dot density and the discrete energy levels in QDs, the optimum p-doping levels are $\sim 5.0 \times 10^{11} \text{ cm}^{-2}$, due to the low dot fill factor and the discrete energy levels in QDs. Optimization of the p-doping is extremely necessary because the excess holes provided by p-doping can occupy the wetting layer states, which can severely limit the potential benefits of this technique [38]. Additionally, p-doping can significantly enhance Auger recombination in QDs, which increases the threshold current [21].

1.4 Objective of the Thesis

Infrared lasers emitting at 1.3 μm and 1.55 μm are the most important light sources for fiber optic communication. Commercial lasers at these wavelengths are generally quantum well based lasers which suffer from higher threshold current, limited small-signal modulation bandwidth and most problematically poor temperature stability. Since quantum dots have higher gain and differential gain and also have atomic like discrete energy states, lasers incorporating quantum dots in the active region can be used to address these drawbacks of the state of the art commercial quantum well lasers used in fiber optic communication. On the other hand, micro-sized infrared lasers will emerge as basic building block for future on-chip optical communication. With the incorporation of quantum-sized emitters such as quantum dots, micro-sized lasers are also suitable for the study of quantum electrodynamics. Additionally, these lasers and laser arrays can be used for chip level chemical and biochemical sensors.

A novel microcavity formed by an epitaxial self-rolling mechanism has recently

drawn much attention as a potential cavity as a micro or nanoscale laser. The microcavity is formed by releasing a pseudomorphically strained epilayer from the host substrate. Figures 1.6(a) and (b) show schematically the rolling mechanism of an InGaAs/GaAs microtube and a optical microscopy image of a rolled-up microtube is shown in

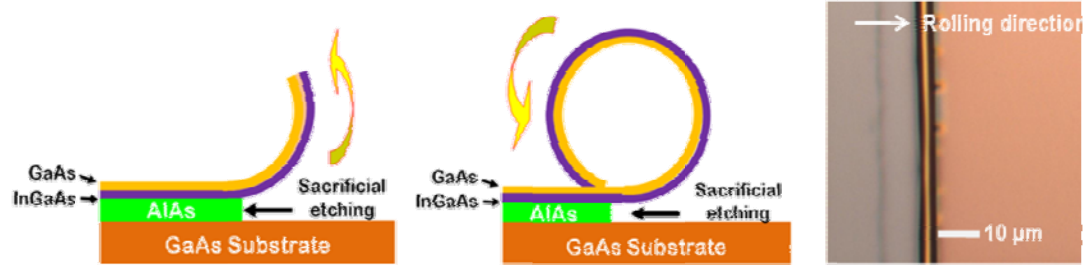


Figure 1.6: (a) and (b) schematic of the formation of an InGaAs/GaAs microtube on a GaAs substrate; (c) Optical microscopy image of an InGaAs/GaAs microtube formed on GaAs.

Fig. 1.6(c). The formation of the microtube is initiated by selective removal of an AlAs layer from beneath the strained InGaAs/GaAs layer by sacrificial etching. Of both fundamental and practical interest is the incorporation of quantum dots in the GaAs microtube structures, wherein controllable coupling between the dots and the whispering-gallery modes can potentially be achieved. Compared to many conventional optical microresonators, such quantum dot microtubes exhibit a number of favorable characteristics such as controllable diameter, atomistically smooth cavity wall, an extremely small mode volume, photolithographically definable surface area and a near perfect overlap between the optical field and gain medium (dot layers) which make them a promising candidate for a new generation of nanophotonic devices. Optically pumped microtube lasers have been demonstrated by several groups [39-45] by inserting

quantum wells or dots since the first demonstration by Prinz *et al.* [46]. One interesting property of the rolled-up microtubes is that they can be transferred controllably on to any foreign substrate (Fig. 1.7 (a)). Therefore, microtubes can in principle be transferred on to silicon substrate and an electrically injected quantum dot microtube laser and a quantum dot microtube detector as schematically shown in Fig. 1.7(b) have the potential

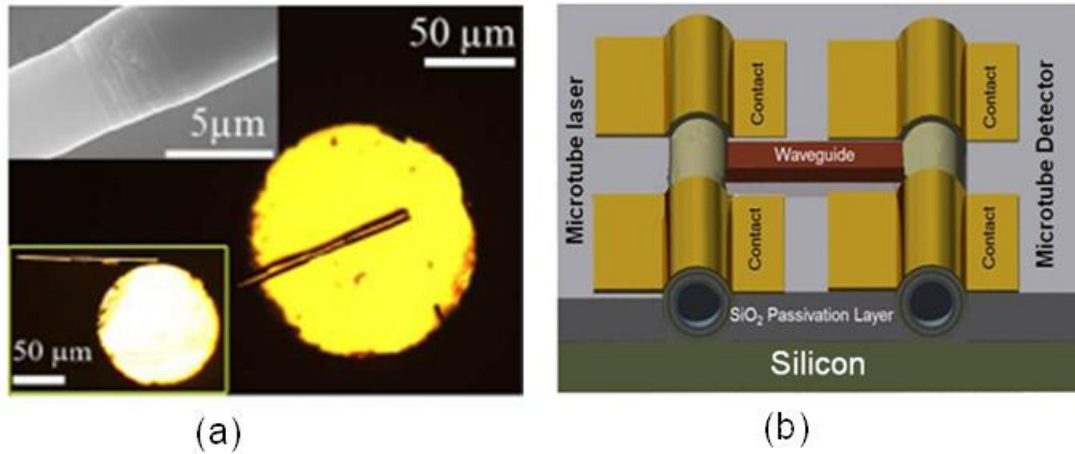


Figure 1.7: (a) Controlled transfer of an InGaAs/GaAs microtube on to the facet of a single mode fiber [44]; (b) schematic of a phototransceiver circuit consisting of an electrically injected microtube laser, a microtube detector and a waveguide connecting them.

to be used in future on-chip communication. Moreover, the unique hollow geometry of the microtube also makes them interesting for sensing applications. The objectives of the current work on microtube devices are to investigate quantum dot rolled-up microtube and their threshold behavior both analytically and experimentally, investigate a microtube phototransceiver and work towards an electrically injected microtube laser and also to investigate sensing applications.

Due to the fact that the minimum fiber attenuation occurs at 1.55 μm, this

wavelength is considered as the single most important wavelength for fiber optic communication. Lasers used at this wavelength are generally InP-based and the active (gain) region is lattice-matched $\text{In}_{0.53}\text{Ga}_{0.47}\text{As}/\text{InGaAsP}/\text{InP}$ or $\text{In}_{0.53}\text{Ga}_{0.47}\text{As}/\text{InGaAlAs}/\text{In}_{0.52}\text{Al}_{0.48}\text{As}$ double hetero-structure or multi-quantum wells (MQWs) [47-50]. Pseudomorphic or strain-compensated QWs are also used to engineer the gain, confinement energies and associated characteristics [51-53]. But these lasers suffer from severe temperature instability and the characteristic temperature of these lasers is typically less than 50 K. Therefore, quantum dot lasers which are well known for extremely high temperature stability can be used to address this drawback. Unfortunately, InAs quantum dots grown on InP substrate generally become elongated along $[\bar{1}10]$ direction, form quantum dashes and as a result lose the favorable characteristics of quantum dots. Very recently, C. Gilfert *et al.* have demonstrated the growth of InAs quantum dots and quantum dot lasers [54] at 1.55 μm which greatly renewed the interest in this field. However, their maximum characteristic temperature T_0 is 87 K ((Fig. 1.8 (a))) which is a good improvement over that of quantum well lasers but still significantly lower than T_0 of quantum dot lasers at 1.3 μm [21]. The maximum -3 dB modulation bandwidth as shown in Fig. 1.8(b) is 8.3 GHz which is significantly lower than state of the art quantum well lasers at 1.55 μm . Therefore, in order for the quantum dot laser to have any impact in the market in future, significant improvement is necessary in terms of modulation bandwidth as well as characteristic temperature. The objective of the work is to grow and optimize quantum dots on InP substrate and to

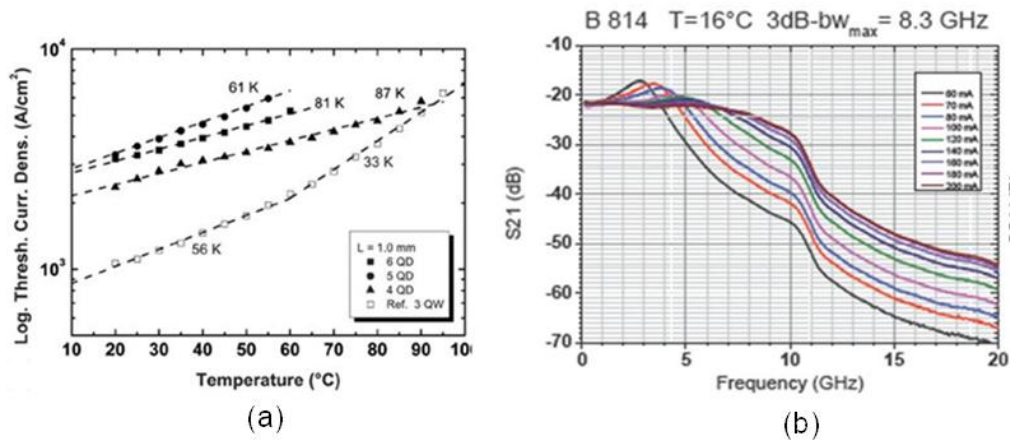


Figure 1.8: (a) Threshold current density vs. temperature characteristics of quantum dot lasers [55]; (b) small signal modulation characteristics [56].

improve the quantum dot laser static and dynamic characteristics by incorporating tunnel injection scheme and modulation p-doping of the active region.

1.5 Dissertation Overview

The goal of this dissertation is to investigate and optimize the growth of InAs quantum dot nanostructures both on InP and GaAs substrates using molecular beam epitaxy (MBE) and investigate the characteristics of both unconventional (rolled-up microtube) and conventional (Fabry-Pérot) edge emitting lasers incorporating those nanostructures in the active region. Additionally, the potential application of quantum dot rolled-up microtube as a fluid sensor device has also been explored.

A detailed growth study of the InAs quantum dots on GaAs substrate is discussed in chapter 2. A thorough investigation of the growth of InAs/In_{0.53}Ga_{0.23}Al_{0.24}As quantum dots on InP for the 1.55 μm wavelength emission grown by limiting the anisotropic migration of In ad-atoms on In_{0.53}Ga_{0.23}Al_{0.24}As surface and the dependence

of their properties on different growth parameters is also discussed in chapter 2. A novel nanostructure, quantum rings, is obtained by in-situ annealing of self-organized quantum dots. An intersubband photodetector with quantum rings in the active region having spectral response in the 1-3 THz range is also realized and presented.

The rolled-up microtube laser has been discussed in chapter 3. The laser microcavity is formed by an epitaxial strain driven mechanism and contains self-organized InAs quantum dots in the active region inserted inside the microtube wall. Rolled up microtubes have atomically smooth surfaces providing a high quality (Q) factor. They also have a near perfect overlap between the maximum optical field intensity and the QD layers, which ensures low lasing threshold. Different loss mechanisms in the microtube microcavity have been investigated. A theoretical study of modal gain in a microtube cavity shows that modal gain is inversely proportional to the radius of the microtube.

In chapter 4, a quantum dot rolled-up microtube directional coupler is described. The rolled-up microtube active directional coupler is fabricated by bringing two microtubes in close proximity. The unique hollow waveguide morphology increases the interaction of the electromagnetic mode with the surrounding medium and this property can be utilized for fluid or gas sensing applications.

A novel rolled-up microtube optoelectronic integrated circuit is presented in chapter 5. The device is made of a quantum dot rolled-up microtube optically pumped laser and a microtube detector connected by an a-Si/SiO₂ waveguide. The overall responsivity of the integrated circuit is measured to be 34 mA/W.

InAs/In_{0.53}Ga_{0.23}Al_{0.24}As/InP quantum dot lasers incorporating a tunnel injection

heterostructure and modulation doped active region grown on InP substrate for the 1.55 μm wavelength range are discussed in chapter 6. The lasers exhibit very high temperature stability with characteristics temperature $T_0 = 227 \text{ K}$ and 100 K for the temperature range of $5\text{-}45 \text{ }^\circ\text{C}$ and $45\text{-}75 \text{ }^\circ\text{C}$ respectively. The maximum 3-dB modulation bandwidth of the lasers is $f_{3dB} (max) = 14.4 \text{ GHz}$ which is good for 22 Gb/s digital data transmission.

Finally, a brief summary of the work and suggestion for the future work is outlined in chapter 7.

Chapter II

MBE Growth of Self-organized Quantum Dots

2.1 Stranski-Krastanov Growth of Self-Organized Quantum Dots

Extensive research on the fabrication and growth of quantum dots has been carried out since the prediction of the superior performance of quantum dot (QD) devices for optoelectronic applications. These methods include e-beam lithography, focused-ion-beam (FIB) etching, and self-organized epitaxial growth [57-59]. However, to date most successful method to realize quantum dot structure is through the self-organization of quantum dots by epitaxial growth technique. During the highly strained heteroepitaxy the formation of the three-dimensional structure provides a way of strain relief and prevents the formation of dislocations. Uniform dots with small size, high density and high emission efficiency can be easily realized in conventional molecular beam epitaxy (MBE) and metalorganic vapor phase epitaxy (MOVPE). As a result, epitaxial growth technique has become the dominant technique for making quantum dots.

Depending on the lattice mismatch between the epitaxial layer and the substrate, epitaxial growth usually occurs in three modes: (i) Frank-van der Merwe (FM) [60], (ii) Stranski-Krastanov (SK) [61], or (iii) Volmer-Weber (VW) [62]. The growth of epitaxial thin films on a single crystal surfaces depends critically on the interaction strength between adatoms and the surface. In Volmer-Weber (VW) growth, adatom-adatom

interactions are stronger than those of the adatom with the surface, leading to the formation of three-dimensional adatom clusters or islands. Growth of these clusters, along with coarsening, will cause rough multi-layer films to grow on the substrate surface. This growth usually occurs when there is a large lattice mismatch between the substrate and the epilayer. On the other hand, during the Frank-van der Merwe (FM) growth, which occurs for lattice matched substrate and epilayers, adatoms attach preferentially to surface sites resulting in atomically smooth, fully formed layers. This layer-by-layer growth is two-dimensional, indicating that complete films form prior to growth of subsequent layers [63, 64]. Stranski–Krastanov growth is an intermediary process characterized by both 2D layer and 3D island growth. Transition from the layer-by-layer to island-based growth occurs at a critical layer thickness which is highly

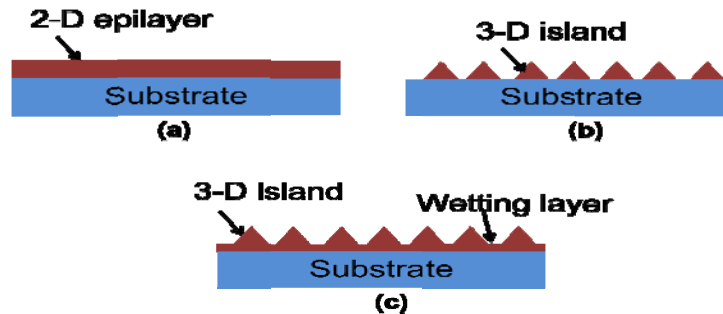


Figure 2.1: Schematics representation of (a) Frank–van der Merwe (FM) growth mode; (b) Volmer-Weber (V-W) growth mode; (c) Stranski-Krastanov (S-K) growth mode.

dependent on the chemical and physical properties, such as surface energies and lattice parameters, of the substrate and the film[63-64]. Figure 2.1 is a schematic representation of the three main growth modes for different surface coverages. The mechanism by

which a thin film grows is dictated by the chemical potentials of the first few deposited layers [63, 65]. As proposed by Markov, the model for the layer chemical potential per atom is given by $\mu_n = \mu_\infty + [\varphi_a - \varphi'_a(n) + \varepsilon_d(n) + \varepsilon_e(n)]$ where μ_∞ is the bulk chemical potential of the adsorbate material, φ_a is the desorption energy of an adsorbate atom from a wetting layer of the same material, $\varphi'_a(n)$ is the desorption energy of an adsorbate atom from the substrate, $\varepsilon_d(n)$ is the per atom misfit dislocation energy, and $\varepsilon_e(n)$ is the per atom homogeneous strain energy. In general, the values of these parameters depend in a complex way on the thickness of the growing layers and lattice misfit between the substrate and adsorbate film. In the limit of low strain, $\varepsilon_d(n) \ll \mu_\infty$, the criterion for a film growth mode is dependent on $\frac{d\mu}{dn}$

VW growth: $\frac{d\mu}{dn} < 0$ (adatom cohesive force is stronger than surface adhesive force)

FM growth: $\frac{d\mu}{dn} > 0$ (surface adhesive force is stronger than adatom cohesive force)

SK growth can be described by both of these inequalities. Initially the film growth follows FM mechanism, but after growing a certain thickness, which is called the critical thickness, this strain induces a sign reversal in the chemical potential leading to a switch in the growth mode. At this point it is energetically favorable to nucleate islands and further growth occurs by a VW type mechanism [65]. Self-organized quantum dots discussed in this chapter are grown in the SK growth mode by depositing InAs on either GaAs or $\text{In}_{0.53}\text{Ga}_{0.23}\text{Al}_{0.24}\text{As}$ lattice matched to InP substrate.

2.2 Optimization of InAs Quantum dots on GaAs Substrate

Self-organized quantum dots are grown on (001) GaAs substrate. At first a 200 nm GaAs buffer layer is grown at 600 °C. After that growth temperature is lowered to 495-530 °C to grow the InAs quantum dots. The test structure, which contains three layers of self organized InAs quantum dots separated by 30 nm spacer layer, is shown in Figure 2.2. The top quantum dot layer is left uncapped to facilitate

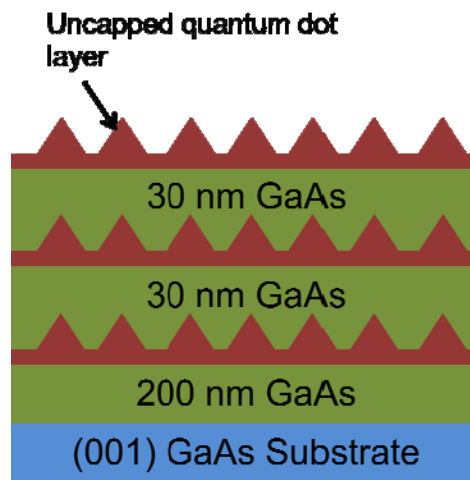


Figure 2.2: Test structure for quantum dot calibration. Top quantum dot layer is left uncapped in order to facilitate atomic force microscopy (AFM) imaging.

atomic force microscopy (AFM). The qualities of the dots such as photoluminescence intensity, linewidth, dot density etc. are critically dependent on the growth conditions, which require a lot of calibration of the growth temperature, growth rate, V/III ratio, growth interruption etc. to get the optimum dot quality.

2.2.1 Effect of Temperature

We have investigated the role of temperature by varying the growth temperature

of the quantum dots from 500-530 °C keeping the other parameters constant. The AFM images of the quantum dots shown in Figure 2.3(a), (b) and (c) are grown at 495 °C,

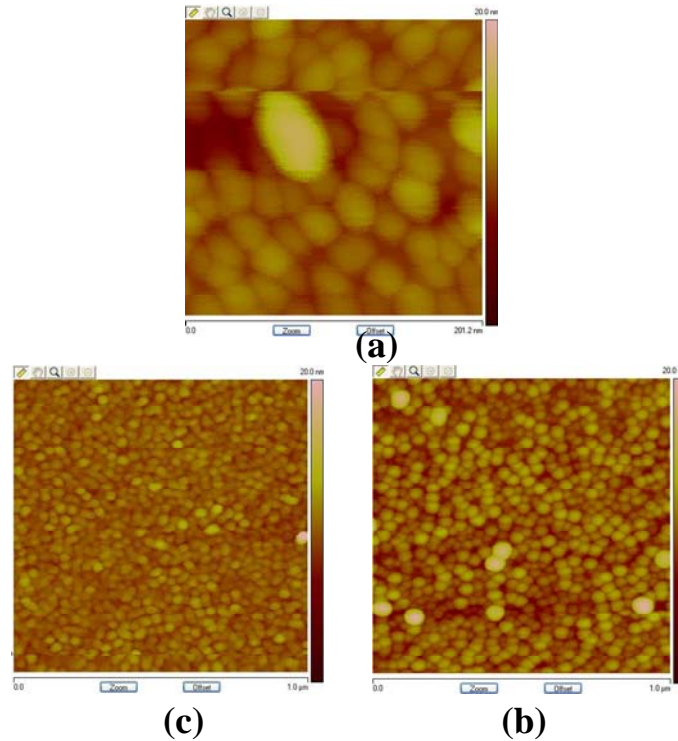


Figure 2.3: Atomic force microscopy (AFM) images of the 2.5 monolayer InAs/GaAs quantum dot layers grown at (a) 495°C; (b) 510°C; (c) 530 °C with a group V/III ratio of 40.

510 °C and 530 °C respectively by depositing 2.5 monolayer (ML) of InAs material at a growth rate of 0.12 ML/sec and with a V/III ratio of 40. From the AFM images, it is observed that the areal dot density at lower growth temperature is lower as the number of coalesced dots increases and dot density decreases at very high temperature due to the desorption of quantum dots at high temperature. The room temperature photoluminescence (PL) spectra of the three quantum dot layers are shown in Fig. 2.4. The 510 °C dots have the best PL intensity and linewidth followed by 530 °C dots and 495 °C dots. We believe that the reduced intensity of PL spectrum for higher temperature dot

is a direct consequence of the reduced dot density at higher temperature. On the other hand, for lower temperature (495 °C), the reduction in In adatom mobility on the GaAs surface produces coalesced dots, creates misfit dislocations and affects uniformity in the dot layer which in turn affects the PL characteristics of the quantum dots.

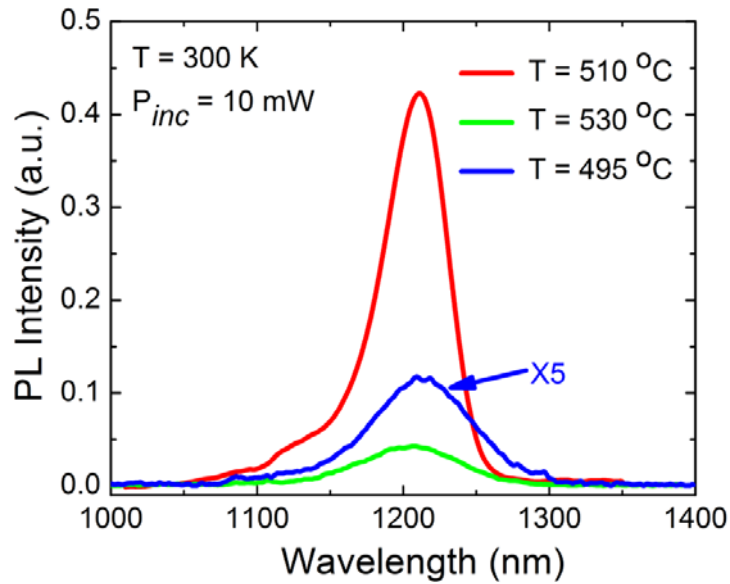


Figure 2.4: Photoluminescence spectra of the InAs/GaAs quantum dots grown at different temperatures with a group V/III ratio of 40.

2.2.2 Effect of V/III Ratio

The V/III ratio plays a very important role in the quality of self-organized quantum dots by changing the surface diffusion length of the group III atoms. We have investigated the impact of different V/III ratio on the quality of the quantum dots by varying the that ratio from 35 - 45 keeping the growth temperature at 510 °C and the growth rate at 0.12 ML/sec. The AFM images of the quantum dot layers are shown in Figure 2.5. The PL spectra of the different dot layers are shown in Fig. 2.6. At higher V/III ratio of 40, the dots become coalesced and the density of the quantum dots decrease. Lower group V/III ratio enhances the migration of the In adatom on the GaAs

surface and as a result dots become and the average dot density is $1 \times 10^{11} \text{ cm}^{-2}$.

For very low V/III ratio, the group V pressure becomes insufficient to prevent

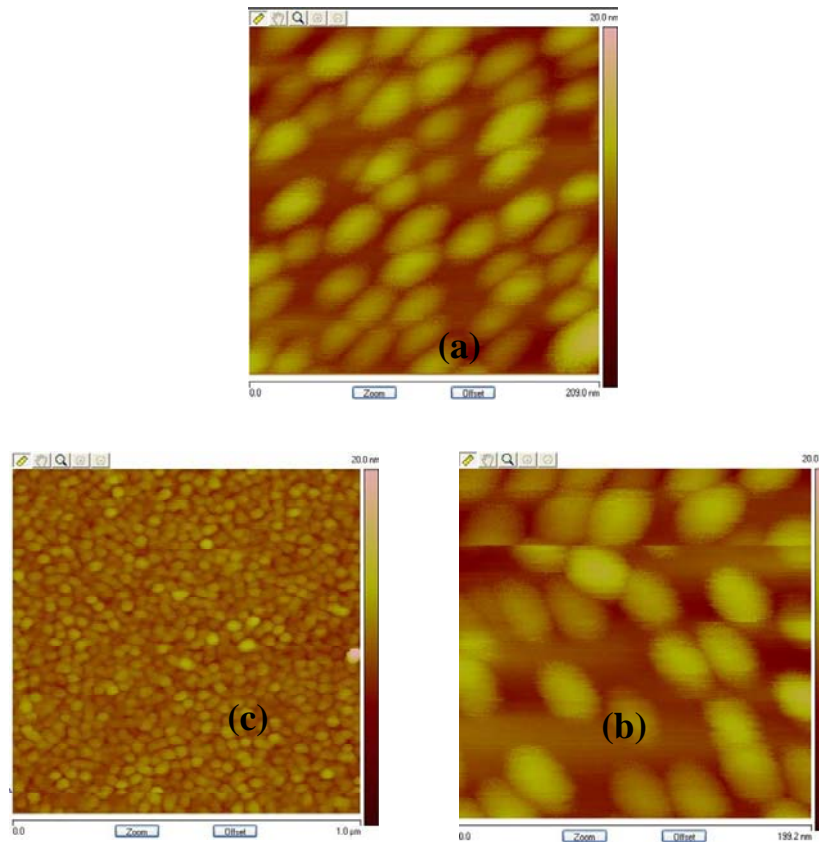


Figure 2.5: Atomic force microscopy images of the 2.5 monolayer InAs/GaAs quantum dot layers grown at 510 °C; with a group V/III ratio of (a) 35; (b) 40; (c) 45.

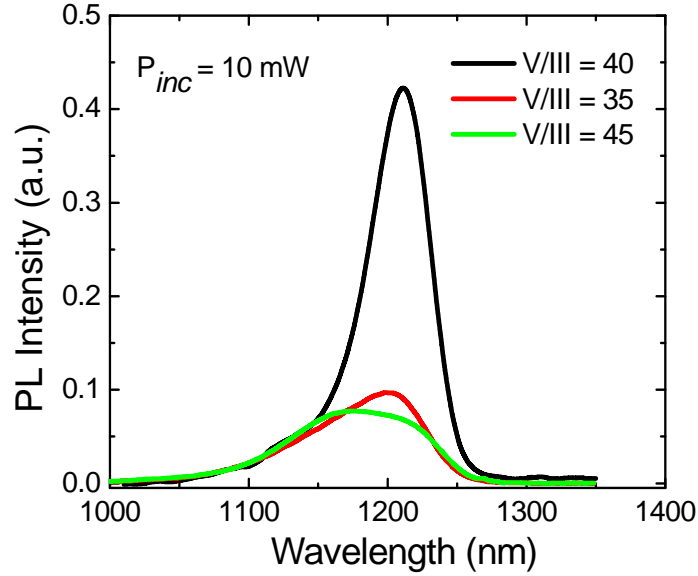


Figure 2.6: Photoluminescence spectra of the 2.5 monolayer InAs/GaAs quantum dot layers grown at 510 °C with different group V/III ratios.

Table 2.1: Properties of InAs/GaAs quantum dot grown under different V/III ratio.

Temperature	Dot density (cm^{-2})	Peak normalized PL intensity	Linewidth (FWHM) (meV)
35	7×10^{10}	0.25	30
40	1×10^{11}	1	25
45	$5\text{-}6 \times 10^{10}$	0.22	37

desorption of In adatom from the surface and as a result the linewidth and the intensity of the PL emission degrades. The properties of InAs/GaAs quantum dots grown at different conditions are summarized in Table 2.1.

2.3 Growth and Optimization of InAs/ $\text{In}_{0.53}\text{Al}_{0.24}\text{Ga}_{0.23}\text{As}$ /InP Quantum dots

Unfortunately InAs quantum dots grown on GaAs substrate cannot emit light in the 1.55 μm range which is the most desired wavelength for fiber optic communication. This problem can be overcome by moving to the InP material system where InAs

quantum dots grown on $\text{In}_{0.53}\text{Al}_{0.24}\text{Ga}_{0.23}\text{As}$ lattice matched to InP emit in the 1.55 μm range. Growth of InAs/ $\text{In}_{0.53}\text{Al}_{0.24}\text{Ga}_{0.23}\text{As}$ quantum dots is not straight forward since under non optimum growth condition the dots elongate in the $[\bar{1}10]$ direction and form quantum dashes rather than quantum dots [66, 67]. The test heterostructure (shown in Fig. 2.7) used for the growth optimization of quantum dots is grown on (001) InP substrate and contains a 200 nm $\text{In}_{0.52}\text{Al}_{0.48}\text{As}$, a 50 nm $\text{In}_{0.53}\text{Ga}_{0.23}\text{Al}_{0.24}\text{As}$ and three layers of self-organized quantum dots separated by 30 nm $\text{In}_{0.53}\text{Ga}_{0.23}\text{Al}_{0.24}\text{As}$ spacer layer. A 200 nm $\text{In}_{0.52}\text{Al}_{0.48}\text{As}$ layer is first grown at 515°C. After that the substrate temperature is lowered to 485-505 °C to grow the subsequent layers. Figure 2.8 shows the high resolution X-ray diffraction image of $\text{In}_{0.53}\text{Ga}_{0.23}\text{Al}_{0.24}\text{As}$ layers grown

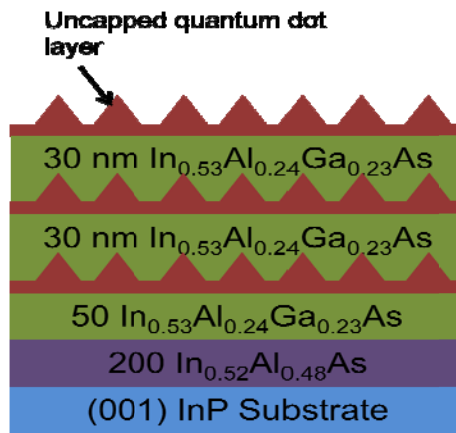


Figure 2.7: Test structure for InAs/ $\text{In}_{0.53}\text{Ga}_{0.23}\text{Al}_{0.24}\text{As}$ quantum dot calibration. Top quantum dot layer is left uncapped in order to facilitate atomic force microscopy (AFM) imaging.

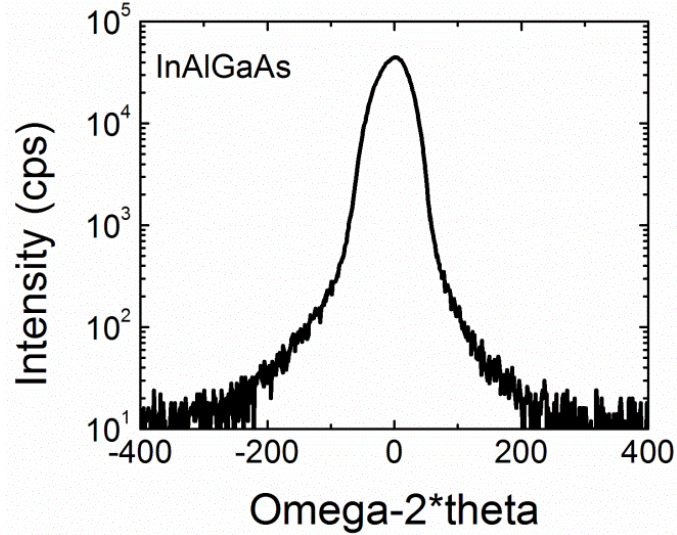


Figure 2.8: X-ray diffraction image of InAlGaAs layer grown on (001) InP substrate.

on InP substrate. The narrow linewidths of the images indicate good crystal quality. The top quantum dot layer was left uncapped to facilitate AFM on the quantum dots.

2.3.1 Effect of Temperature

Figure 2.9(a), (b), and (c) shows the AFM images of the quantum dots grown at three different temperatures of 480 °C, 495 °C and 510 °C by depositing 5 ML of InAs with a V/III ratio of 18 under As₂ flux, which limits the elongation of quantum dots. At higher temperature the dots are more dash like than the dots grown at lower temperature. Due to increased In adatom diffusion length at higher temperature, quantum dots elongate in the $[\bar{1}10]$ direction and almost all the features are dash like. The height of the dots/dashes are about 2-3 nm and density is very low. The photoluminescence

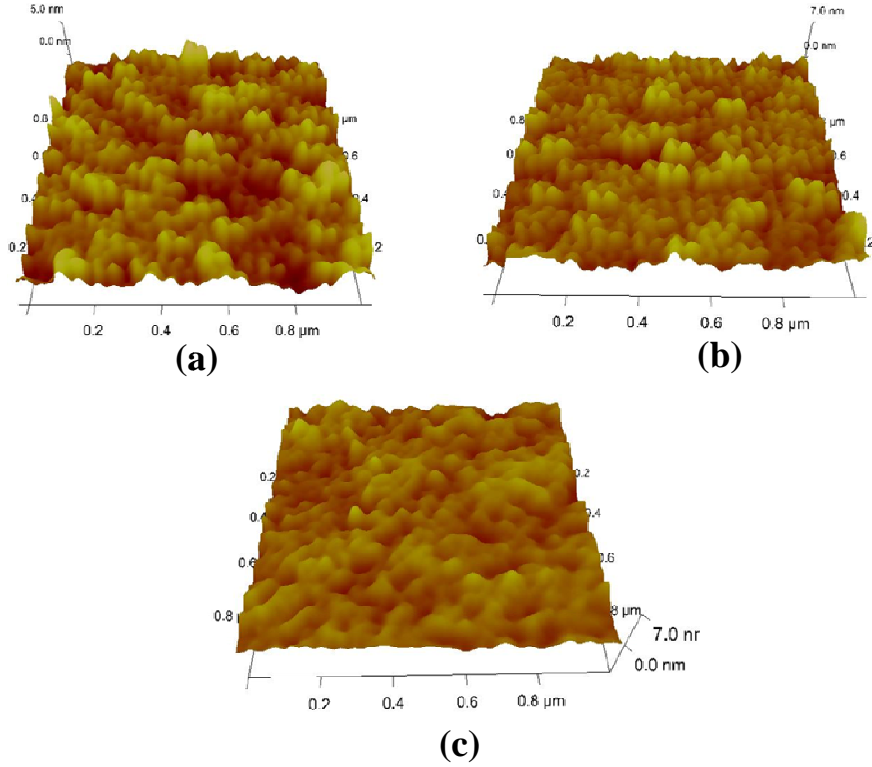


Figure 2.9: Atomic force microscopy images of the 5 monolayer InAs/In_{0.53}Ga_{0.23}Al_{0.24}As quantum dot layers grown at (a) 480 °C; (b) 495 °C; (c) 510 °C with a group V/III ratio of 18.

spectrum of the dots/dashes is shown in Figure 2.10. The linewidth of the PL spectrum is ~ 54 meV and the intensity is comparatively low. As the growth temperature is decreased, In adatom diffusion length decreases and the dot nature is enhanced. At 495 °C, dots are more uniform and dot density is $\sim 2\text{-}3 \times 10^{10} \text{ cm}^{-2}$. The linewidth of the PL spectrum is ~ 45 meV and the intensity increases substantially. But at very low temperature, the dots become non-uniform again due to reduced In adatom migration and forms big clusters.

2.3.2 Role of V/III Ratio

V/III ratio, along with temperature, plays a very important role on the growth of

quantum dot/dash. Figures 2.11(a), (b), and (c) show the AFM images of the quantum dot/dash layers grown at 495 °C with a V/III ratio of 13, 18 and 23 respectively.

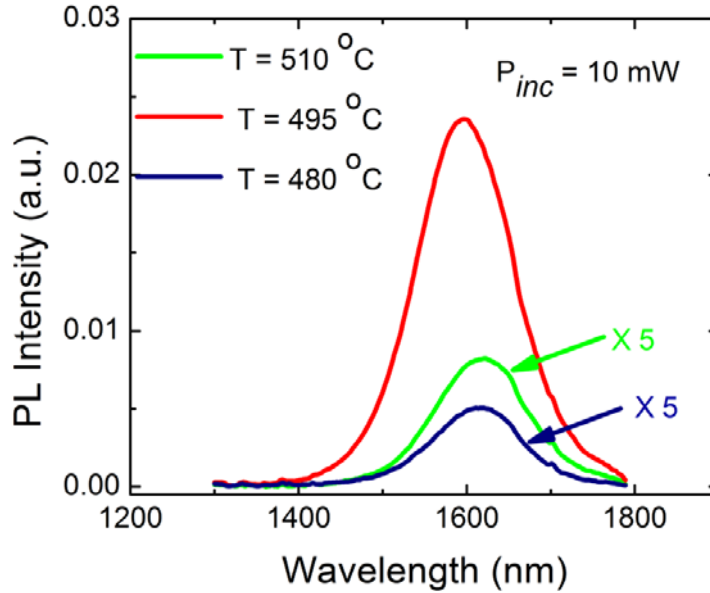


Figure 2.10: Photoluminescence spectra of the InAs/In_{0.53}Ga_{0.23}Al_{0.24}As quantum dots grown at different temperatures with a group V/III ratio of 18.

The dash nature of the dot/dash layer becomes dominant at a low V/III ratio. This is because of the deficiency of the As₂ species on the growth surface, which makes anisotropic migration easier for the In adatom and there dots become elongated and form dashes. With the increases of V/III ratio, the presence of As₂ species on the growth surface become sufficient to prevent that anisotropic migration and dot nature in the dot/dash layer increases. However too much As₂ on the surface reduces the mobility of the In adatom significantly which affects the uniformity in the dot layer. Figure 2.12 shows the PL spectra of the quantum dot layers grown at three different V/III ratios. From the PL spectra it is seen that with a V/III ratio of ~18 and a growth temperature of

495°C, best quality dots are obtained. Dot quality worsens considerably both with lower and higher V/III ratio. Although we were able to get dot

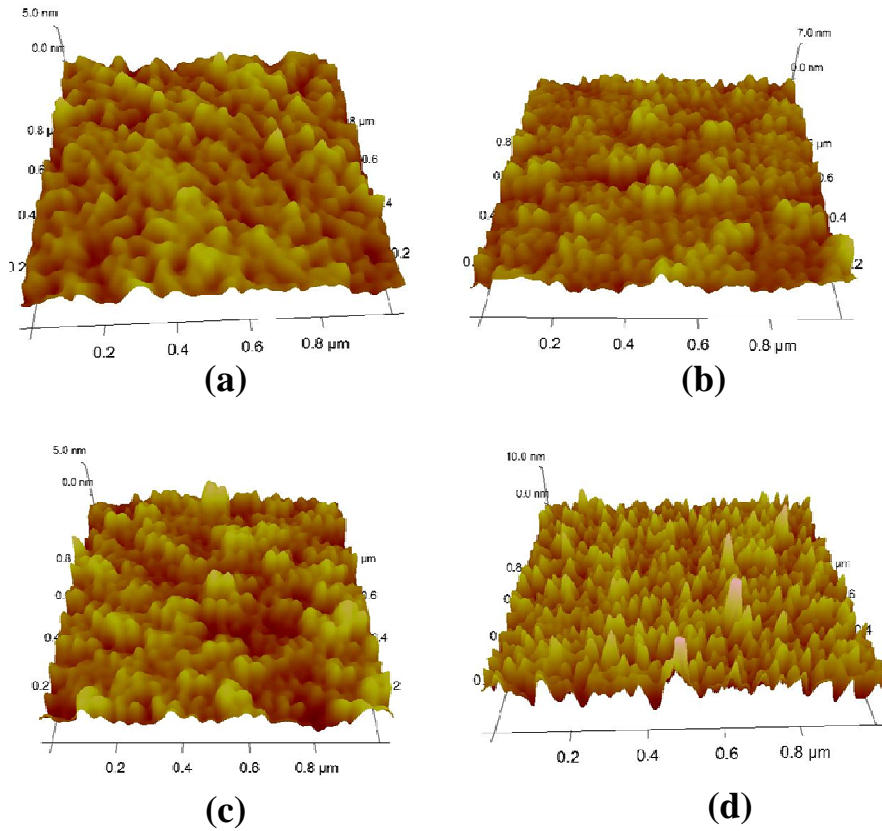


Figure 2.11: Atomic force microscopy images of the 5 monolayer InAs/ $\text{In}_{0.53}\text{Ga}_{0.23}\text{Al}_{0.24}\text{As}$ quantum dot layers grown at 495 °C with group V/III ratio of (a) 13; (b) 18; (c) 23; (d) quantum dots grown with same growth condition but with a 5 Å GaAs grown just before the growth of InAs quantum dots.

like nanostructures by varying the temperature and the V/III ratio, the dots are worse in terms of PL linewidth and areal dot density compared to the InAs/GaAs quantum dots. To further improve the dot characteristics, we grew a very thin 5 Å GaAs layer just before growing the quantum dots. The AFM image of the quantum dots grown by this technique is shown in Fig. 2.11(d). As evident from the image, the dot density

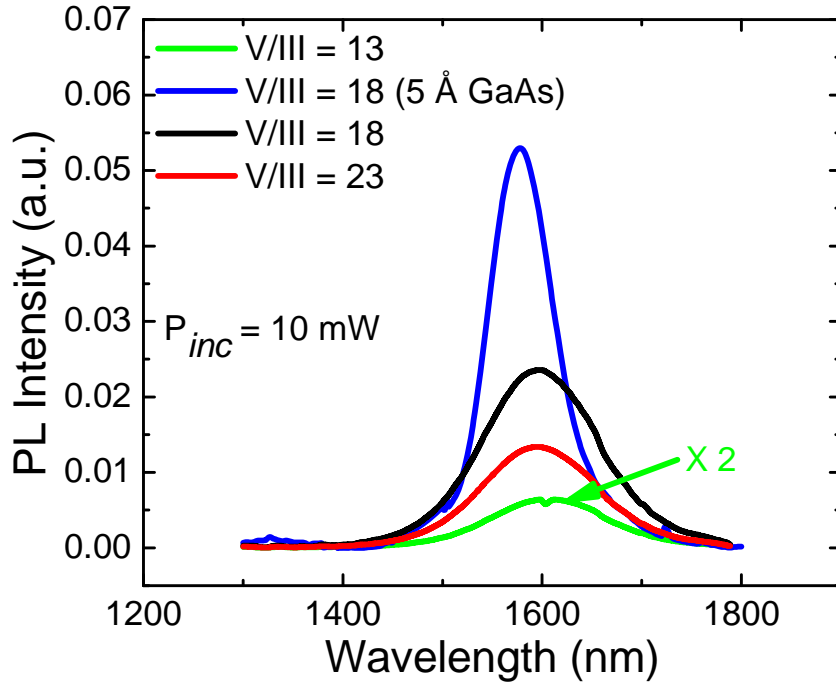


Figure 2.12: Photoluminescence spectra of the InAs/In_{0.53}Ga_{0.23}Al_{0.24}As quantum dots grown at temperature 495°C with different group V/III ratio.

increased significantly to $\sim 5 \times 10^{10} \text{ cm}^{-2}$ and the average dot height increased to 5-6 nm. The PL intensity also increased and the linewidth got reduced to $\sim 32 \text{ meV}$ at room temperature which is a significant improvement. We believe that the presence of the ultrathin GaAs layer on the surface makes the surface smooth and therefore helps the growth of uniform dots. It also alters the strain on the surface to some extent. As a result, a blue shift in the PL spectrum is also observed. The properties of InAs/In_{0.53}Al_{0.24}Ga_{0.23}As/InP quantum dots grown at different conditions are summarized in Table 2.2.

Table 2.2: Properties of InAs/In_{0.53}Al_{0.24}Ga_{0.23}As/InP quantum dot grown at 495 °C with different V/III ratio.

V/III Ratio	Dot density (cm ⁻²)	Peak normalized PL intensity	Linewidth (FWHM) (meV)
13	10 ¹⁰	0.04	~ 55
18	2-3×10 ¹⁰	0.5	~ 45
23	2×10 ¹⁰	0.25	~ 50
18 (5 Å GaAs)	5×10 ¹⁰	1	~32

2.4 Growth of InAs/GaAs Quantum Ring

A quantum ring is a novel nanostructure that is formed by insitu annealing of self-organized quantum dots [68-70]. The formation mechanism of the quantum ring structure is schematically shown in Figure 2.13. First, InAs quantum dots are grown in the S-K mode. Next, a GaAs/AlAs cap layer is deposited to partially cover the dot. Finally, the substrate undergoes an annealing process, during which the center part of the quantum dots evaporates and diffuses outwards and form quantum rings.

Quantum ring ensembles developed here at the University of Michigan were grown by molecular beam epitaxy in an EPI Mod Gen II system equipped with an arsenic cracker. Insitu reflection high energy electron diffraction (RHEED) was used to monitor the formation of the quantum dots. Sample for AFM or photoluminescence study was grown on an (001)-oriented semi-insulating GaAs substrate. First, a 1000Å GaAs buffer layer was grown at 600°C. The substrate temperature was then lowered to 530°C and 2.6 monolayers of InAs was deposited at a rate of 0.05 monolayer/sec. Self-organized quantum dots were formed following growth of 1.8 monolayers of an InAs

wetting layer. A 10Å AlAs cap layer was grown on the InAs islands at 530°C. Growth was interrupted and the capped islands were annealed at 580°C for 30 sec, under

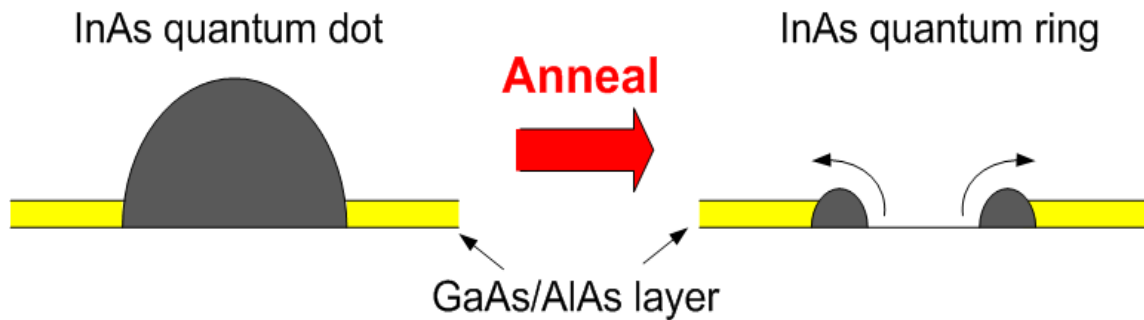


Figure 2.13: Schematic of the formation mechanism of self-organized quantum ring.

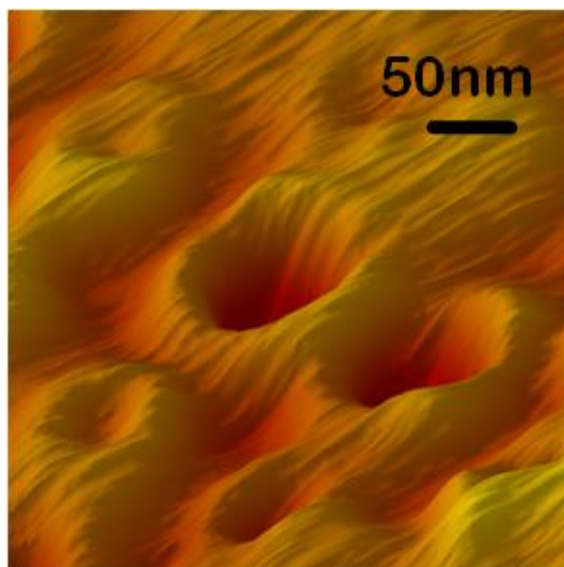


Figure 2.14: AFM image of quantum rings grown by insitu annealing of self-organized quantum dots.

an As₂ flux to form the quantum rings. The function of the AlAs layer was to reduce the surface mobility of group III atoms on the AlAs surface since AlAs has higher bonding strength than GaAs. In this way, the ring shape is better preserved during the annealing process.

An atomic force microscopy (AFM) image of exposed QR layers is shown in Figure 2.14. The height, inner diameter, and outer diameter of the rings are typically 2-4, 50, and 80nm respectively. The aerial density of the rings is estimated to be $\sim 10^{10} \text{ cm}^{-2}$.

Figure 2.15 shows a cross-sectional transmission electron microscopy (XTEM) image of a single quantum ring measured in another group using similar growth techniques [71]. The ring-like shape of the nanostructure is revealed in the XTEM image.

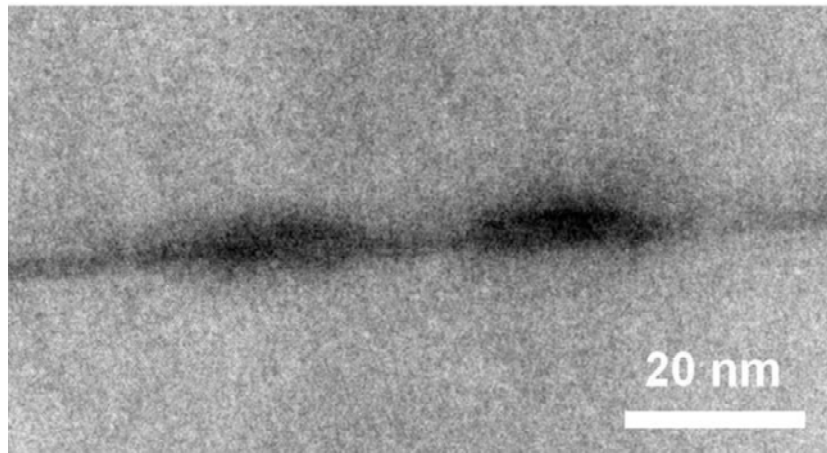


Figure 2.15: XTEM image of an In(Ga)As quantum ring grown by MBE [71]

2.4.1 Application of Quantum Rings in Intersubband Photodetectors

Intersubband photodetectors using zero dimensional quantum structures in the active region are predicted to have an edge over present THz detecting technologies, since three dimensional confinement leads to normal incident detection, low dark current and high responsivity. In particular, quantum dot detectors have demonstrated success in the 15-100 THz range.

To extend the detection range to the longer-wavelength region i.e 1-3 THz, a smaller intraband transition energy ΔE is needed. Utilizing the excited states transition has been one feasible approach to achieve smaller ΔE , as described. Another intuitive idea is to make the spatial confinement smaller since a reduction in size pushes the bound energy states towards the barrier energy level. The nanostructure of interest for this application is the quantum ring (QR), which can be formed after the epitaxy of self-organized InAs quantum dots on GaAs. A few nanometers of a GaAs or GaAs/AlAs cap layers are grown on the pyramid/lens-shaped QDs. The growth is then interrupted and an insitu anneal is performed. The quantum dot transforms into a quantum ring due to the lateral diffusion of indium. The height, inner diameter, and outer diameter of the rings are typically 2-4, 50, and 80nm, respectively. The reduced intraband transition energy of these quantum rings

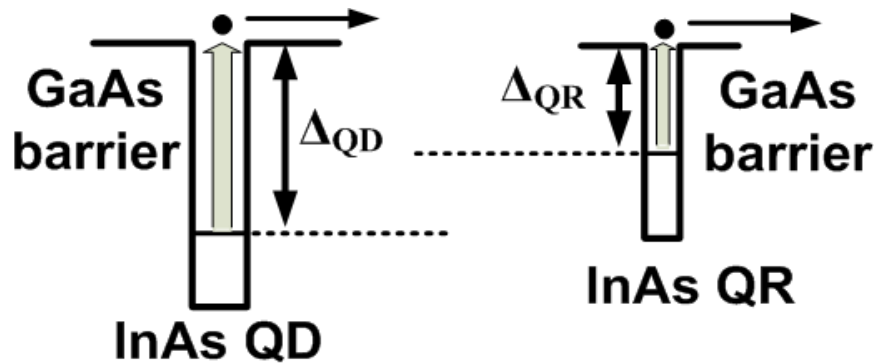


Figure 2.16: Schematic band diagram of QD and QR showing a reduced intraband transition energy for the latter

compared with that of the quantum dots is schematically shown in Figure 2.16. The photoluminescence spectra of the 2.5 ML quantum dots and quantum rings are shown in

Figure 2.17. From the blue shift of the photoluminescence spectrum of the quantum rings, it is evident that they have smaller bound state to continuum transition energy and therefore these nanostructures are suitable for terahertz detection via intersublevel absorption.

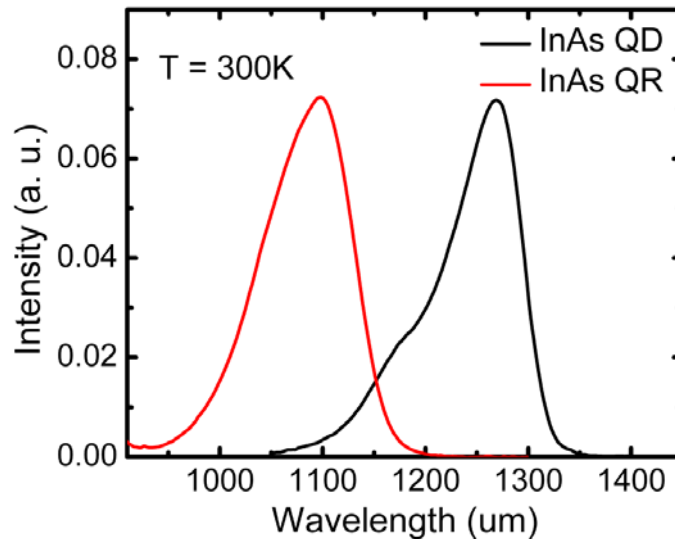


Figure 2.17: Photoluminescence spectra of quantum rings and their precursor quantum dots.

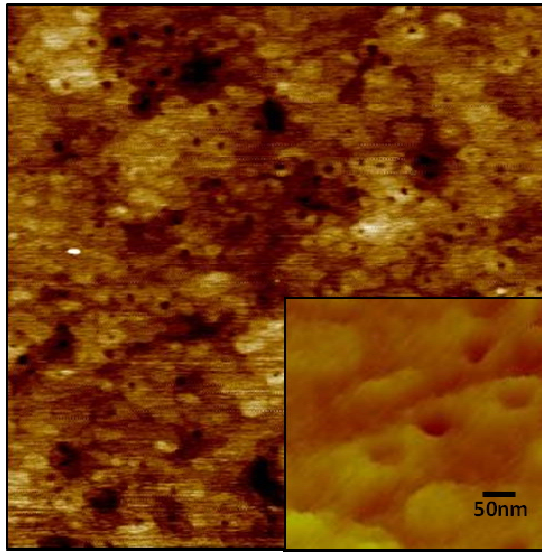
2.4.1.1 Quantum Ring Intersubband Photodetectors for the 1-3 THz Range

Terahertz (THz) detectors are needed for molecular spectroscopy, medical diagnostics, security and surveillance, quality control and astronomy applications [72-74]. Devices operating at high temperature are always desired for every application; however the development of room temperature THz detectors still remains a challenge. Nevertheless, high performance THz detectors operating at low temperatures are also in demand, particularly for astronomy and space applications [73]. Bolometers or extrinsic photodetectors, based on Ge, Si or InSb, operated at 4.2 K or lower temperatures are

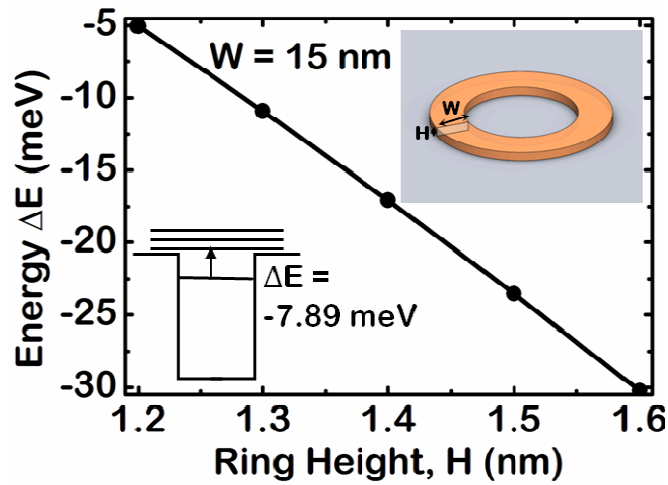
currently used, but they have their drawbacks. Hence, the development of semiconductor based THz detectors [75, 76], whose operation is based on electronic transitions and having figures of merit comparable to those of bolometers, will have an appeal even if they operate at low temperatures. It is also important for some applications to detect radiation spectra of frequency in the 1-3 THz range.

Semiconductor-based quantum dot (QD) and quantum ring intersubband (QR) detectors [77-82] have been used for the detection of long wavelength radiation. Quantum rings are derived from epitaxially grown self-organized quantum dots by post growth annealing [83, 84] and are generally smaller than the dots. Detection in the 1-3 THz range has been more elusive. In the present study, we have investigated the characteristics of small quantum rings grown by molecular beam epitaxy (MBE) and of intersublevel THz photoconductive detectors with quantum ring active regions. It is found that the quantum ring intersublevel detectors (QRIDs) exhibit very low dark current and strong response in the 1-3 THz range, with the peak response measured at 1.82 THz (165 μm) in the temperature range of 5-10 K. This detection peak is characterized by a peak responsivity of 25 A/W and specific detectivity of 1×10^{16} Jones. These characteristics compare very favorably with those of bolometers.

In order to get an estimate of the size of the QRs in which the intersublevel spacing would be in the 1-3 THz range, we have performed calculations using a simplified model. From atomic force microscopy (AFM) images such as one shown



(a)



(b)

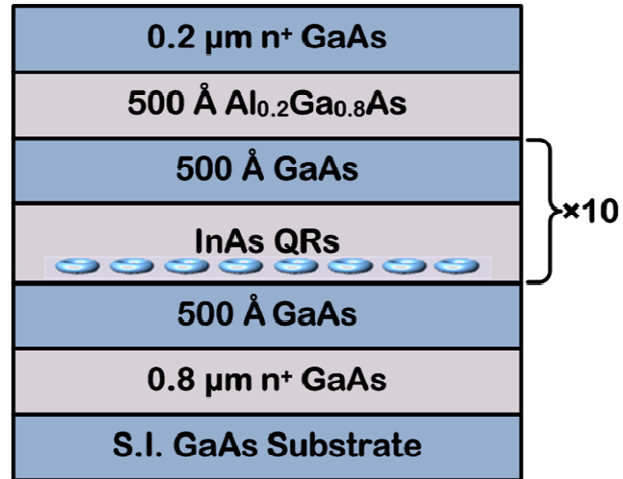
Figure 2.18: (a) AFM image of InAs quantum rings formed by post-epitaxy thermal annealing of quantum dots. Inset shows a magnified image and dimensions; (b) calculated ground state energy in the quantum ring as a function of ring height for ring width $W = 15$ nm. Inset shows the schematic of the quantum ring and calculated bound state in a quantum ring with $W = 15$ nm and $H = 1.25$ nm.

in Figure 2.18(a), it is evident that the rings have a height in the range of 1.2-1.5 nm and inner and outer radii of 25 and 40 nm, respectively. Carrier confinement in the rings

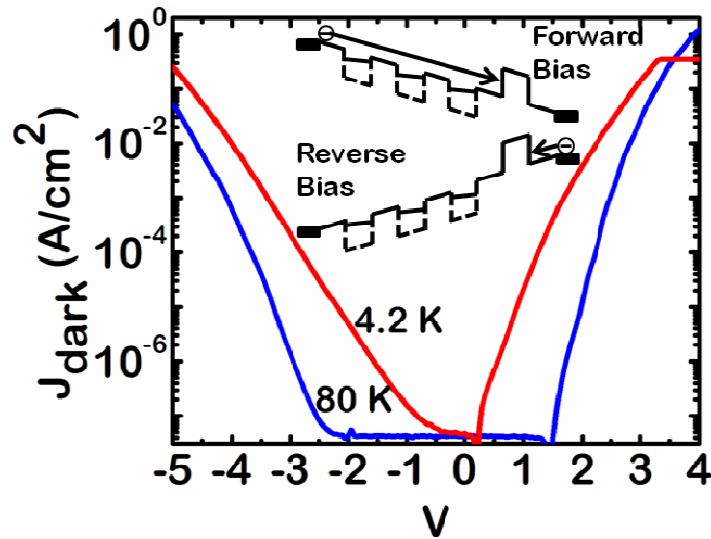
primarily results from their width and height. We have therefore, approximated the ring by a quantum wire of equal width and height and solved the three dimensional (3-D) Schrodinger equation using appropriate boundary conditions. The thickness of the surrounding GaAs layer is assumed to be large enough along the nanowire height and width, such that the wavefunction can be assumed to be zero at the boundaries, while periodic boundary conditions exist along the length of the nanowire. The eigen energies of the matrix Hamiltonian are then calculated. With the dimensions considered, there is only one bound state in the potential well and Figure 2.18(b) shows the energy positions of this state, which is also the ground state. It is evident that for QR height of 1.2-1.5 nm and width of 15 nm, the transition energy from the ground state to the continuum in the ring corresponds to the frequency range of 1-3THz. It is important to note that the single confined state in the quantum ring can be obtained only if they are made small. It may also be noted that we have used a simplified model for this calculation. In reality, the picture is more complex due to the actual shape of the ring and wavefunction overlap.

The quantum ring ensembles and photoconductive detectors containing multiple QR layers were grown by MBE on semi-insulating (001) GaAs substrates. The growth parameters for the initial InAs quantum dots and the anneal conditions to convert them to quantum rings were investigated and carefully tuned to produce the desired smaller size of these nanostructures. For these experiments, a 0.8 μm GaAs buffer layer was first grown at 600°C. The substrate temperature was then lowered to 530°C and 2.1 monolayers of InAs was deposited at a rate of 0.08 monolayer/sec. Self-organized quantum dots were formed following the growth of 1.8 monolayers of InAs wetting layer. A 10Å AlAs cap layer was grown on the InAs islands at 530°C. Growth was

interrupted and the capped islands were annealed at 580°C for 30 sec under an As₂ flux to form quantum rings. The function of the AlAs layer was to reduce the



(a)



(b)

Figure 2.19: (a) Heterostructure schematic of QRID grown by MBE. It has 10 layers of InAs quantum rings in the active region and a single Al_{0.2}Ga_{0.8}As barrier at the end; (b) dark current characteristics at two different temperatures (4.2 K and 80 K). Inset shows the conduction band profiles in the active region for forward and reverse bias.

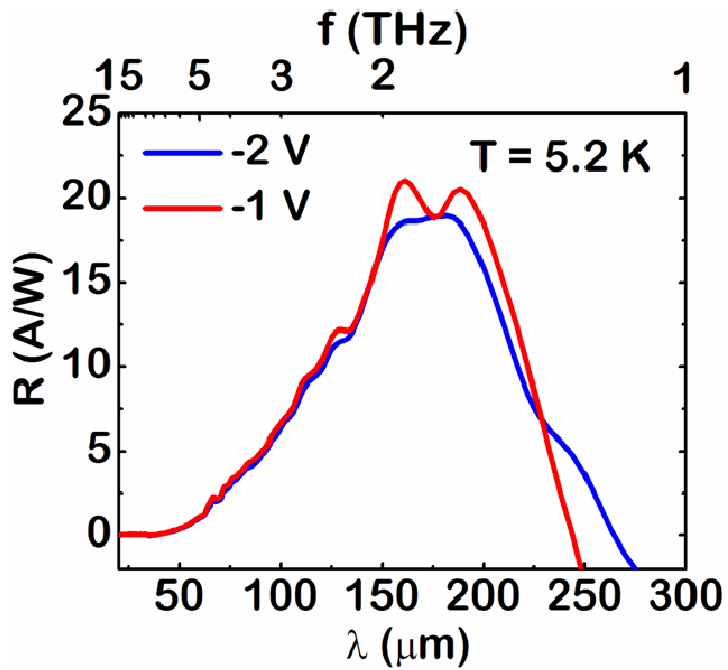
surface mobility of group III atoms on the AlAs surface since AlAs has a higher bonding strength than GaAs. Consequently, the ring shape is better preserved during the annealing process. Under these growth conditions, small quantum rings as shown in the AFM image of Figure 2.18(a) are obtained. The detector heterostructure, grown with 10 QR layers separated by 50 nm GaAs barriers, is shown in Figure 2.19(a). A single $\text{Al}_{0.2}\text{Ga}_{0.8}\text{As}$ barrier is inserted at the end. In quantum dot infrared photodetectors (QDIPs), the insertion of a single barrier layer has been very effective in reducing the dark current without substantially affecting the photocurrent [85]. The band profiles of the heterostructure for forward and reverse bias are shown in the inset of Figure 2.19(b). Mesa shaped devices for top illumination were fabricated by photolithography, wet chemical etching and n-contact metallization. The ring-shaped top contact has an inner radius of 300 μm , which defines the illumination area.

The QRIDs were characterized at cryogenic temperatures by dark current-voltage (I-V), spectral response and noise measurements. The processed detectors were mounted on chip carriers with silver epoxy and individual devices were wire bonded to separate chip carrier leads. The mounted devices were inserted in a variable temperature liquid He cryostat for I-V measurements, which was done using a Keithley 2400 Source Meter. In order to determine the spectral responsivity of the detectors, the spectral responses of the device under test and a Si composite bolometer with a known sensitivity were measured with a Perkin Elmer System 2000 Fourier Transform Infrared (FTIR) spectrometer. The two spectra were recorded with the same combination of optical windows, beam-splitter, and filters, so that the optical paths are identical. A glow-bar was used as the radiation source. In order to confirm that the detection is not due to short

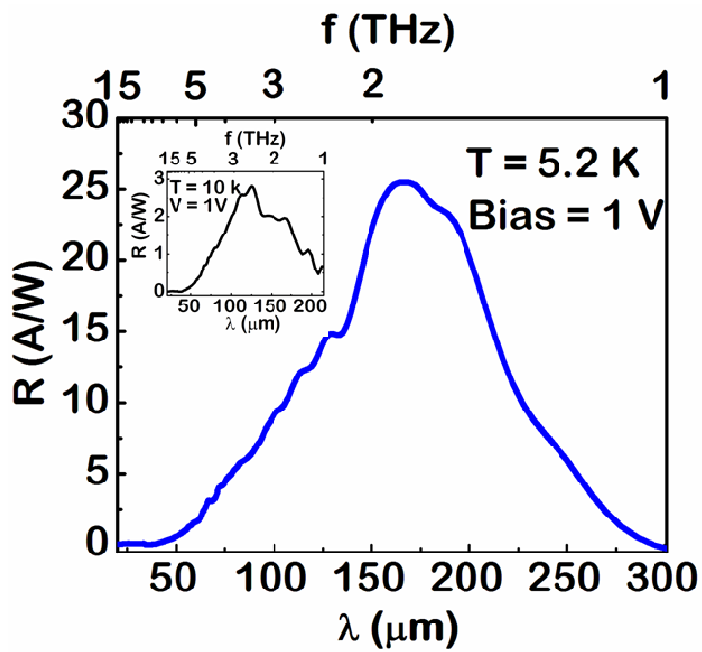
wavelength ($< 62 \mu\text{m}$) radiation, as in an optical pumping situation, a $62 \mu\text{m}$ cut-on filter was placed in front of the detector and the same detector response (but with reduced intensity due to the low transmission coefficient of the filter) was obtained. The voltage responsivity in V/W of the detectors was calculated by, $R = GSI_d/I_b$, where I_d is the raw detector spectrum, I_b is the bolometer raw spectrum, S is the bolometer sensitivity, and G is a geometrical factor which corrects for differences in the radiation-incident-area of the detector and the bolometer. To obtain the current responsivity in A/W , the voltage responsivity was divided by the effective resistance, which is the parallel combination of the load resistance R_l and the detector dynamic resistance $R_d (= dV/dI)$. The specific detectivity of the detectors at different temperatures and applied biases was obtained from, $D^* = R_p \sqrt{A}/\sqrt{S_i}$ where R_p is the measured peak responsivity, S_i is the noise current density, and A is the illuminated area of the detector. The noise current density was measured with a dual channel Fast Fourier Transform (FFT) signal analyzer and a SR570 low noise current pre-amplifier.

The measured dark current densities at 4.2 K and 80 K are shown in Figure 2.19(b). The asymmetry in the I-V curves is due to the asymmetric structure of the device and can be understood in terms of the conduction band profiles shown in the inset. It may be noted that the dark current densities are extremely low; at $T = 4.2 \text{ K}$, $J = 10^{-8} \text{ A/cm}^2$ and 10^{-6} A/cm^2 for bias of -2V and $+2\text{V}$, respectively. At $T = 80 \text{ K}$, $J = 10^{-5} \text{ A/cm}^2$ and 10^{-3} A/cm^2 for bias of -2V and $+2\text{V}$, respectively.

The calibrated spectral response of the QRIDs at different biases and temperatures are shown in Figures 2.20(a) and (b). There are several important points



(a)



(b)

Figure 2.20: Measured spectral responsivity of QRID for (a) different reverse biases measured at 5.2 K, and (b) 1V bias measured at 5.2 K. The inset to (b) shows the responsivity at 10 K under 1 V bias.

to be noted in the data. The responsivity peak at 1.82 THz (165 μm) corresponds to an energy of 7.52 meV, which agrees with the calculated ground state-to-continuum transition energy shown in Figure 2.18(b) for the ring height of 1.25 nm. The observed high peak value of the responsivity $R_p \sim 20$ or 25 A/W, depending on bias polarity is due to the fact that the number of photons per 1 W of power at long wavelengths is higher compared to that in short wavelengths. The total quantum efficiencies (internal quantum efficiency \times gain) are ~ 15 and 19 % at -1 and 1 V bias values, respectively. The $\text{Al}_{0.2}\text{Ga}_{0.8}\text{As}$ barrier layer with a height of 150 meV (assumed to be equal to the conduction band offset), does not seem to impede the transport and collection of photogenerated carriers under forward bias operation. The peak responsivity is larger under the forward bias than under the same amount of reverse bias (1V). It may be noted that the trend of the dark current is also the same. We believe that the dark current contributes to the filling of bound states in the quantum ring with electrons which eventually contribute to the photocurrent and the responsivity. Hence the trend in peak responsivity follows that of the dark current for opposite bias polarities. From Figure 2.20(b) it is evident that the responsivity decreases sharply with the increase of temperature from 5.2 K to 10 K. In fact, at 12 K, the spectral response is too weak to measure. Due to the small energy difference between the bound state and the continuum in the quantum rings, any increase in temperature leads to emptying of electrons from the bound states to the states in the continuum. This also explains the shift of the responsivity peak to a higher energy (by 2.6 meV) when the measurement temperature is increased from 5.2 K to 10 K (Figure 2.20(b)). The values of specific detectivity D^* , at a bias of 1V, derived from the measured peak responsivity and noise current, are 1×10^{16}

Jones and 3×10^{15} Jones at 5.2 K and 10 K respectively.

It is worthwhile to compare the measured characteristics of the QRIDs with those of Si and Ge bolometers that are currently used. The spectral response of the bolometers is generally uniform (flat) in the range of 2-1000 μm . In the temperature range of 0.3-4.2 K, compensated Ge bolometers have $D^* \sim 10^{14}$ Jones and the response time is 10 ms. In contrast, the QRIDs reported here exhibit a response peak at 1.82 THz, which can be tuned by varying the size of the quantum rings. The specific detectivity is $\sim 10^{15}$ Jones, even at 10 K, and higher at lower temperatures. The response time of the QRIDs, which is dependent on the emission and transport of the photoexcited carriers, is $\sim 300\text{ps}$ [86]. We do not believe that the present device can be operated at high temperatures, for reasons outlined above. But higher temperature operation can be obtained with QRIDs designed for the 3-10 THz range.

2.5 Summary

We have investigated the growth of InAs/GaAs quantum dots and dependence of their properties on different growth parameters i.e. growth temperature, growth rate and group V/III ratio by atomic force microscopy (AFM) and room temperature photoluminescence measurement. A maximum dot density of $7 \times 10^{10} \text{ cm}^{-2}$ and photoluminescence linewidth of $\sim 25 \text{ meV}$ were achieved for temperature of 510 $^\circ\text{C}$ with a V/III ratio of 35.

A detailed growth study of InAs/ $\text{In}_{0.53}\text{Ga}_{0.23}\text{Al}_{0.24}\text{As}$ quantum dots for 1.55 μm laser has also been investigated. Quantum dots are grown on $\text{In}_{0.53}\text{Ga}_{0.23}\text{Al}_{0.24}\text{As}$ lattice matched to InP substrate. Presence of As_2 and optimized temperature and V/III ratio

limits the anisotropic In diffusion length in the $[\bar{1}10]$ direction and forms quantum dots rather than quantum dashes. It has been observed that by growing a very thin GaAs layer just before growing the quantum dots significantly changes the dot morphology and dot density. A maximum dot density of $5 \times 10^{10} \text{ cm}^{-2}$ was obtained using this technique and it also improves the photoluminescence properties such as intensity and linewidth of the quantum dots.

The growth of a novel nanostructure called quantum ring is also investigated. Self-organized quantum rings are grown by insitu annealing of the self-organized quantum dots. The intraband transition energies in the quantum ring are smaller than those of the dots which make them an excellent candidate for longer wavelength detection. We report an intersubband detector with 2.3 monolayer quantum ring in the active region. The detector has a response peak at $165 \mu\text{m}$ at 5.2 K. The responsivity of the detector is measured to be $\sim 25 \text{ A/W}$.

Chapter III

Threshold Characteristics of Rolled-up Microtube Laser

3.1 Introduction

Semiconductor-based microcavities are of great interest at the present time because of a wide spectrum of applications, ranging from fundamental studies in cavity quantum electrodynamics to practical optical components and sensors. Common examples are distributed Bragg reflector (DBR)-based and photonic crystal based microcavities [87-89]. An interesting and self-forming microcavity can be realized with debonded strained semiconductor bilayers. The rolled-up microtube is formed by strain mismatch between two semiconductor layers. The basic structure is shown in Fig. 3.1. As the AlAs sacrificial layer is etched away, the rolling process starts and a complete rotation takes place. If the etching is continued, multiple rotations of the bilayer take place. However, the mismatch strain increases with continued rotation and defects can be generated. The diameter of the microtube scales according to the in-plane biaxial strain and the thickness of the bilayers. The rolling process is temporally non-linear and is also self-limiting [90], which allows precise positioning of the microtube on the starting underlayer surface. After the first demonstration by Prinz *et al* [46], there have been reports of the use of such rolled-up microcavities in coherent light sources, where a gain medium is inserted in one of the constituent layers [39-45]. Since the bilayers are

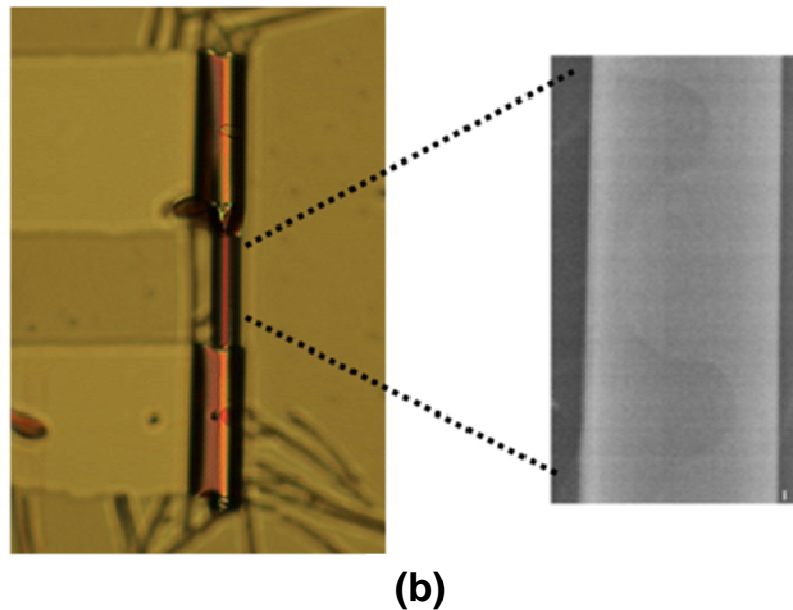
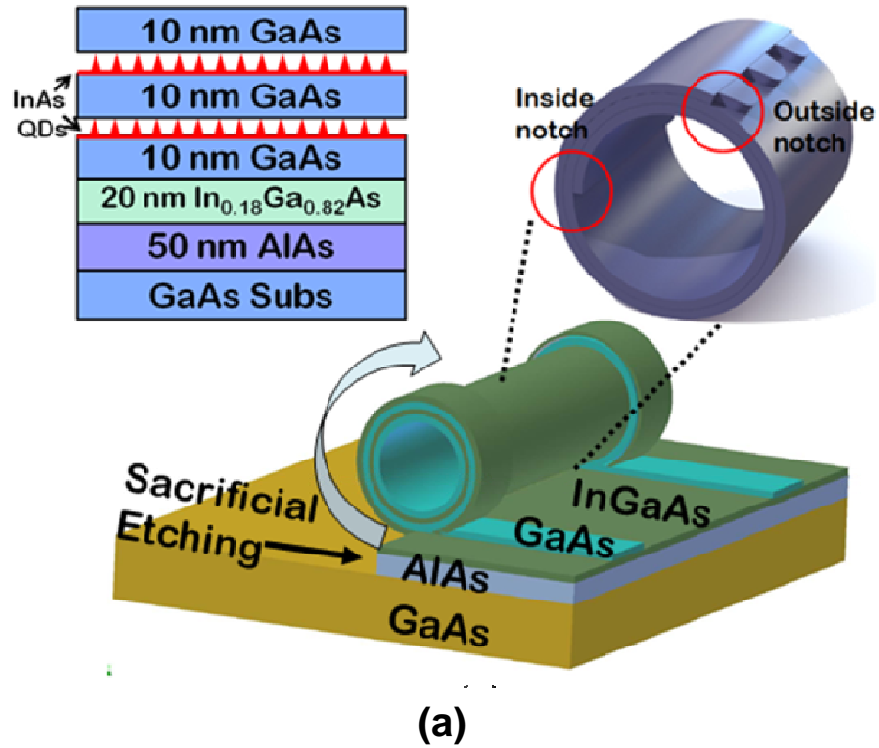


Figure 3.1: (a) Schematic representation of a free-standing rolled-up microtube. The left inset shows heterostructure of device with two layers of InAs quantum dots buried in the GaAs matrix. The bridge part of the microtube is schematically magnified in the right inset. It shows the inside and outside notches and the corrugation at the outside notch; (b) optical microscopy image of a fabricated rolled-up microtube showing the suspended bridge. The scanning electron microscopy (SEM) in the inset shows the corrugation in the bridge region of the microtube.

epitaxially grown, the rolled-up microcavity walls are atomistically smooth, which can greatly enhance the quality factor Q . Another significant advantage arises from the fact that the active (gain) medium overlaps with the maximum intensity of the optical field. As seen in the right inset of Fig. 3.1(a), the device is a cylindrical micro-sized optical ring resonator with inside and outside notches. However, there are a couple of significant differences. The rolled-up microtube is hollow and the thickness of the tube wall is much smaller than the wavelength of the light guided along the periphery. The circular symmetry present in a conventional ring resonator is broken due to the spiral geometry of the tube. It is also evident that two notches, inside and outside the tube, are formed by rolling. The scattering at the notches provide the useful output [91] and at the same time reduces the Q of the cavity. Therefore, the rolled-up microtube is approximated and analyzed as a free-standing spiral optical ring resonator with the inside and outside notches. As will be evident in a later section, the cavity resonant modes can be engineered by varying the shape of the notches [92], as shown in the right inset of Fig. 3.1(a).

Coherent emission from the rolled-up microtube is obtained by inserting quantum wells or dots in the bilayers. In particular, it is relatively simple to insert self-organized InAs quantum dots (QDs) in GaAs-based strained mismatched bilayers. To date, various groups have demonstrated optically pumped quantum dot rolled-up microtube resonators and lasers operating at room temperature [42-45]. However, the calculation of the threshold condition of these lasers and the dependence of the threshold power on key design parameters affecting the modal gain, such as the tube diameter and wall thickness, have not been done theoretically or experimentally. We present here a

relatively simplified calculation of the losses and the threshold condition, and the measured dependence of the threshold power on the diameter of InAs QD microtube lasers. The spectral emission characteristics of these devices have also been analyzed. The epitaxial growth of the strained bilayers containing InAs quantum dots and the fabrication of the rolled-up microtubes are described in Sec. 2. This section also describes the measurement and analysis of the lasing spectra from microtubes of different diameters. Section 3.3 outlines the formulation for the various losses, the modal gain and the threshold condition for microtube lasers. It is shown that the measured threshold carrier density is inversely proportional to the microtube diameter. Finally, the work is summarized in Sec. 3.4.

3.2 Experimental

3.2.1 Device Heterostructure and Fabrication

The device heterostructure, grown by molecular beam epitaxy (MBE), is shown in the left inset of Fig. 3.1(a). Two layers of InAs QDs are inserted in the GaAs layer. The dot density (N_{qd}) is determined by atomic force microscopy (AFM) is $\sim 5 \times 10^{10} \text{ cm}^{-2}$. To fabricate rolled-up free standing microcavities, a U-shaped mesa is first defined by selectively etching down to the InGaAs layer with a $\text{H}_2\text{O}_2/\text{H}_3\text{PO}_4$ mixture where the ending edge of the U-shaped body is either straight or has corrugation. The starting edge of rolling is defined by deep etching through the AlAs sacrificial layer with the same solution. The self-rolling process is initiated as the diluted hydrofluoric (HF) acid solution undercuts the InGaAs layer. The number of revolution is varied

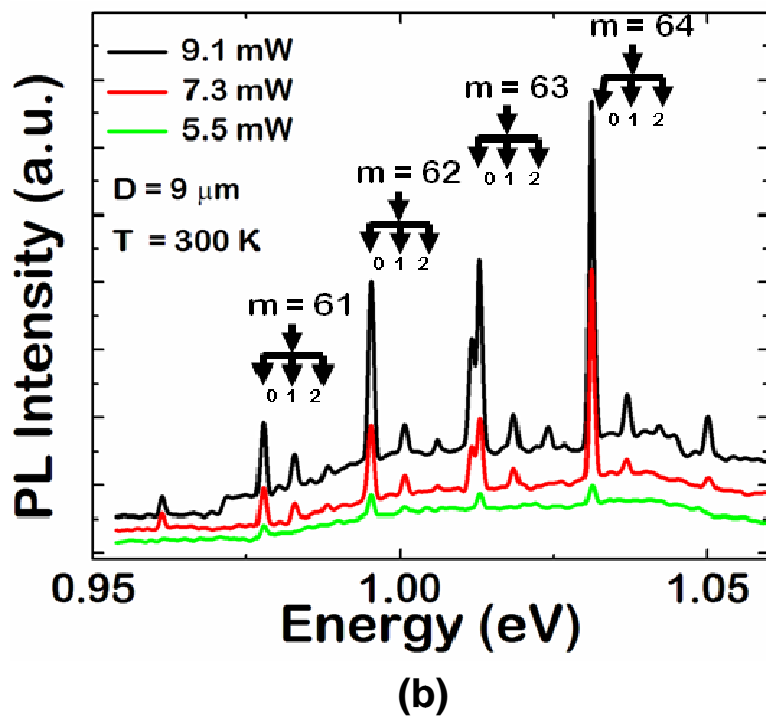
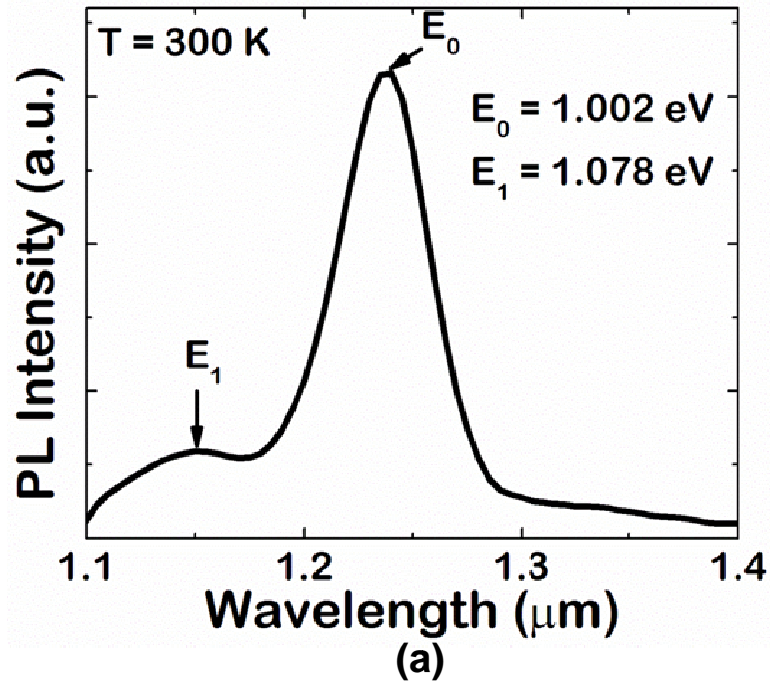
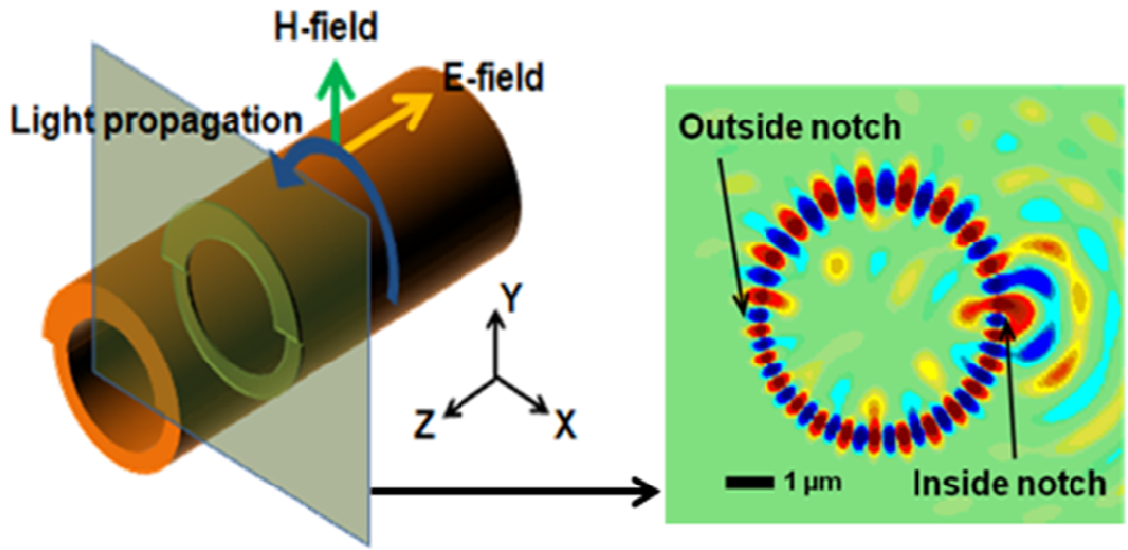


Figure 3.2: (a) Room-temperature micro-photoluminescence from the as-grown InAs quantum dot bilayers heterostructure; (b) microphotoluminescence spectra of the rolled-up microtube device of diameter $\sim 9\ \mu\text{m}$ for different incident powers. Theoretically calculated mode energies indicated in the figure show excellent agreement with the measured data.

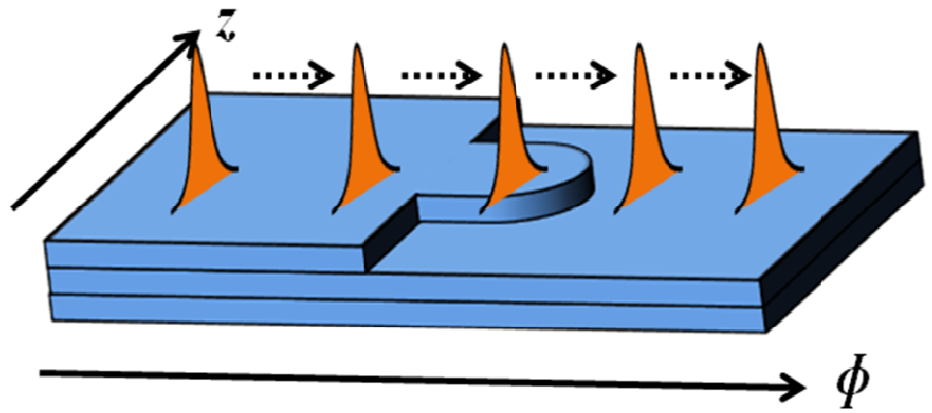
from sample to sample. The central part of the tube is suspended due to the U-shaped mesa, as seen in the micrograph of Fig. 3.1(b). For the devices used in this study, the diameter and the wall thickness of the suspended (bridge) region varied in the range 6-12 μm , and 160-130 nm, respectively. The air gap between the bridge and the substrate depends on the number of revolutions and is typically $\sim 0.5 \mu\text{m}$. The scanning electron microscopy (SEM) image of a quantum dot microtube with a corrugated notch is shown in inset of Fig. 3.1(b). All the devices characterized in this study have such corrugations at the outside notch.

3.2.2 Spectral Emission Characteristics and Modal Behavior

The emission characteristics of the QD microtube devices were determined by micro-photoluminescence (PL) measurements. The excitation from a diode laser ($\lambda = 523 \text{ nm}$) was focused to a 20 μm illumination area on the microtube with the use of a suitable objective lens. Emission from the device was collected by the same lens, analyzed by a high resolution monochromator and detected by a liquid nitrogen cooled Ge detector with lock-in amplification. All measurements have been made with the samples at room temperature. Figure 3.2(a) shows the micro-PL spectrum of an as-grown quantum dot bilayer heterostructure. The two broad peaks at $\lambda=1237$ and 1150 nm correspond to quantum dot ground state and first excited state emission, respectively. Excitation dependent micro-PL spectra from a rolled-up microtube of 9 μm diameter and ~ 130 nm wall thickness and separated from the substrate by ~ 400 nm, are shown in Fig. 3.2(b). A microtube cavity can support an azimuthal mode propagating along the circumference with the E -field along the axial direction [91]



(a)



(b)

Figure 3.3: (a) Schematic of the microtube showing the direction of light propagation, E-field and H-field for the azimuthal mode. The calculated mode profile shown in the inset indicates most of the radiation originates from the notches of the microtube; (b) schematic of equivalent planar waveguide near the notch.

(Fig. 3.3(a)). A finite difference time domain (FDTD) simulation of the azimuthal mode

profile confined in a microtube of diameter 5 μm and wall thickness 100-150 nm is shown in the inset of this figure. These modal characteristics confirm that the rolled-up microtube is a cylindrical micro-sized ring resonator with inside and outside notches. From this figure, it is evident that photons are predominantly emitted by scattering at the inside notch. The sharp peaks observed in the emission spectra of Fig. 3.2(b), are identified to be the azimuthal modes separated by ~ 18 meV which satisfy the phase matching conditions of a ring resonator given by: $\pi D n_{eff} = \lambda m$. Here D , n_{eff} , λ , and m are, respectively, the tube diameter, effective refractive index of the bi-layer, resonant wavelength and the azimuthal mode number. The minimum linewidth of the resonant peaks is ~ 0.8 nm. In addition to the azimuthal modes, we observe additional peaks in the spectra of Fig. 3.2(b). These arise from the axial confinement of modes due to the corrugation at the outside notch, shown in Fig. 3.1(b). With respect to the schematic representation of Fig. 3(b) showing equivalent planar waveguide near the notch, Maxwell's equation for the z component of the electric field $E_z(\Phi, z)$ is given by [43]

$$-\frac{1}{n_{eff}^2(z)} \left[\frac{\partial^2 E_z(\Phi, z)}{\partial z^2} + \frac{\partial^2 E_z(\Phi, z)}{\partial \Phi^2} \right] = k^2 E_z(\Phi, z) \quad (3.1)$$

Considering the phase matching condition along the circumference of the microtube and expressing $E_z(\Phi, z) = e^{j\beta\Phi} \varphi(z)$, we get

$$-\frac{\partial^2 \varphi(z)}{\partial z^2} - n_{eff}^2(z) k^2 \varphi(z) = -\beta^2(z) \varphi(z) \quad (3.2)$$

Due to the corrugated surface geometry of the microtube, $n_{eff}(z)$ is different at different positions along the z -axis of the microtube which essentially produces three dimensional confinement for the propagating light along the axial direction and results in discrete transverse modes supported by the microtube. The eigenmodes of

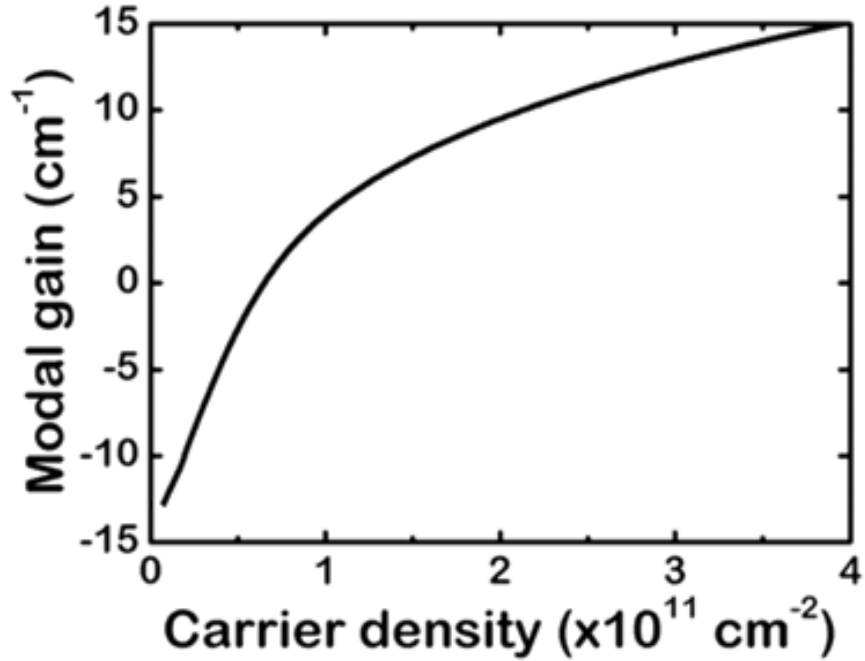


Figure 3.4: Theoretically calculated modal gain versus carrier density in a InAs quantum dot layer.

the resonator results from the interaction of these transverse modes with different azimuthal modes defined by $\beta = 2\pi m/l$, and discussed earlier [43], l is the circumference of the tube. In this study, we have fabricated microtubes with semicircular corrugation of diameter $\sim 10 \mu\text{m}$. The measured peaks in the spectra (shown in Fig. 3.2(b)) show excellent agreement with the calculated resonances.

3.3 Lasing Characteristics, Modal Gain and Threshold Condition

Our objective was to understand the role of various losses and of a key parameter, the diameter of the microtube, on the threshold behavior of the laser. For this, we have formulated and calculated the modal gain and derived the analytical form

of the important losses. The threshold condition is then obtained.

3.3.1 Modal Gain

The gain of the devices investigated in this study is provided by a couple of layers of InAs self-organized quantum dot layers. The dots are generally assumed to be of pyramidal shape with base diameter and height of 20-30 nm and 6-7 nm, respectively. The dot density (N_{qd}) is $\sim 5 \times 10^{10} \text{ cm}^{-2}$. The modal gain of the QD active region is given by [93, 94]:

$$g(E) = \frac{2\pi e^2 \hbar \Gamma}{c n_r \epsilon_0 m_0^2} \left(\frac{N_{qd}}{t_{qd}} \right) \sum_i \frac{|P_{cv}^\sigma|^2}{E_i} [f_n(E) - f_p(E)] \cdot G(E - E_i)$$

(3.3)

where Γ is the confinement factor and is ~ 0.01 , t_{qd} is the thickness of a quantum dot layer, $f_{n(p)}(E)$ are the Fermi distribution functions for electrons (holes) and $G(E - E_i) = \frac{1}{\sqrt{2\pi}\sigma} \exp\left[-\frac{(E-E_i)^2}{2\sigma^2}\right]$ is the Gaussian distribution function with a full width at half maximum (FWHM) equal to σ to take into account the inhomogeneous broadening of the dot photoluminescence lineshape due to QD size variation. The value of $\sigma = 36 \text{ meV}$ is taken from measured PL spectra. In order to calculate the Fermi levels for electron and holes and the distribution functions for different carrier injection levels, the following relation is used:

$$n = \int_{E_g}^{\infty} \sum_i s_i N_{qd} f_n(E) \delta(E - E_i) dE = \sum_i s_i N_{qd} f_n(E_i) dE \quad (3.4)$$

where it is assumed that the QDs have delta-function like density of states. s_i is the degeneracy of each confined level. It may be noted that in addition to a spin degeneracy of two, the excited level in each dot has a twofold degeneracy due to the

symmetry of the dot geometry. The energy levels in the pyramidal InAs quantum dots are known to be those of a harmonic oscillator Hamiltonian [94, 95]. The energy levels used in this calculation are extracted from the transition energies in the photoluminescence spectra of the dots before the formation of the microtube (Fig. 3.2(a)): the ground state energy $E_0 = 1.002$ eV and the first excited state $E_1 = 1.078$ eV. Since the lasing emission of the QD microtube was observed only from the ground state, gain calculations were restricted only to ground state transitions. The calculated modal gain of the ground state per dot layer, as a function of carrier density is depicted in Fig. 3.4. The transparency carrier density is $\sim 7 \times 10^{10}$ cm⁻².

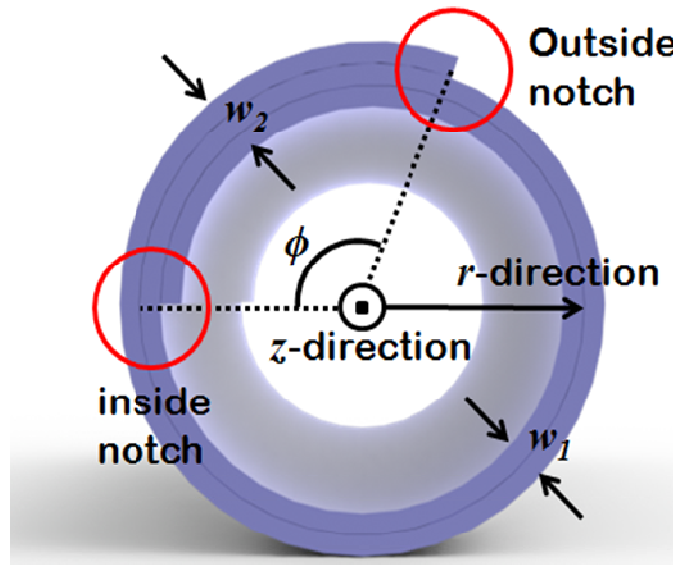
In order to derive the threshold condition, the microtube is approximated as a ring resonator consisting of two different wall thicknesses, w_1 and w_2 and two notches, inside and outside as shown in Fig. 3.5(a). Since the wall thickness is much smaller than the microtube diameter, a uniform diameter of D is assumed. The losses in the microtube are the bending loss α_{bend} while light travels along the curvature of the tube circumference, radiation loss $R_n (= 1 - T_n)$, where T_n is the transmission, at the notches due to the step discontinuities, and optical loss into the substrate. The change in the light intensity after one round trip is then expressed as:

$$I = I_0 T_1 T_2 \exp[(\Gamma g - \alpha_{\text{bend}1})l_1 + (\Gamma g - \alpha_{\text{bend}2})l_2 - \alpha_{\text{sub}}l] = I_0 \quad (3.5)$$

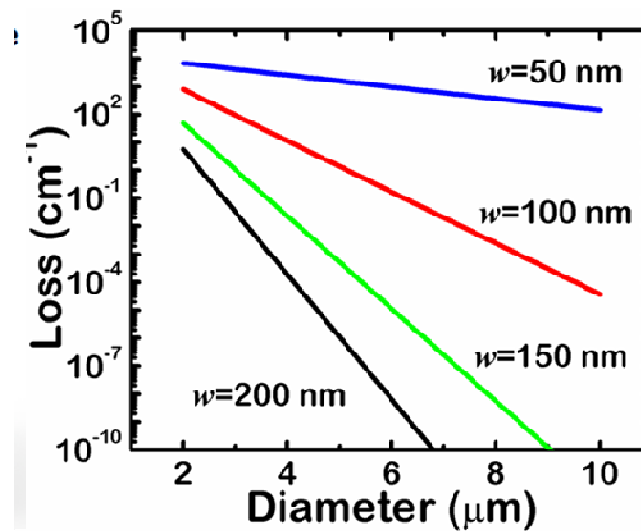
where $l_1 = D(\pi\phi)$, $l_2 = D\phi/2$ and $l = l_1 + l_2$. $\alpha_{\text{bend}1}$ and $\alpha_{\text{bend}2}$ are bending losses in the microtube section of thickness w_1 and w_2 , respectively, and α_{sub} is the substrate loss. The threshold condition is then expressed as:

$$\Gamma g_{\text{th}} = \frac{(\alpha_{\text{bend}1}l_1 + \alpha_{\text{bend}2}l_2)}{l} + \frac{1}{l} \ln\left(\frac{1}{T_1 T_2}\right) + \alpha_{\text{sub}} \quad (3.6)$$

where Γg_{th} is the modal gain at threshold.



(a)



(b)

Figure 3.5: (a) Schematic cross section of a microtube showing different wall thickness (w_1 and w_2) at different positions along the tube periphery. The r -direction is the outward direction from origin at the center of the ring to the wall and the z -direction is the direction out of the paper; (b) calculated bending loss as a function of diameter for different wall thicknesses.

3.3.2 Bending Loss α_{bend}

With reference to Fig. 3.5(a), the wave equation in cylindrical coordinates for a wave propagating along the circumference (TE mode):

$$\frac{d^2 E_z}{dr^2} + \frac{1}{r} \frac{dE_z}{dr} + \left[k_0^2 n_r^2(r) - \frac{\beta^2}{r^2} \right] E_z = 0 \quad (3.7)$$

is solved [96]. The bending loss is evaluated as the ratio of radiated power to the total power and is derived as:

$$\alpha_{bend} = K[\exp(-S)] \quad (3.8)$$

with $K \approx \frac{2p^2 h^2}{v^4(hw+2)} k_0(n_{rs} - n_{ra})$ and $S \approx \frac{h^3}{3v^3} qD$ after some approximations. Here n_{rs} and n_{ra} are, respectively, the refractive indices of the microtube (average of the bilayers) and air. $h = (\beta_0^2 - k_0^2 n_{ra}^2)^{1/2}$ and $p = (k_0^2 n_{rs}^2 - \beta_0^2)^{1/2}$ are the transverse phase constant and the transverse decay constant, respectively, of an equivalent waveguide without any bending, where β_0 is the propagation constant, $v^2 = (h^2 + p^2)$, w is the average wall thickness, and $q = n_{rs} k_0 \left[2 \left(1 - \frac{n_{ra}}{n_{rs}} \right) \right]^{3/2}$. Equation (8) gives a fairly accurate estimate of the bending loss for small wall thicknesses. The bending loss is plotted in Fig. 3.5(b) for different microtube wall thickness values and is evident that $\alpha_{bend} \propto \exp(-D)$.

3.3.3 Radiation Loss

A wave traveling along the circumference of the microtube experiences step discontinuities at the two notches and there is radiation of power. This is modeled as a straight waveguide with a step discontinuity, schematically shown in Fig. 3.6(a) with

$$\text{and } |c_T|^2 + |e_R(\kappa)|^2 + |e_T(\kappa)|^2 = 1$$

the radiation rate can be expressed as

$$\frac{P_{rad}}{P_{in}} = \int_{-k_0 n_a}^{k_0 n_a} \left(\frac{\beta_r + \beta_1}{4\omega\mu_0} \right)^2 (I_m^2 + I_n^2) \frac{|\beta_r|}{\kappa} d \quad (3.10)$$

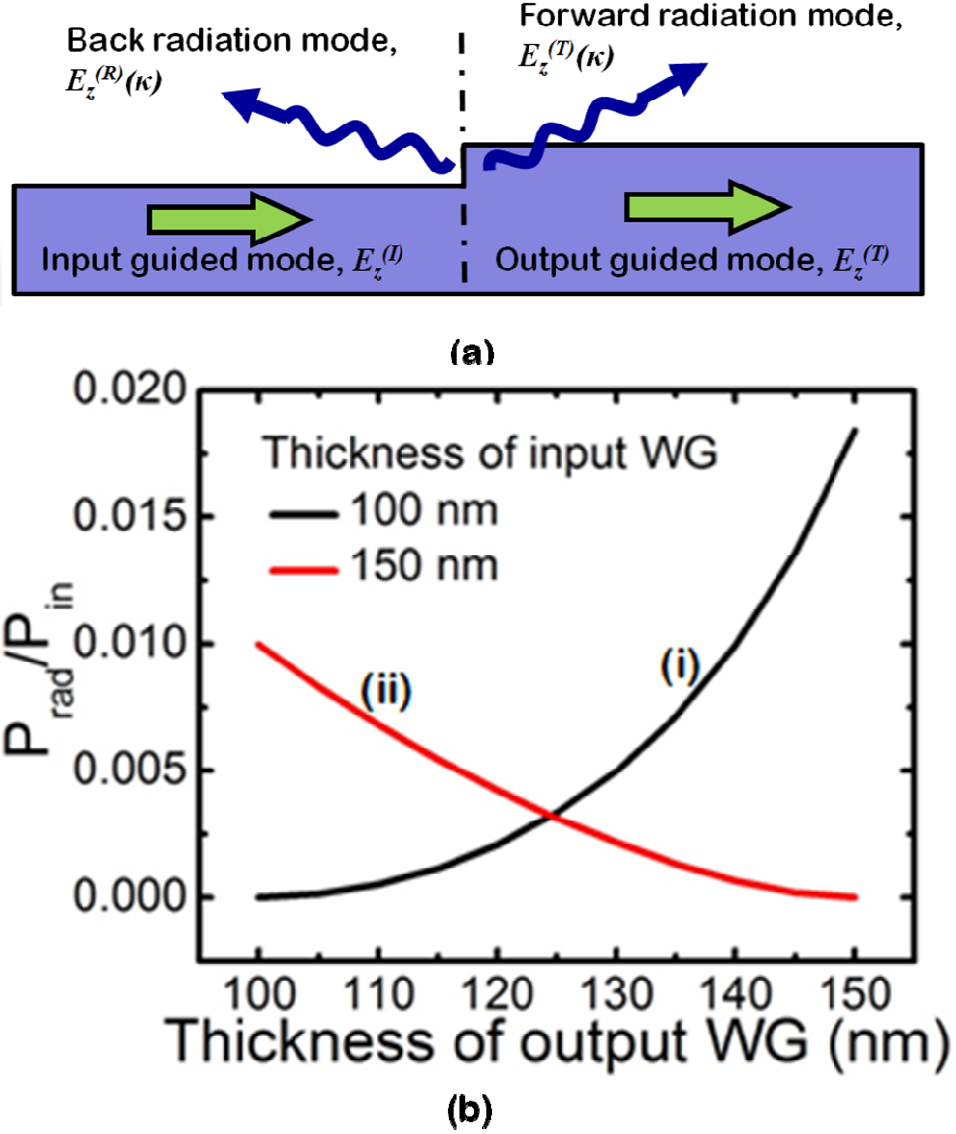


Figure 3.6: (a) Schematic representation of scattering losses at the step discontinuity of a notch of the microtube; (b) radiation loss as a function of output waveguide thickness.

where,

$$I_{m,n} = \int_{-\infty}^{\infty} E_z^{(I)} E_{zm,n}^{(T)} dx$$

Here $e_R(\kappa)$, $e_T(\kappa)$, and c_T are the amplitude coefficients of the backward traveling radiation mode, the forward traveling radiation mode, and the transmitted guided mode, respectively. β_1 is the propagation constant of the input waveguide. The calculated scattering losses as a function of output waveguide thickness are depicted in Fig. 3.6(b). The curves (i) and (ii) represent scattering losses for the wave traveling from a wall with $w = 100$ nm to the wall of larger w , and in travelling from a wall with $w = 150$ nm to the wall of smaller w , respectively. It is evident that for a rolled-up microtube with wall thickness $w_1 = 100$ nm and $w_2 = 150$ nm, the rate of radiation at the two notches are $R_1 = 0.01$ and $R_2 = 0.08$, knowing that $T_1 = 1 - R_1$ and $T_2 = 1 - R_2$. The total radiation loss at the notches can be expressed as

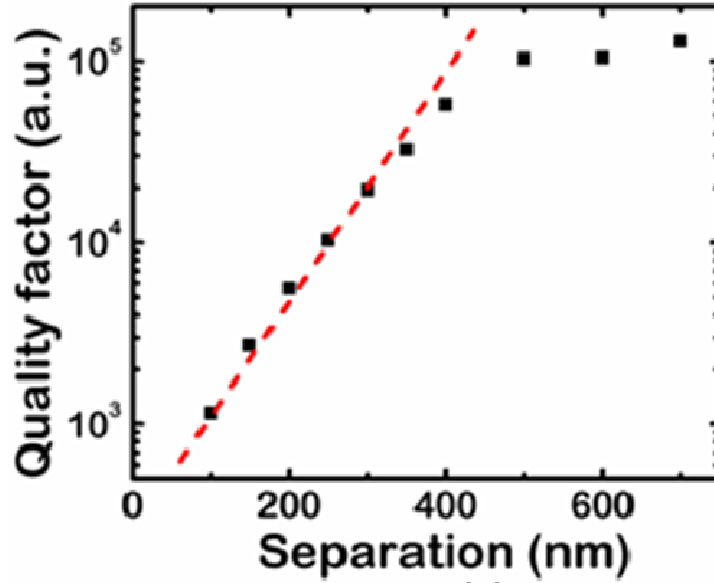
$$\alpha_{rad} = \frac{1}{l} \ln \left(\frac{1}{T_1 T_2} \right) = \frac{1}{\pi D} \ln \left(\frac{1}{T_1 T_2} \right) \quad (3.11)$$

3.3.4 Substrate Loss

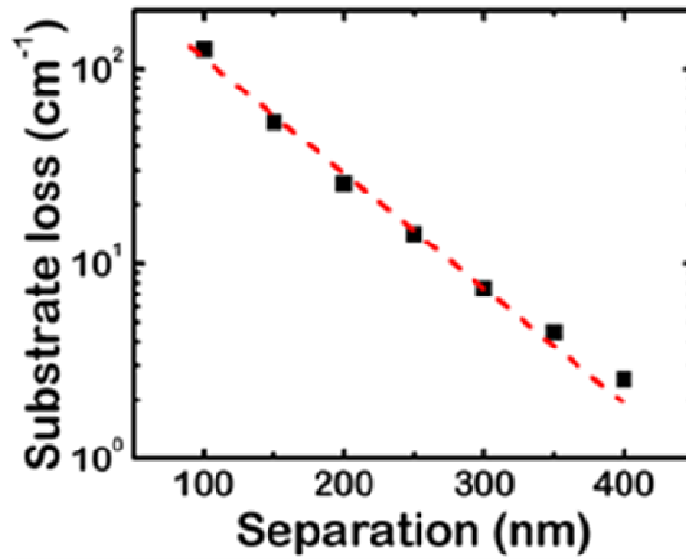
As seen in Fig. 3.1(b), the bridge region of the rolled-up microtube is separated from the substrate. However, this separation is strongly dependent on the number of revolutions to form the microtube and the resulting wall thickness. The substrate loss is expressed as:

$$\alpha_{sub} = \frac{2\pi n_{eff}}{\lambda} \cdot \frac{1}{Q} \quad (3.12)$$

We have performed an FDTD simulation of the Q-factor as a function of the microtube-to-substrate separation and the corresponding substrate loss is obtained



(a)



(b)

Figure 3.7: (a) Dependence of the microtube cavity quality factor Q on the separation of the tube from the substrate; (b) substrate loss in the microtube cavity versus separation from substrate. The dashed lines are guides to the eye.

from Eqn. (12). These parameters are plotted in Figs. 3.7(a) and (b). It is evident that for a separation less than 400 nm, the Q -factor decreases exponentially due to leakage of energy into the substrate. For larger separation, as is the case of the devices fabricated

for this study ($\sim 0.5 \mu\text{m}$), the substrate loss can be ignored. The calculated bending and radiation losses are compared in Fig. 3.8(a) for microtubes of varying diameters. The bending loss becomes important only for very small diameter microtubes. Therefore for the microtubes fabricated and characterized in the present

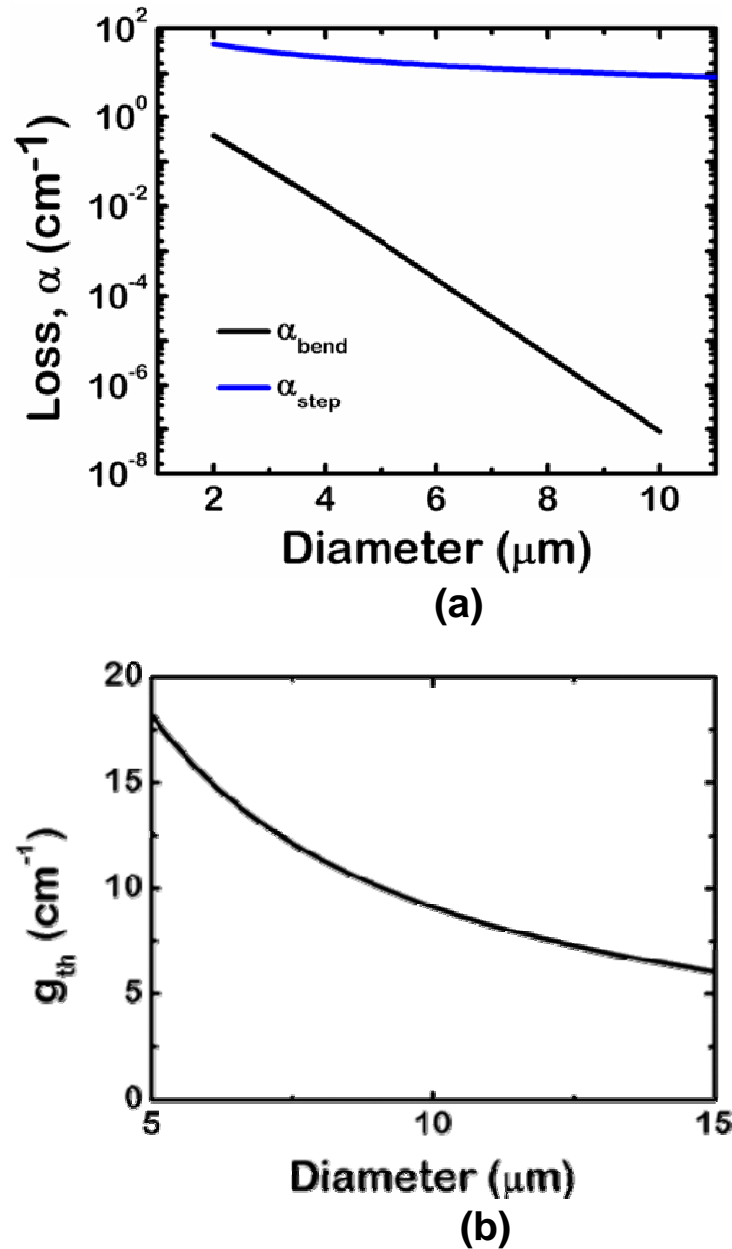
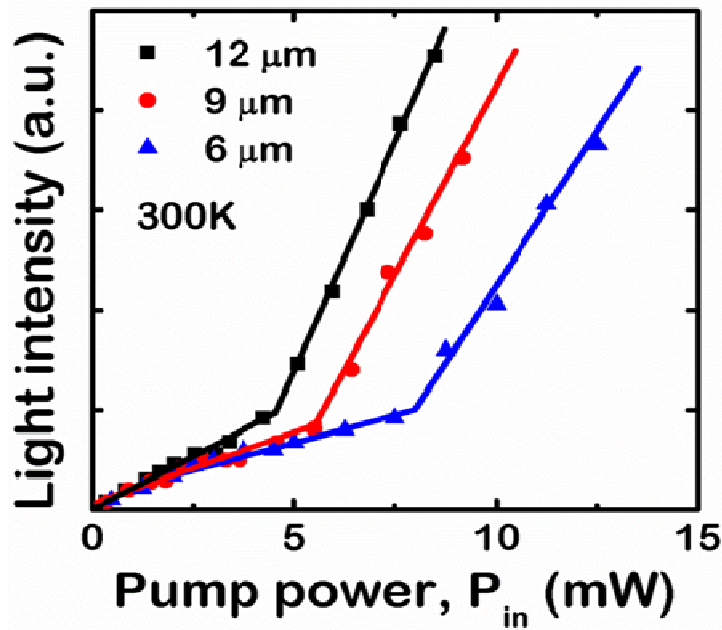
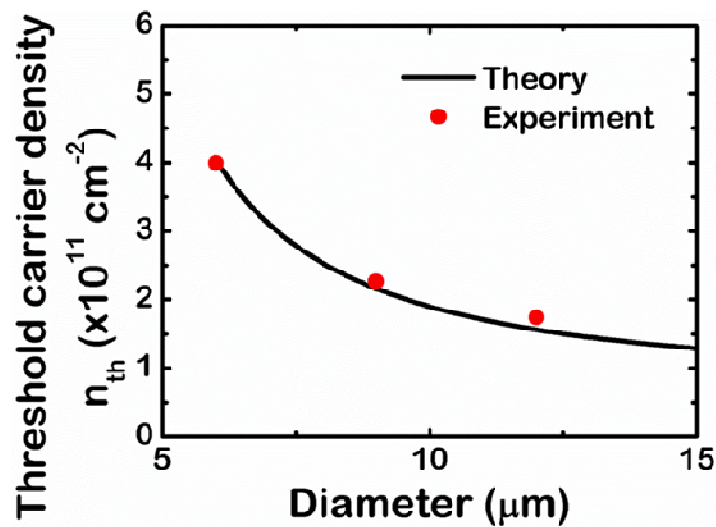


Figure 3.8 (a) Comparison of radiation loss at a step notch and bending loss in the microtube cavity as a function of tube diameter; (b) calculated threshold gain versus diameter in the microtube laser.



(a)



(b)

Figure 3.9 (a) Output light intensity versus incident pump power for different diameter quantum dot microtube lasers; (b) variation of threshold carrier density in active region of the lasers with microtube diameter.

study, the dominant loss mechanism is scattering and radiation at the notches. The threshold condition then becomes

$$\Gamma g_{th} \cong \frac{1}{\pi D} \ln \left(\frac{1}{T_1 T_2} \right) \quad (3.13)$$

and the a plot of this equation is shown in Fig. 3.8(b) for w_1 and w_2 equal to 100 nm and 150 nm, respectively.

3.3.5 Dependence of QD Laser Threshold on Microtube Diameter

The measured output light intensity versus pump power for QD microtube lasers of varying diameter are depicted in Fig. 3.9(a). The threshold carrier density in the quantum dots is obtained from the incident and absorbed power (Table 3.1) for

Table 3.1: Calculation of threshold carrier densities from excitation power

Diameter	6 μm	9 μm	12 μm
Layer thickness (d)	55 nm	66 nm	77 nm
Number of revolutions	2.92	1.95	1.46
P_{in} (mW)	8	5.1	4.25
P_{pump} (W/cm ²)	1473.7	939.5	782.9
P_{abs} (W/cm ²)	373.1	211.4	162.5
n_{th} ($\times 10^{11}$ /cm ²)	3.99	2.26	1.74

$$P_{abs} = P_{pump} \times T \times [1 - \exp(-\alpha \cdot 2w)] \times \frac{1}{2}$$

$$n = \frac{P_{abs} \times \tau}{E_{pump}}$$

$$T = 0.7$$

$$E_{pump} = 2.335 \text{ eV}$$

$$\tau = 400 \text{ ps}$$

$$w = d \times (\text{num. of revolutions})$$

each device and is plotted as a function of device diameter in Fig. 3.9(b). The solid line

is the calculated trend, using the variation of modal gain with tube diameter (Fig. 3.8(b)) and with the carrier density in the active region (Fig. 3.4) and there is an excellent agreement between the two sets of data. The threshold carrier density in the active region is therefore inversely proportional to the microtube diameter.

3.4 Summary

We have investigated the spectral characteristics and threshold behavior of GaAs-based rolled-up microtube lasers with self-organized InAs quantum dots as the gain media. The spectral output has been analyzed and is understood in the framework of mode confinement and scattering in the corrugated regions at the notches and mode propagation as in a cylindrical ring resonator. Simplified analytical expressions have been derived for the scattering (radiation) loss at the microtube notches, the bending loss and the substrate loss and their values have been calculated as a function of tube diameter. It is seen that the radiation loss is the dominant loss mechanism in these devices. The threshold condition for a microtube laser has been derived from which it is found that the threshold excitation (power) is inversely proportional to the microtube diameter. This result is borne out by the measured data.

Chapter IV

Quantum Dot Rolled-up Microtube Directional Coupler

4.1 Introduction

The directional coupler has become an important component in optoelectronic and photonic integrated circuits since the theory of its operation was first outlined by Marcatili [97]. In addition to couplers made of semiconductors, for the above mentioned applications, they have been realized with a variety of other dielectrics and optical fibers [98, 99] and are used in interferometers, switches, add-drop filters and sensors [100-105]. A directional coupler usually consists of two passive optical guides in close proximity, such that the mode guided in one of them is coupled to the other over a characteristic distance termed the coupling length. This length is determined by the index of the coupling medium and the properties of the guides and can be determined from a solution of the coupled mode equations which describe the system. A coupler made of passive semiconductor waveguides is constrained by the fact that the optical excitation, or the signal that is launched into the coupler, must be guided with low loss by the constituent guides and must therefore have a photon energy smaller than the energy bandgap of the semiconductor. On the other hand, an active coupler is made of coupled active waveguides. An edge-emitting semiconductor laser, for example, consists of an active waveguide with the light emitting gain region and

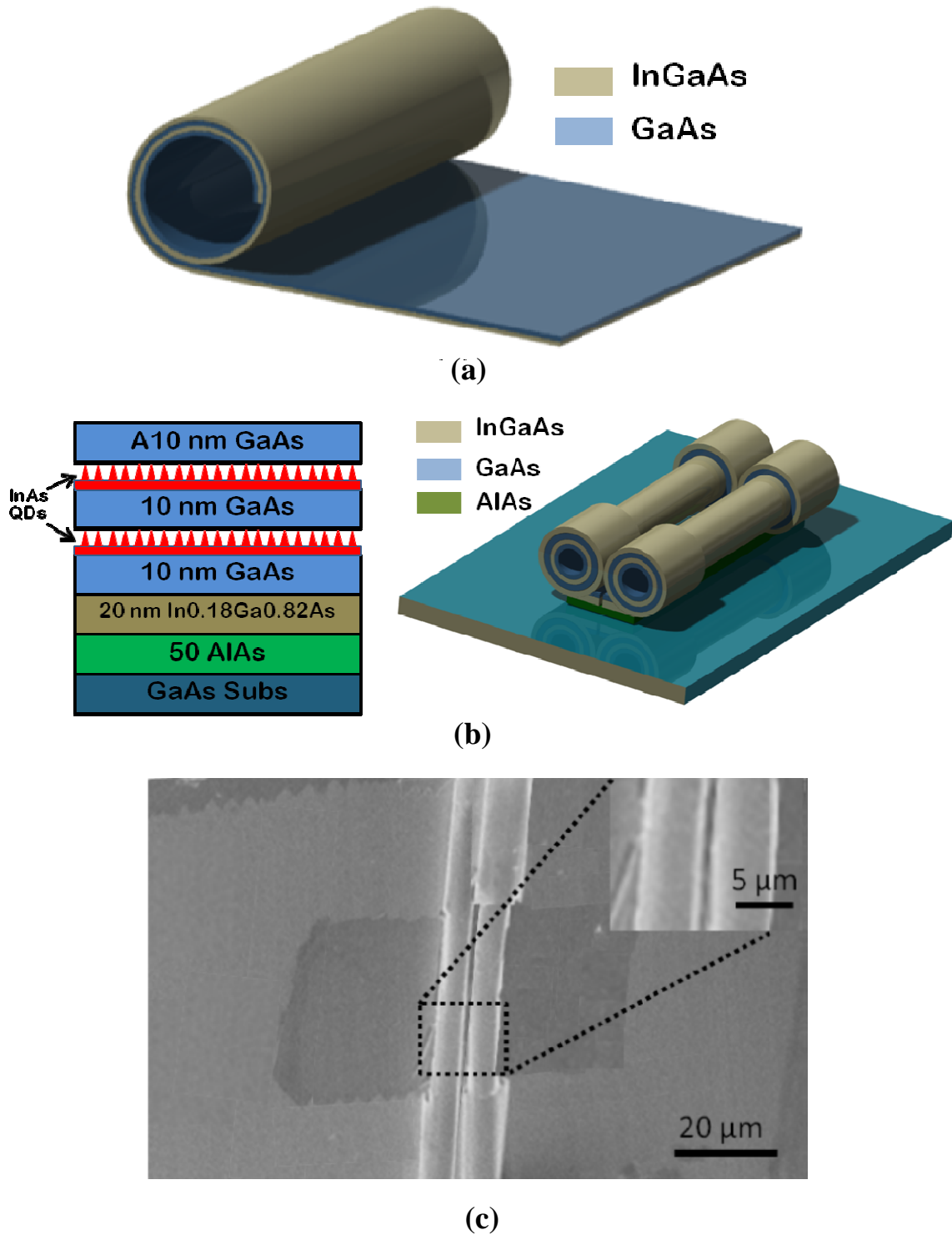


Figure 4.1: (a) Schematic representation of rolling mechanism; (b) schematic representation of GaAs-based heterostructure and the rolled-up microtube coupler. The heterostructure is grown by MBE and has two layers of InAs quantum dots embedded in the GaAs matrix; (c) scanning electron microscopy (SEM) image of a microtube coupler with the inset showing an enlarged region of the microtubes.

the end mirrors realized by cleaving or etching. An active directional coupler can be excited by light of any photon energy larger than the bandgap of the active medium. We report here a directional coupler made with active rolled-up microtubes and its possible use in sensing applications. The microtubes are formed from strained InGaAs/GaAs bilayers containing self-organized InAs quantum dots.

The formation of a rolled-up microtube directional coupler is based on the differential biaxial strain between epitaxially grown nanometer thick bilayers and their debonding from the underlayer surface (Fig. 4.1(a)) and the rolling mechanism have been discussed elaborately in chapter 3. We investigate here, the properties of a directional coupler made of twin tubes [106] formed by bringing two active microtubes in close proximity. The microtubes are formed from an epitaxially grown $\text{In}_{0.18}\text{Ga}_{0.82}\text{As}/\text{GaAs}$ bilayer with two layers of self organized InAs quantum dots (QDs) inserted in the GaAs layer (Fig. 4.1(b)).

4.2 Device Heterostructure and Fabrication

The strained bilayer heterostructure with InAs quantum dot layers, shown in Fig. 4.1(b), is grown by molecular beam epitaxy on (001) GaAs substrate. The quantum dot density N_{qd} in each dot layer was determined by atomic force microscopy (AFM) measurements on a control sample and is $\sim 5 \times 10^{10} \text{ cm}^{-2}$. Two U-shaped mesas facing each other are first defined by selectively etching down to the InGaAs layer with a $\text{H}_2\text{O}_2/\text{H}_3\text{PO}_4$ mixture. The starting undercuts the InGaAs layer and initiates the self-rolling process. Two microtubes roll towards each other and stop when their arms touch. The process is schematically illustrated undercuts the InGaAs layer and initiates the self-

rolling process. Two microtubes roll towards each other and stop when their arms touch. The process is schematically illustrated in Fig. 4.1(b). The tubes are identical and the diameter and wall thickness of the microtube are $\sim 6\ \mu\text{m}$ and $150\ \text{nm}$, respectively. The central part of the tube is suspended due to the U-shaped mesa, as seen in Fig. 4.1(b). The gap between the bridge and the substrate depends on the number of turns and is typically $\sim 0.5\ \mu\text{m}$. A scanning electron microscope (SEM) image of the fabricated microtube directional coupler is shown in Fig. 4.1(c). The separation between the two microtubes is $\sim 700\ \text{nm}$.

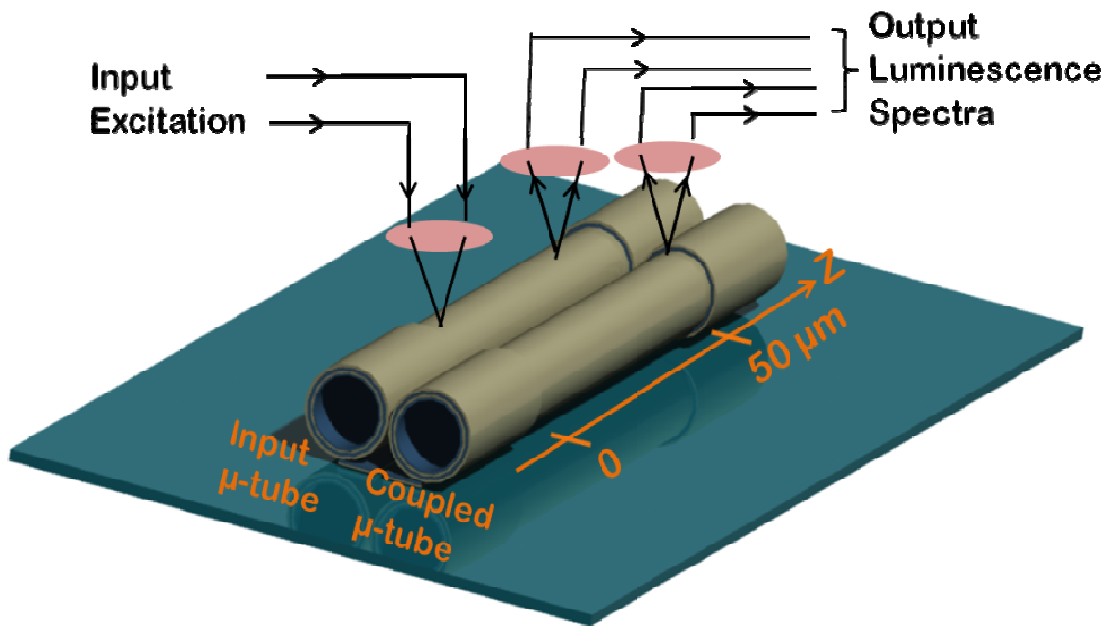


Figure 4.2: Schematic of the measurement procedure. The output objective lens is swept along the z-direction to obtain the luminescence spectra at different positions on the input and coupled microtubes.

4.3 Directional Coupler Characteristics

The principle of operation is illustrated in Fig. 4.2. Optical excitation is provided at one end of the input microtube. The quantum dot luminescence that is generated propagates along its length and couples to the output microtube, via the evanescent mode. At the same time, part of the luminescence that is generated is lost as outwardly radiating modes and represents a guide loss. Depending on the length of the two microtubes, the optical energy will oscillate between them with a characteristic coupling length l_c , which will depend on the separation of the two microtubes and the index of the coupling medium. It may be noted that because of the hollow tubes with large surface-to-volume ratio, there is a larger interaction of the optical modes with the surrounding medium, compared to conventional waveguide directional couplers, and this aspect is helpful for sensing applications. The coupling of light between the microtubes was analyzed by the three-dimensional FDTD method. A continuous wave (cw) light source excites and launches a mode at one end of the input microtube, similar to the experiments, and the optical power is monitored as a function of distance along the axis of both microtubes. The losses mentioned above are taken into account in the analysis. The solid curves in Fig. 4.3(b) represent the calculated normalized power in both microtubes when they are separated by 700 nm, and show good agreement with the measured results. The value of the coupling length l_c is estimated to be $\sim 45 \mu\text{m}$. The calculations were repeated for various separations between the two microtubes and the coupling lengths were derived in the same manner. Figure 4.4 shows that the coupling length increases exponentially when the separation is linearly increased. The evanescent field which is responsible for

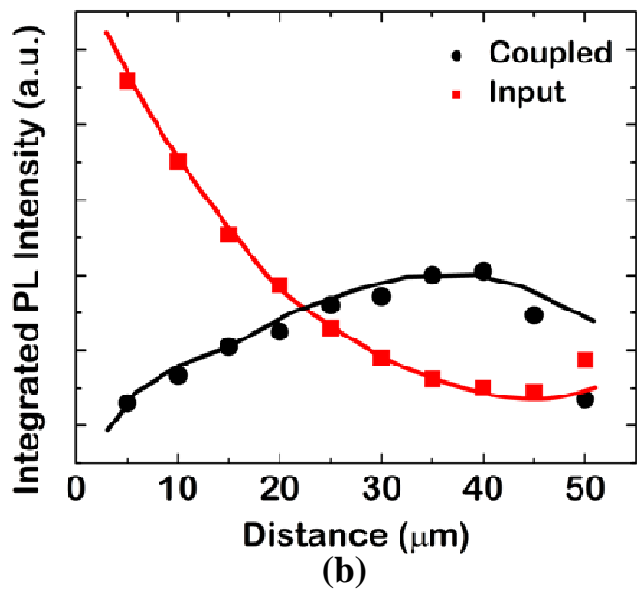
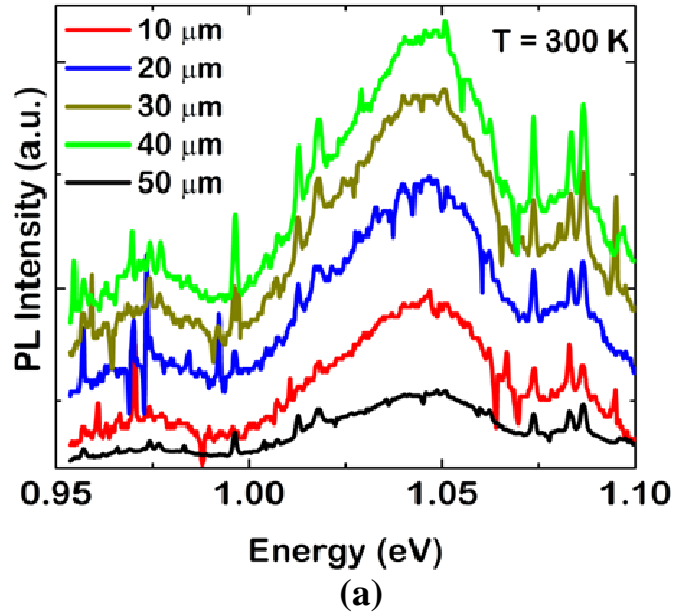


Figure 4.3: (a) Measured photoluminescence spectra at different positions on the coupled microtube in air; (b) integrated photoluminescence intensity vs. distance on the input and output microtube. Solid lines are calculated intensities using the finite difference time domain technique. coupling light between the microtubes decays exponentially outside them. Hence, a smaller amount of optical energy is coupled and l_c increases exponentially.

4.4 Liquid Sensing Application

The use of single microtube resonators for sensing and detection of fluids, embryonic cells and micro- and nano-organisms and as magnetic sensors has been

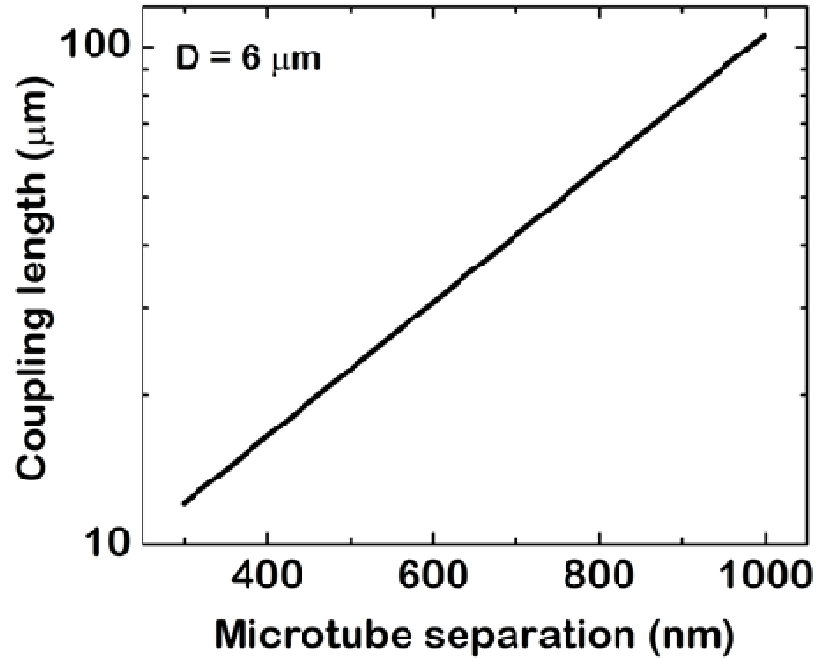
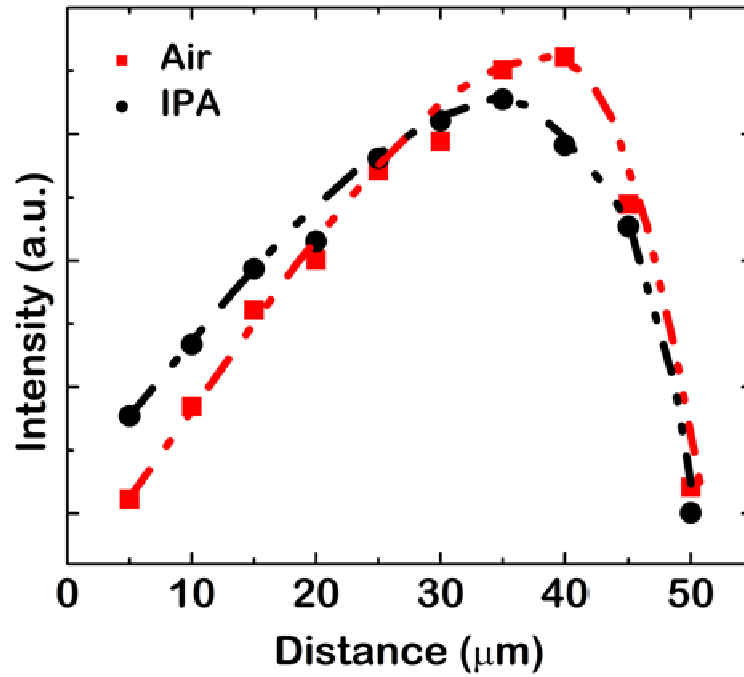
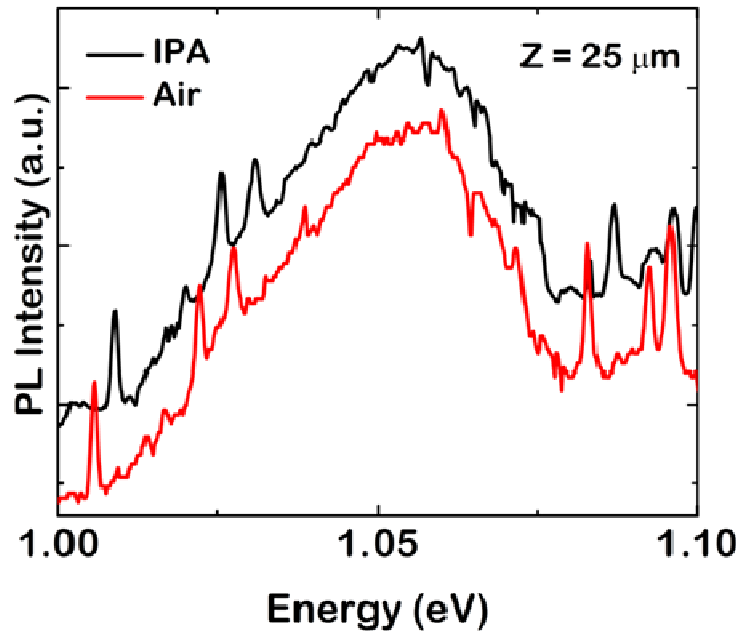


Figure 4.4: Calculated variation of coupling length l_c vs. the microtube separation.

reported [107-110]. We have explored the possibility of using the rolled-up microtube coupler for sensing applications. The inner and outer surfaces and the inner hollow region uniquely provide a 3D microstructure to interact with the environment for such applications. Figure 4.5(a) shows the spectra from the coupled microtube recorded at a distance of $25 \mu\text{m}$ along the axis, with 532 nm excitation to the input microtube, for air and isopropyl alcohol (IPA) surrounding media. The spectra have been displaced arbitrarily along the vertical axis for clarity. The relative shift of the resonant peaks is due to the difference in refractive index between air and IPA. Figure



(a)



(b)

Figure 4.5: (a) Measured photoluminescence spectra from coupled microtube at a distance of $25 \mu\text{m}$ in air and isopropyl alcohol (IPA) as the coupling media. The spectra are displaced arbitrarily along the vertical axis for clarity; (b) integrated photoluminescence intensities vs. distance along the axis of the coupled microtube in air and IPA. Dashed lines are guides to the experimental data.

5.5(b) depicts the measured integrated light intensity as a function of distance in the coupled microtube for air and IPA as the coupling media. The coupling lengths in IPA and air are $\sim 35 \mu\text{m}$ and $\sim 40 \mu\text{m}$, respectively. Because of this difference, caused by the difference in refractive index, there is a relatively large difference in intensity at $\sim 40 \mu\text{m}$ ($\sim 18\%$ for an index difference of 0.378). Thus the microtube coupler can be used for very sensitive microfluidic detection, where a small change in refractive index of the coupling medium can generate a large change in light intensity measured in the coupled guide. The measurement of the emission spectra is not required in such a sensing scheme.

4.5 Summary

In summary, we report a directional coupler with GaAs-based rolled-up InGaAs/GaAs bilayer microtubes, having InAs self-organized quantum dots buried in the GaAs layer. The insertion of quantum dots inside the directional coupler makes it capable of working at any excitation wavelength. The use of the directional coupler for potential liquid sensing applications has also reported.

Chapter V

Rolled-up Microtube Phototransceiver

5.1 Introduction

Optoelectronic integrated circuits (OEICs) are ubiquitous in optical communication, displays, sensing and other related applications. Integrated transmitters [111, 112], photoreceivers [113-115] and phototransceivers [116-119] are commonly used optoelectronic components in these applications. More recently, OEICs are being employed for on-chip transmission of information and in the emerging field of silicon photonics [3, 4]. From consideration of size, cost and ease of operation, it is desirable to form an OEIC in which the component electronic and/or photonic devices are monolithically integrated. For example, an on-chip phototransceiver will consist of a laser monolithically integrated with a low-loss guide and a suitable photodetector. Such a component would be useful for on-chip transmission of information.

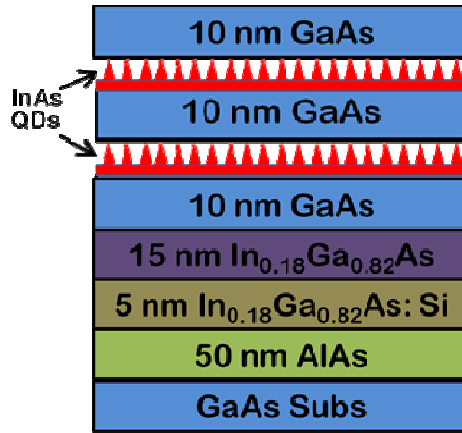
The rolled up microtube laser [42-45, 120] is a light source that can be realized by simple processing steps after epitaxy of the strained heterostructure. Rolled-up microtubes have also been used to form on-chip microfluidic sensors and directional couplers [121-123]. The formation mechanism of the microtube has been discussed in chapter 3. A microtube phototransceiver circuit can be realized by

integrating a microtube laser with a microtube detector with a waveguide. We have demonstrated an OEIC on GaAs, in which a rolled-up microtube laser is monolithically integrated with a passive a-Si/SiO₂ waveguide and a microtube detector fabricated with the same active bilayer, to form a phototransceiver. The microtube laser is photoexcited and the microtube detector is operated in the photoconductive mode. The responsivity of the detector is measured to be 9.8 A/W. The waveguide loss and the responsivity of the phototransceiver are measured to be 7.96 dB/cm and 34 mA/W respectively. It has been demonstrated that such bilayer microtubes formed on GaAs can be transferred on to Si substrates by a controlled substrate-on-substrate transfer process. The OEIC demonstrated here can therefore, in principle, be transferred on to Si CMOS chips.

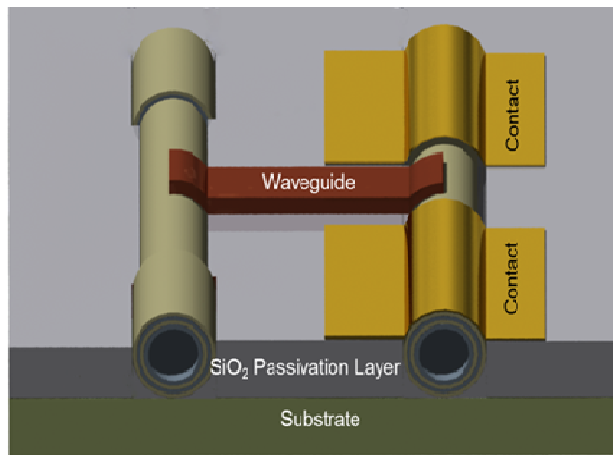
5.2 Device Heterostructure and Fabrication

The quantum dot heterostructure is grown on a semi-insulating (001) GaAs substrate by molecular beam epitaxy (MBE) and is schematically shown in Fig. 5.1(a). A 5 nm Si doped ($n = 3 \times 10^{17} \text{ cm}^{-3}$) In_{0.18}Ga_{0.82}As layer is grown on the AlAs sacrificial layer to form the contact layer of the microtube photoconductive detector. This is followed by 15 nm undoped In_{0.18}Ga_{0.82}As and 30 nm undoped GaAs. Two InAs self-organized quantum dot layers are inserted in the GaAs layer. The areal dot density in each layer, measured by atomic force microscopy (AFM), is $5 \times 10^{10} \text{ cm}^{-2}$.

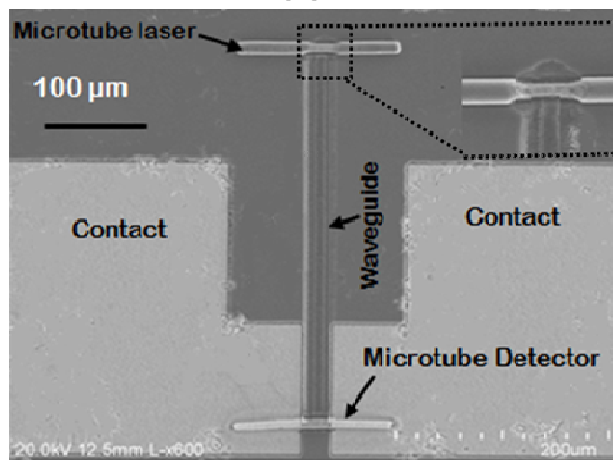
The phototransceiver to be fabricated and characterized is schematically shown in Fig. 5.1(b). To fabricate the free standing microtube laser and detector, two U-shaped mesas facing each other are first defined by selectively etching down to the



(a)



(b)



(c)

Figure 5.1: Schematic of rolled up microtube heterostructure grown by molecular beam epitaxy. Two layers of self-organized InAs quantum dots are contained in the active region; (b) schematic of the monolithically integrated microtube phototransceiver consisting of the laser, photoconductive detector and dielectric waveguide; (c) scanning electron microscope image of the fabricated phototransceiver.

$\text{In}_{0.18}\text{Ga}_{0.82}\text{As}$ layer with a $\text{H}_2\text{O}_2/\text{H}_3\text{PO}_4$ mixture. The terminating edge of the U-shaped body of the microtube to form the laser is corrugated [120] whereas the mesa intended for the detector microtube has no such corrugation. A deep etch through the AlAs sacrificial layer with the same etchant defines the starting edge of rolling. The sample is then immersed in diluted HF solution, which etches AlAs and initiates the rolling process. The two microtubes are formed while rolling towards each other. The diameter of the microtube laser and detector is $\sim 8 \mu\text{m}$ and their separation is $\sim 340 \mu\text{m}$. The airgap between the center part of the microtubes and the substrate is $\sim 0.5 \mu\text{m}$. This gap is critical for control of substrate losses [120]. To facilitate further processing and lithography, the sample is passivated with $4 \mu\text{m}$ SiO_2 by plasma enhanced chemical vapor deposition (PECVD). A a-Si/ SiO_2 dielectric waveguide is

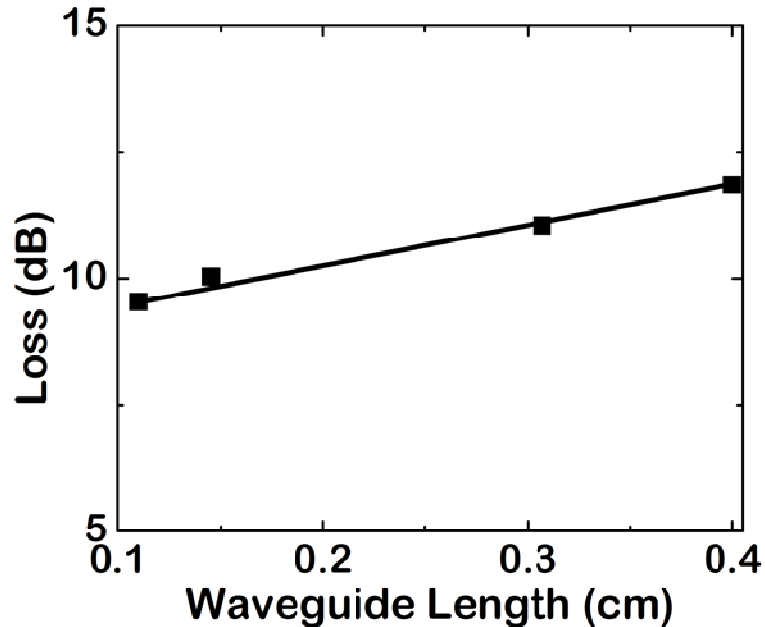


Figure 5.2: Measured transmission loss in the a-Si/ SiO_2 waveguide for different waveguide lengths.

then formed, to laterally connect the laser and the detector microtubes, by sputter deposition of a-Si and dry etching techniques. The thickness of the a-Si guide layer is $0.5\ \mu\text{m}$ and the width of the waveguide is $10\ \mu\text{m}$. Two ohmic contacts to the n-InGaAs layer of the microtube detector are formed by deposition of Ni/Ge/Au/Ti/Au. The separation between the contacts is $25\ \mu\text{m}$. A scanning electron microscope (SEM) image of the completed OEIC, consisting of the integrated microtube laser, waveguide and microtube photoconductive detector, is shown in Fig. 5.1(c). A control OEIC consisting of the microtube laser and detector, without the interconnecting waveguide, was also fabricated. Single waveguides of identical thickness and width were fabricated for the measurement of guide propagation loss. For these measurements guides of varying length were excited at the input end with focused light from a $1.3\ \mu\text{m}$ laser and the transmitted power was measured with a Ge detector. From a plot of guide loss versus transmission length, shown in Fig. 5.2, the propagation loss of the a-Si/SiO₂ waveguide is estimated to be 7.96 dB/cm.

5.3 Experimental Results

The luminescent properties of the quantum dot bilayer heterostructure and the fabricated rolled-up microtube laser in the phototransceiver circuit of Fig. 5.1(c) were first measured. Excitation is provided by a 532 nm diode laser focused to a $\sim 5\ \mu\text{m}$ spot with a suitable objective lens. The luminescence is collected by the same lens, analyzed by a high resolution spectrometer and detected by a liquid nitrogen cooled Ge detector with lock-in amplification. Figure 5.3(a) shows the room-temperature luminescence spectrum obtained from the as-grown bilayer heterostructure and

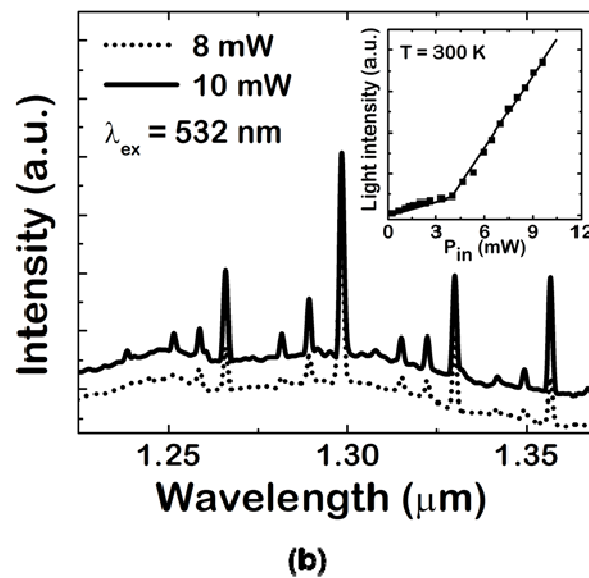
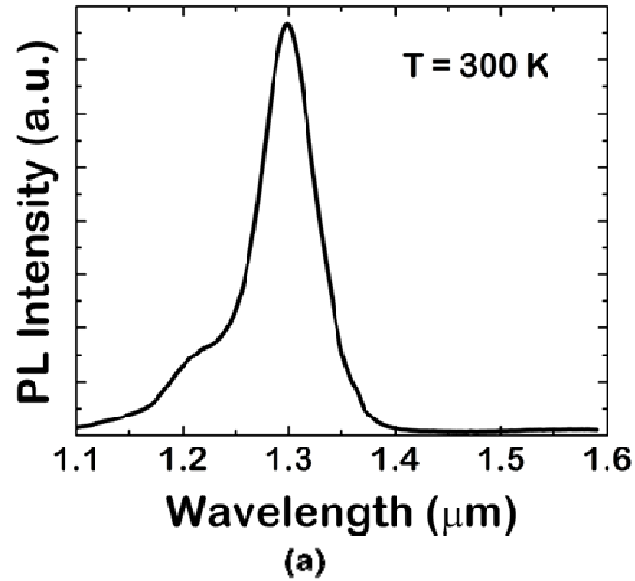
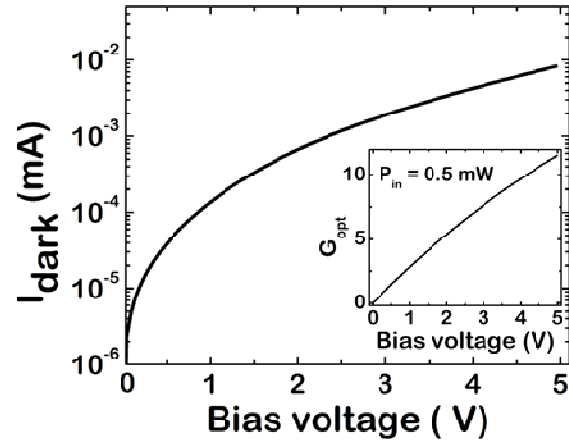


Figure 5.3: (a) Measured room temperature photoluminescence spectrum from the as-grown microtube heterostructure; (b) room temperature microphotoluminescence spectra from the rolled-up microtube laser for two different excitation powers. The inset shows the output light intensity of the microtube laser as a function of excitation power.

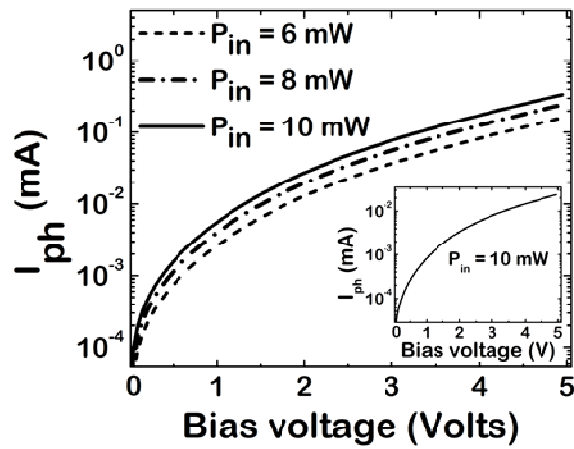
corresponds to emission from the InAs/GaAs quantum dots. The emission peaks at

1.3 μm and has a linewidth (full width at half maximum) of ~ 30 meV. Room-temperature luminescence spectra from the microtube laser for different incident excitation powers are shown in Fig. 5.3(b). The photoexcitation is incident on the microtube in the suspended section. The sharp peaks of higher intensity in the emission spectra are the azimuthal modes which satisfy the phase matching condition of a ring resonator and the threshold condition for lasing in such a laser device. The peaks of smaller intensity in the spectra originate from the axial confinement of modes due to the corrugation that was formed at the outside notch [120]. The laser output (light-light) characteristics for the emission at 1.3 μm is shown in the inset to Fig. 5.3(b).

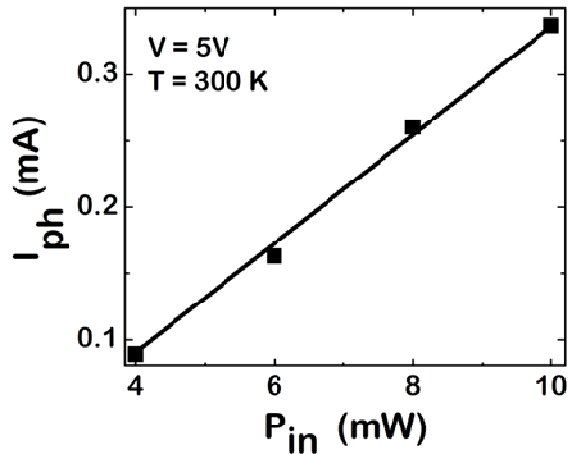
The measured dark current-voltage characteristics of the photoconductive detector is shown in Fig. 5.4(a). The dark current at a bias of 5V is 9 μA , which is quite small. The internal optical gain of a photoconductor is given by $G_{opt} = \frac{h\nu}{q} \left(\frac{I_{ph}}{P_{inc}} \right)$, where I_{ph} is the photocurrent and P_{inc} is the incident photoexcitation power. The gain was measured with 1.3 μm photoexcitation incident on the detector, which is absorbed by the quantum dots, and is plotted in the inset to Fig. 5.4(a) as a function of applied bias. To characterize the complete photoreceiver circuit, 532 nm excitation was made incident on the microtube laser. The incident power was adjusted such that the device was in the lasing mode. The coherent output is coupled via the a-Si/SiO₂ waveguide into the microtube photoconductor, where it is absorbed by the quantum dots and produces a photocurrent. It is important to note that only the coherent emission at $\lambda \approx 1.3$ μm will be transmitted by the waveguide and not the incident 532 nm photoexcitation. The photocurrent-voltage characteristics of the microtube



(a)



(b)



(c)

Figure 5.4: (a) Dark current-voltage characteristics of the microtube detector. Inset shows the photoconductive gain of the microtube detector as a function of bias; (b) variation of photocurrent in the microtube detector as a function of pump power in the microtube laser. Inset shows detector photocurrent due to scattered light in the control OEIC for comparison; (c) variation of photocurrent in the microtube detector for different excitation powers in the microtube laser.

photoconductor for different incident powers on the microtube laser are shown in Fig. 5.4(b). To determine the contribution to the photocurrent by directly scattered light from the excitation laser, the photoexcitation was made incident on the microtube laser in the control OEIC without the a-Si/SiO₂ waveguide. The measured photocurrent-voltage characteristics of the detector with the scattered light is plotted in the inset to Fig. 5.4(b) for comparison. It is evident that the photocurrent generated by the stray light is small in comparison to that due to guided light from the laser. The plot of detector photocurrent at a bias voltage of 5V versus excitation power incident on the laser is depicted in Fig. 5.4(c). From the slope of the plot, the responsivity of the entire phototransceiver is calculated to be 34 mA/W.

5.4 Summary

In conclusion, a GaAs-based rolled-up microtube monolithically integrated phototransceiver is demonstrated. Operation of the OEIC is achieved by photoexcitation of the quantum dot microtube laser, whose output is guided by an a-Si/SiO₂ waveguide to a microtube photoconductive detector realized with the same quantum dot heterostructure.

Chapter VI

High Performance InAs/In_{0.53}Ga_{0.23}Al_{0.24}As/InP Quantum Dot

1.55 μm Tunnel Injection Laser

6.1 Introduction:

The light source that serves as the workhorse in long-haul optical communication links is a 1.55 μm laser, to take advantage of the minimum fiber attenuation in this wavelength range. These long wavelength edge-emitting lasers are generally InP-based and the active (gain) region is lattice-matched In_{0.53}Ga_{0.47}As/InGaAsP/InP or In_{0.53}Ga_{0.47}As/InGaAlAs/In_{0.52}Al_{0.48}As double heterostructure or multi-quantum wells (MQWs) [47-51]. Pseudomorphic or strain-compensated QWs are also used to engineer the gain, confinement energies and associated characteristics [52, 53]. Because of the small bandgap of the gain region injected carriers undergo Auger recombination which, together with gain compression at high injection levels, lead to larger threshold currents, large temperature dependence of the threshold current (small T_0), and large chirp and α -factor associated with small-signal modulation.

GaAs-based quantum dot lasers incorporating multiple self-organized In(Ga)As/GaAs quantum dot (QD) layers have demonstrated superior performance at 1.3 μm [124-130], resulting from the large gain and differential gain in the dots and

more optimized carrier confinement compared to quantum well lasers. The lasers are characterized by $T_o \sim \infty$, extremely low threshold current, large small-signal modulation bandwidth of ~ 15 GHz, and near-zero chirp and α -factor [124-130]. Unfortunately, the emission wavelength of these lasers cannot be extended to $1.55 \mu\text{m}$ without the use of metamorphic buffer layers, which degrade device performance due to the presence of mismatch defects.

There have been reports on InP-based semiconductor lasers that incorporate self-organized InAs quantum dashes as active regions [131-138]. Under group V

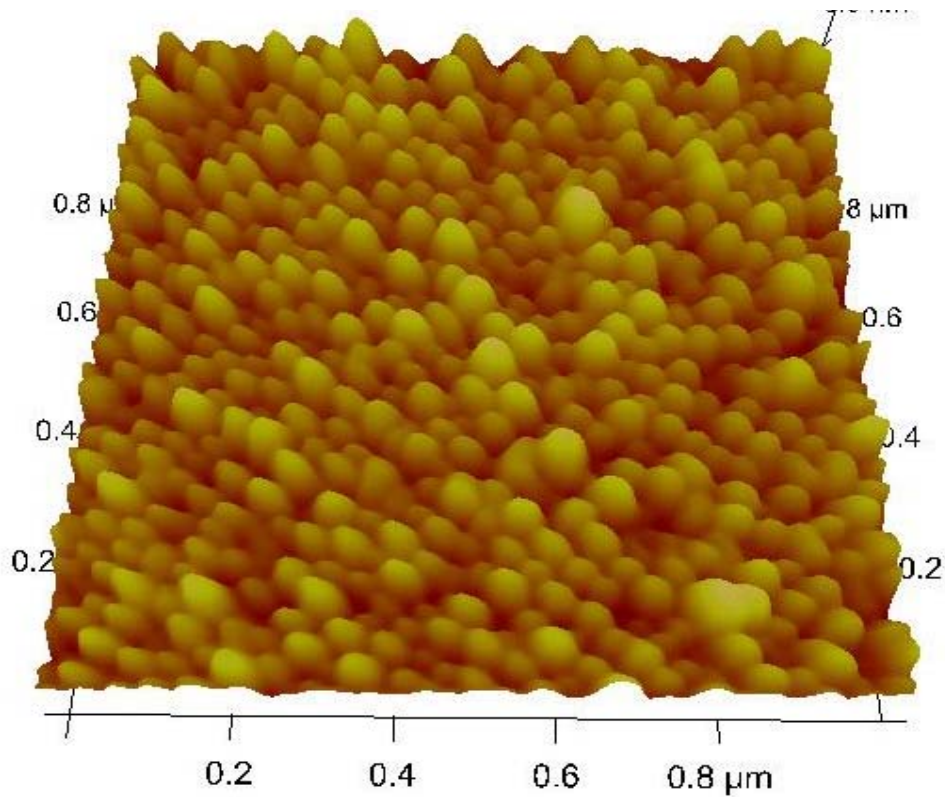
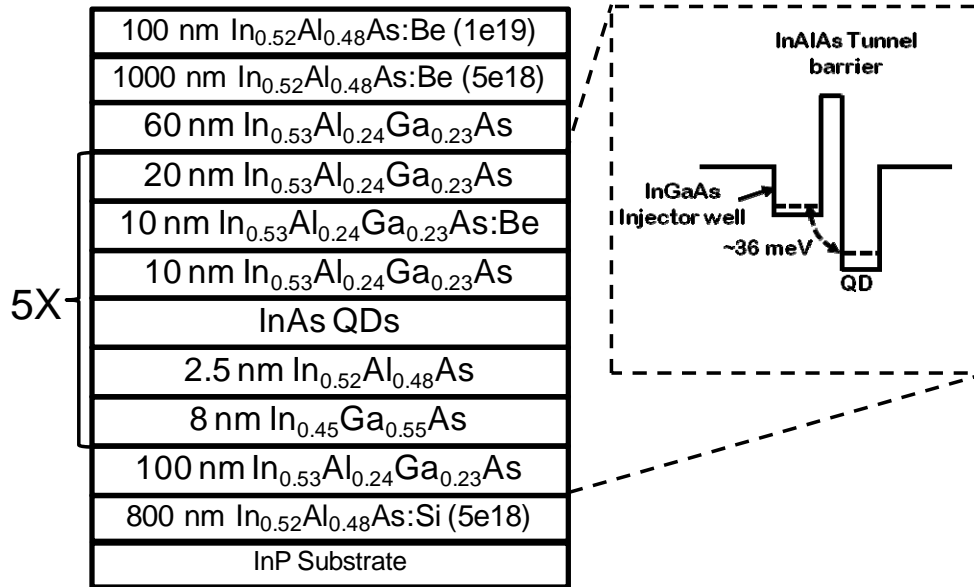


Figure 6.1: Atomic force microscopy (AFM) image of InAs/In_{0.53}Ga_{0.23}Al_{0.24}As/InP quantum dots grown by molecular beam epitaxy. The dot density is estimated to be $5 \times 10^{10} \text{ cm}^{-2}$.

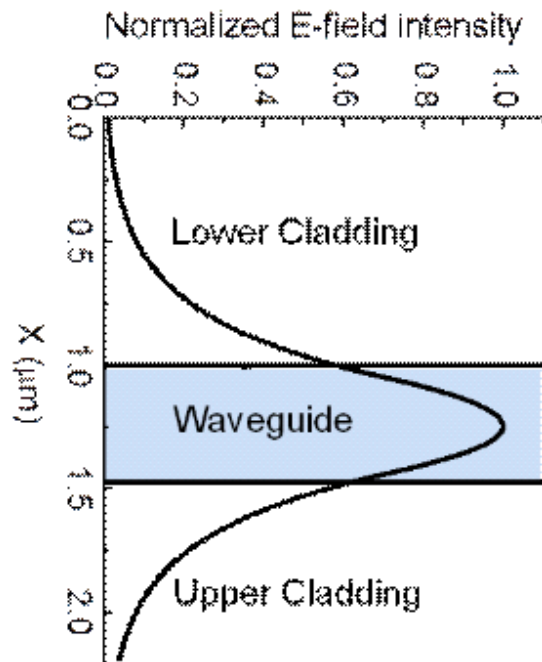
stabilized surface conditions, the quantum dashes are typically elongated along the

$[\bar{1}10]$ direction on (001) InP substrates due to longer indium surface diffusion length along this direction [131, 133]. The emission wavelength of the quantum dashes can be readily tuned in the spectral range of 1.2 to 2.0 μm . Self-organized InAs quantum dashes typically exhibit characteristics similar to InAs/GaAs quantum dots in the transverse direction, and therefore, strong quantum confinement can be achieved. In the longitudinal direction, however, the quantum dashes are more than 100 nm long, which results in very weak quantum confinement. Because of their distinct material and structural properties, InAs quantum dashes exhibit a number of unique characteristics, such as closely spaced electron and hole energy levels and a large Auger recombination rate, which often severely limits the performance of the lasers. Additionally, the achievement of high quality quantum dashes, with small inhomogeneous broadening of the luminescence spectrum, is still elusive due to the complex interplay of thermodynamics and surface kinetics at the growth front of InAlGaAs layers. While many groups have reported the growth and characteristics of quantum dash lasers, failure to address these unique problems, however, generally leads to devices with poor performance at room temperature, such as very large threshold current, highly temperature sensitive operation ($T_o \sim 50\text{-}90$ K) [135, 139-141] large linewidth enhancement factor (≥ 2) [141] and low modulation bandwidth (≤ 7 GHz) [136].

Three-dimensional InAs/InGaAlAs/InP quantum dots have been recently grown by molecular beam epitaxy (MBE) in the Stranski-Krastanow mode using an As_2 source [54]. The luminescence properties of the QDs are extremely good and



(a)



(b)

Figure 6.2: (a) Schematic of the tunnel injection quantum dot laser heterostructure; (b) calculated mode profile.

1.55 μm edge-emitting QD lasers have been reported [55]. However, the fact remains that we are dealing with lasers having small-bandgap materials in the active region and hence Auger recombination and related hot-carrier effects are bound to play a significant role. Tunnel injection of carriers into the active region has been used with great success to minimize hot carrier effects in quantum well and quantum dot lasers [53, 126, 128, 129, 142]. In the most commonly used scheme, cold electrons are directly injected from a wide injector region through a barrier into the ground or first excited state of quantum wells or dots by non-resonant direct or phonon-assisted tunneling [126, 128, 129]. Hot carrier effects resulting from the large two-dimensional density of states in the dot wetting layer and barrier regions and carrier leakage are minimized, resulting in devices with increased differential gain, reduced gain compression, high T_o , and reduced α -parameter and chirp [128, 129]. It is also well-recognized that the hole distribution in quantum dots is thermally broadened into many available states with very small energy spacing and therefore a large injected carrier density would be required for large gain in the ground state. With acceptor (p) doping, extra holes are provided at the ground state energy by either direct doping of the dots or by modulation doping in the barriers [125, 127]. Such doping is also known to reduce hot carrier effects.

In the present study, we have incorporated the electron tunnel injection scheme and modulation doping of the dots with holes in the design of InAs/InGaAlAs/InP QD lasers grown by MBE. Both broad-area and near-single mode ridge waveguide edge-emitting lasers have been fabricated and their static and dynamic characteristics have been measured. The lasers are characterized by large

differential gain ($8 \times 10^{-16} \text{ cm}^2$), relatively low threshold current density (390 A/cm^2), very large T_o (227 K in the range $5 \text{ }^\circ\text{C} \leq T \leq 45 \text{ }^\circ\text{C}$ and 100 K in $45 \text{ }^\circ\text{C} \leq T \leq 75 \text{ }^\circ\text{C}$), large modulation bandwidth (14.4 GHz) and low α - parameter (0.17) and chirp (0.6 \AA), making them extremely attractive for long-haul fiber-optic communication links.

6.2 Epitaxial Growth and Fabrication of QD Lasers

The MBE growth of self-organized InAs/InGaAlAs/InP quantum dots is first described. InAs quantum dots are grown on a $\text{In}_{0.53}\text{Ga}_{0.23}\text{Al}_{0.24}\text{As}$ layer lattice matched to InP substrate by depositing 5 monolayers of InAs at an optimized temperature of $495 \text{ }^\circ\text{C}$ under As_2 flux with a V/III ratio of 18. The growth rate of InAs is kept fixed at 360 nm/hr . An ultra-thin 5 \AA GaAs layer is grown on $\text{In}_{0.53}\text{Ga}_{0.23}\text{Al}_{0.24}\text{As}$ just prior to the growth of quantum dots, which we believe reduces the surface roughness of the $\text{In}_{0.53}\text{Ga}_{0.23}\text{Al}_{0.24}\text{As}$ layer, increases the In adatom mobility on the surface and therefore helps to increase dot density and size uniformity. The areal density of quantum dots measured by atomic force microscopy (AFM) (Fig. 6.1) is $\sim 5 \times 10^{10} \text{ cm}^{-2}$, which is very high for this material system. The average dot diameter is $\sim 25 \text{ nm}$ and height is $\sim 5\text{-}6 \text{ nm}$. Therefore the quantum dots are taller than InAs dots grown on GaAs and the carrier confinement energies are expected to be large.

The band diagram of the tunnel heterostructure and the electronic states in the quantum dot are obtained by solving the Schrödinger equation. The final design is obtained by fine tuning with photoluminescence (PL) measurements on control

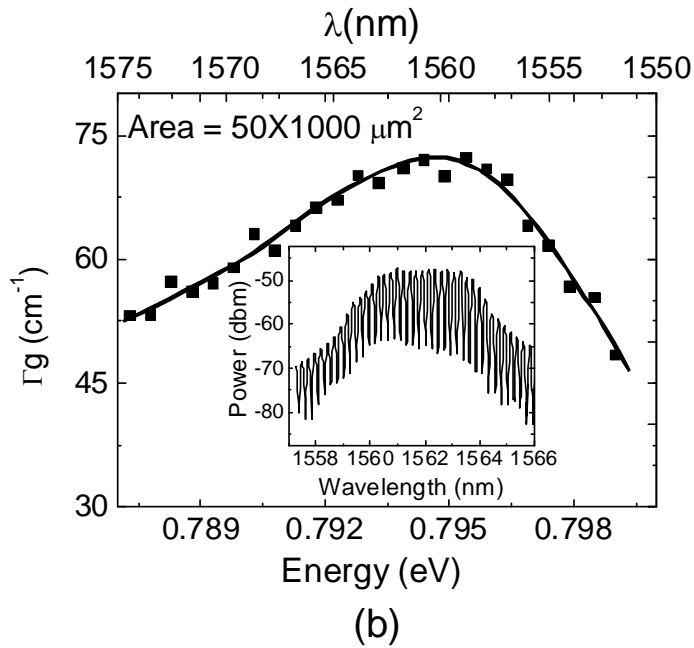
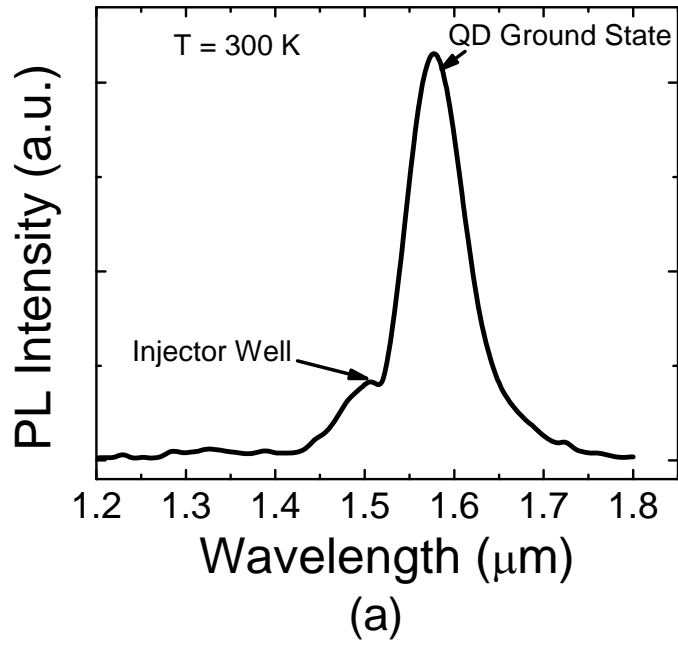


Figure 6.3: Room temperature photoluminescence (PL) spectrum of InAs/In_{0.53}Ga_{0.23}Al_{0.24}As/InP quantum dots; (b) gain spectrum of the quantum dot laser measured from the near-threshold laser spectrum (shown in the inset) using the Hakki-Paoli technique.

samples. The bandgap in the injector well and dot regions necessitate phonon-assisted non-resonant tunneling into the dot ground state. The InAs tunnel injection quantum-dot laser heterostructure, as shown in Fig. 6.2(a), is grown on Si-doped (001)InP substrates. The n- and p-cladding layers consisting of 0.8 μm $\text{In}_{0.52}\text{Al}_{0.48}\text{As}:\text{Si}$ and 1.0 μm $\text{In}_{0.52}\text{Al}_{0.48}\text{As}:\text{Be}$, respectively, are grown at an optimized temperature of 515 $^{\circ}\text{C}$ at a rate of 0.72 $\mu\text{m}/\text{hr}$. The active region consisting of five periods of injector well and dot tunnel injection heterostructures, separated by 40 nm $\text{In}_{0.53}\text{Ga}_{0.23}\text{Al}_{0.24}\text{As}$ barriers, are grown at 495 $^{\circ}\text{C}$. In each period, an 8 nm $\text{In}_{0.45}\text{Ga}_{0.55}\text{As}$ quantum well is grown as the injector region. The injector well and quantum dot layer are separated by a 2.5 nm $\text{In}_{0.52}\text{Al}_{0.48}\text{As}$ tunnel barrier. The PL emissions of both the well and dot layers are carefully tuned so that the ground state of the well is approximately one optical phonon energy (~ 36 meV) above the ground state of the dot layer. The quantum dots are modulation doped p-type with a 10 nm Be-doped ($p = 4.0 \times 10^{11} \text{ cm}^{-2}$) region in the $\text{In}_{0.53}\text{Ga}_{0.23}\text{Al}_{0.24}\text{As}$ barriers. The mode profile in the waveguide was calculated (Fig. 6.2(b)) and a mode confinement factor of $\Gamma = 0.03$ is derived. The room temperature PL spectrum is shown in Fig. 6.3(a), where emission from the injector well and dot layers peak at 1.505 μm and 1.577 μm , respectively, and the full-width-at-half-maximum (FWHM) of the quantum dot emission is ~ 32 meV.

Both broad area (50 μm wide and 390-2000 μm long) and ridge waveguide (2-4 μm wide and 390-2000 μm long) edge emitting lasers were fabricated by standard photolithography and wet etching and contact metallization techniques. The laser facets obtained by cleaving were left uncoated.

6.3. Results and Discussion

6.3.1 Static Characteristics

The modal gain of the QD laser near threshold conditions was measured by the Hakki-Paoli technique [143]. The subthreshold spectra were measured with an optical spectral analyzer under 10 kHz pulsed bias with duty cycle of 1.96% at room temperature. When threshold is reached, the spectral output is characterized by a succession of peaks and valleys. The spectral gain is determined by analyzing these data. The net modal gain Γg , where g is the material gain, is plotted in Fig. 6.3(b) as a function of photon energy for a $50 \mu\text{m} \times 1000 \mu\text{m}$ broad area laser. The measured peak modal gain is 72.5 cm^{-1} , and the modal gain per dot layer is 14.5 cm^{-1} . This is comparable to the highest gain measured in any GaAs- or InP- based quantum dot laser and suggests that we have used the optimum number of QD layers [55] in the active region.

The light-current ($L-I$) characteristics of a broad area laser was measured with pulsed bias (1.96% duty cycle) and is shown in Fig. 6.4(a). A small threshold current density of $J_{th} = 390 \text{ A/cm}^2$ is obtained with as-cleaved facets. The threshold current I_{th} for this device is 195 mA. Even lower values are achievable by coating the facets with dielectric Bragg reflectors. The spectral output of the laser for an injection current of 255 mA is shown in the inset to Fig. 6.4(a) with the peak emission wavelength at $1.56 \mu\text{m}$. The output light-current ($L-I$) characteristics of a $3 \mu\text{m} \times 390 \mu\text{m}$ ridge waveguide device is shown in Fig. 6.4(b).

Temperature dependent measurements were made on the lasers in the range of

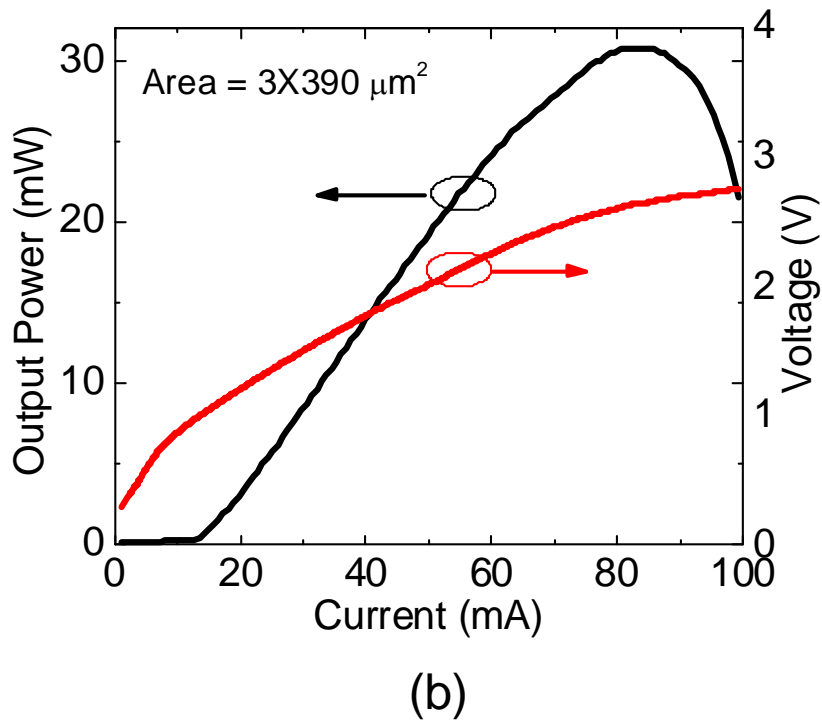
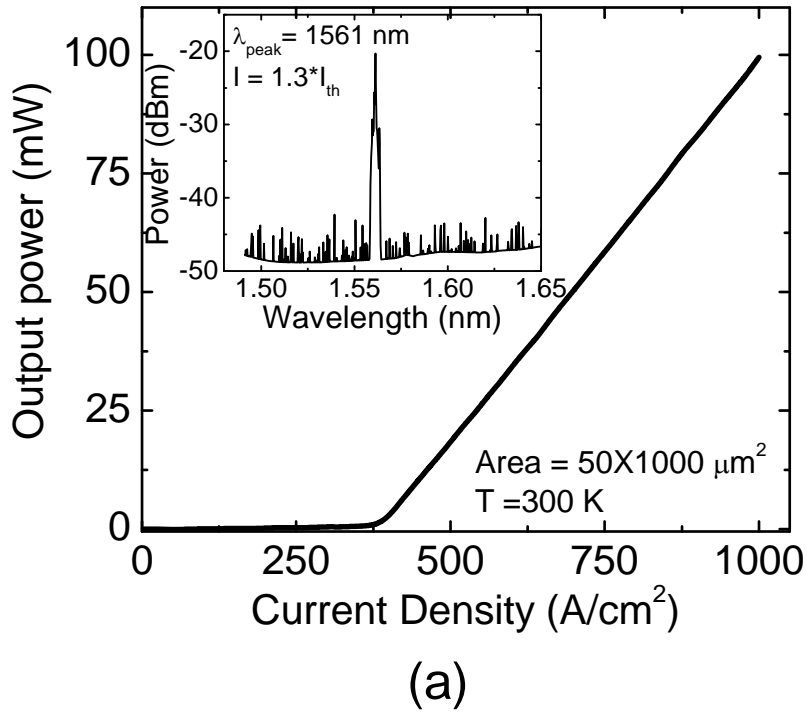
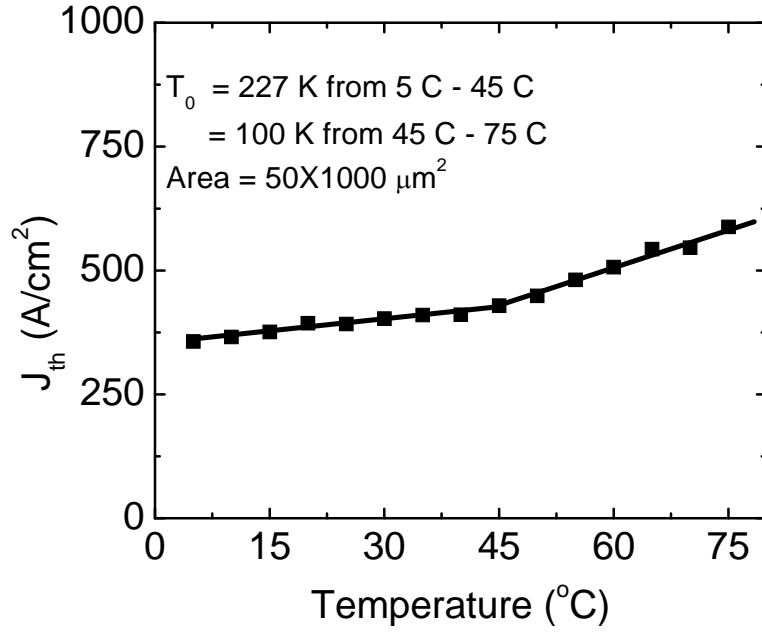


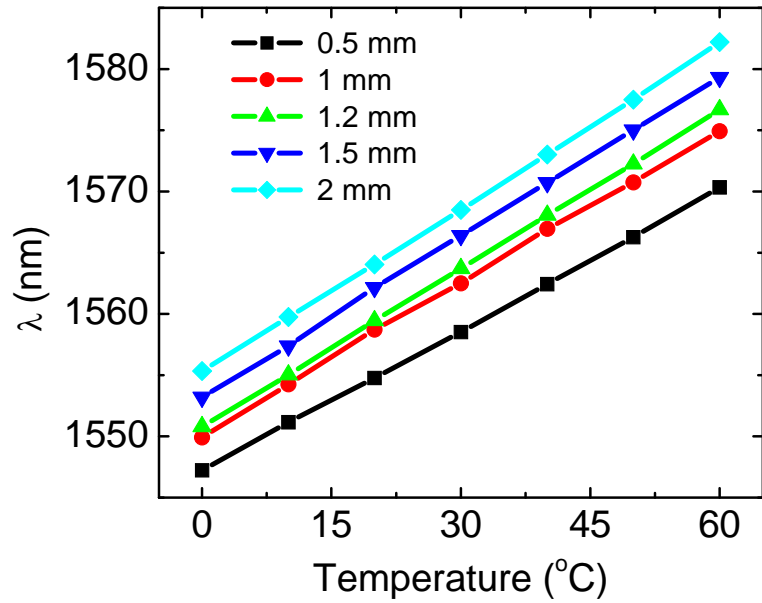
Figure 6.4: (a) Measure light-current characteristics of a broad area quantum dot laser. Inset shows the lasing spectrum at $I = 1.3I_{th}$; (b) L-I-V characteristics of a $3 \mu m \times 390 \mu m$ ridge-waveguide laser showing the roll-over at high injection.

0-75 °C. The variation of threshold current density with temperature for a 1000 μm long broad area laser is shown in Fig. 6.5(a). Analyzing the data with the relation $J_{th}(T) = J_{th}(0) \exp(T/T_0)$ yields values of the temperature coefficient of $T_0 = 227$ K in the range $5^\circ \leq T \leq 45^\circ \text{C}$ and $T_0 = 100$ K in the range of $45^\circ \leq T \leq 75^\circ \text{C}$. These are the highest values of T_0 recorded for any 1.55 μm quantum well or quantum dot laser. We attribute this improvement to the tunnel injection of the cold electrons into the dots and their radiative recombination before they can contribute to Auger recombination and leakage into the barrier regions. The higher conduction band offset in the In(AlGa)As material system is also responsible for the observed improvement. The variation of peak emission wavelength with temperature for lasers with different cavity lengths is shown in Fig. 6.5(a). The temperature and wavelength range represent the practical operational regimes for these lasers. The temperature coefficient $d\lambda/dT$ shows a very small change, from 0.39 nm/K to 0.45 nm/K, in going from 0.5 mm to 2 mm in cavity length. The behavior does not indicate any significant gain saturation or state filling of the ground state [144], as expected from the measured high value of modal gain, and instead reflects the normal bandgap shrinkage with temperature.

We next describe measurements made on lasers with varying lengths, L . The variation of peak emission wavelength is shown in Fig. 6.6(a). As mirror losses increase with decreasing cavity length, the required additional gain can be obtained from transitions involving higher energy levels within the ground state. It may be



(a)



(b)

Figure 6.5: (a) Threshold current density vs. temperature characteristics of the broad-area quantum dot laser; (b) variation of peak wavelength with temperature for broad area lasers of varying cavity lengths.

remembered that the ground state levels are inhomogeneously broadened by coupling between dots of varying size and a two-fold spin degeneracy. Nonetheless, the measured shift of 10.5 nm for a four-fold increase in L is very small, in agreement with the temperature dependent data. Light-current measurements were made on lasers of varying cavity length and the differential quantum efficiency, η_d , and J_{th} were recorded for each length. Figure 6.6(b) shows the variation of η_d^{-1} with L . Assuming mirror reflectivities of 0.30 and the unity injection efficiency, the data yields values of internal quantum efficiency $\eta_i = 65.3\%$ and the cavity loss $\alpha_i = 7.8\text{ cm}^{-1}$. The cavity loss, which includes scattering and absorption losses at the facets, is reasonably low. Figure 6.6(c) shows a plot of J_{th} versus $1/L$. Analysis of this data yields values of the transparency current density $J_{tr} = 272\text{ A/cm}^2$ and differential gain $dg/dn = 7.7 \times 10^{-16}\text{ cm}^2$. In performing this analysis, values of confinement factor $\Gamma = 0.03$, quantum dot fill factor $\zeta = 0.51$, radiative lifetime $\tau_r = 1\text{ ns}$ [145] and the value quoted above for α_i were used.

6.3.2 Dynamic Characteristics

The small-signal modulation characteristics of 390 μm -long ridge waveguide lasers (3 μm ridge width) were measured under pulsed bias conditions with a sweep oscillator, low-noise amplifier, high-speed detector and a spectrum analyzer. The measured response was calibrated for the losses due to cables, connectors, bias network and dc blocking capacitor. The modulation response is shown in Fig. 6.7. A -3dB modulation bandwidth of 14.4 GHz was measured for an injection current of 67 mA, and the resonance frequency f_r at this injection level is 11.2 GHz. This

effectively translates to a digital transmission rate of $\sim 22\text{Gb/s}$ for a bit error rate $< 10^{-11}$ [146]. Since the measured small signal response shows single pole characteristics in the measured range, the response at different injection currents is analyzed by the classical laser modulation response:

$$|M(f)|^2 \propto \frac{1}{(f^2 - f_r^2)^2 + \left(\frac{\gamma_d}{2\pi}\right)^2 f^2} \quad (6.1)$$

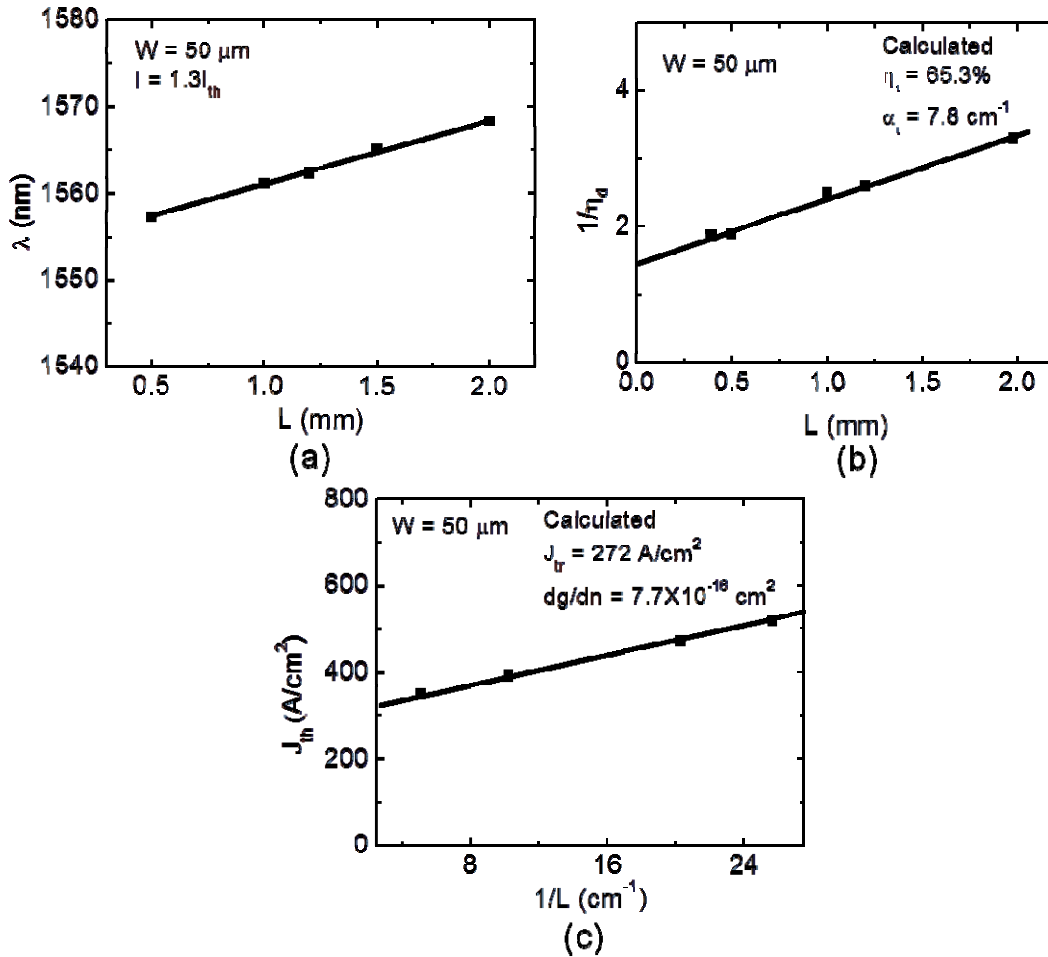


Figure 6.6: (a) Measured variation of peak wavelength of broad area lasers with different cavity lengths; (b) variation of inverse differential slope efficiency with cavity length; (c) variation of threshold current with inverse cavity length.

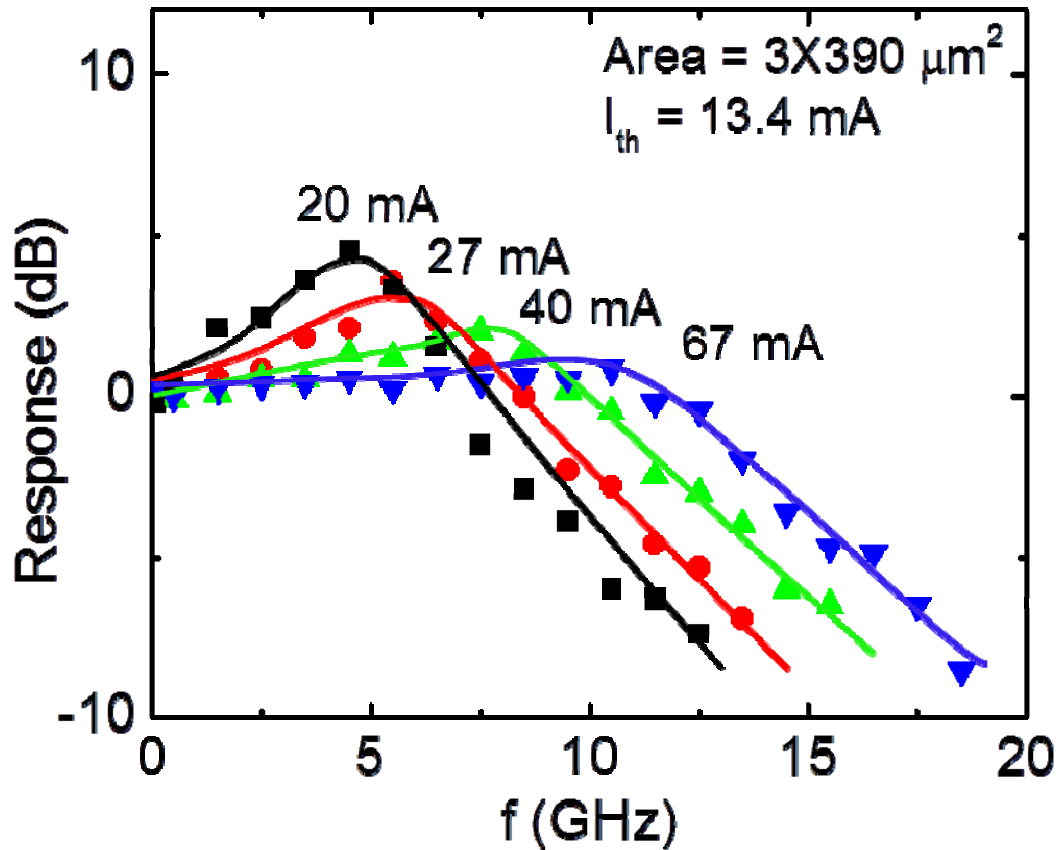


Figure 6.7: Measured small signal modulation response of ridge waveguide tunnel injection quantum dot laser. The solid curves are calculated modulation responses (see text) The -3db modulation bandwidth measured for $I = 67$ mA is 14.4 GHz.

where γ_d is the damping factor. The limitation to the modulation response due to the quantum capture time τ_c , which is related to carrier relaxation in the QD, is neglected and it is assumed that differential gain and gain compression limit the modulation bandwidth. Since we tunnel electrons directly into the QD, this assumption is justified. Under these conditions, the damping factor is related to the resonance frequency by the approximate relationship $\gamma_d \cong Kf_r^2$. The proportionality constant is the K -factor, which is a measure of the damping limited bandwidth. Analysis of the

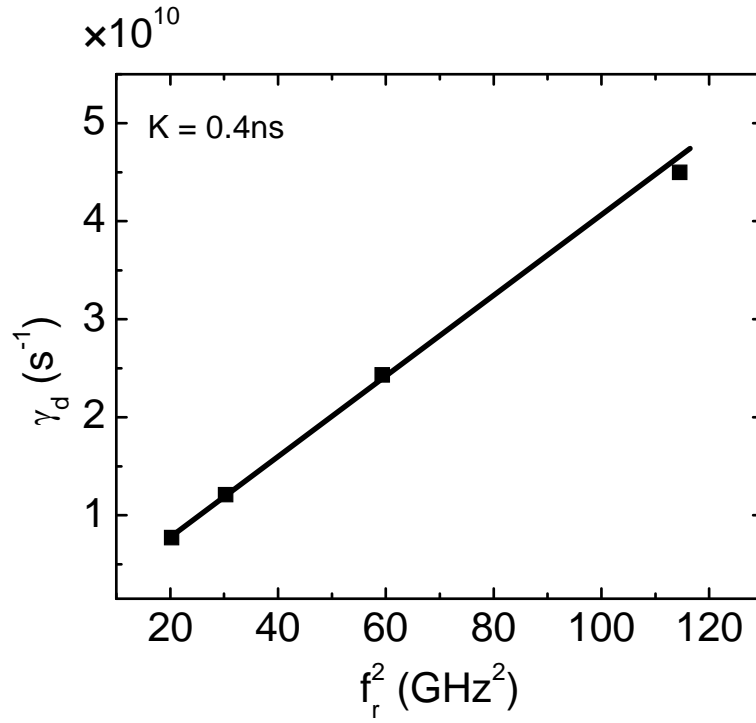
small-signal modulation data of Fig. 6.7 using Eqn (6.1) yields the values of γ_d and f_r and the plot of γ_d versus f_r^2 is shown in Fig. 6.8(a). From the slope of this plot, a value of $K = 0.40$ ns is obtained. The maximum intrinsic modulation bandwidth is given by $f_{-3dB(max)} = 2^{3/2}\pi/K = 22.3$ GHz for these quantum dot lasers. Neglecting carrier transport effects, the K -factor is related to differential gain, gain compression factor ε and photon lifetime τ_p through the equation:

$$K \cong 4\pi^2 \left(\frac{\varepsilon}{v_g \frac{dg}{dn}} + \tau_p \right) \quad (6.2)$$

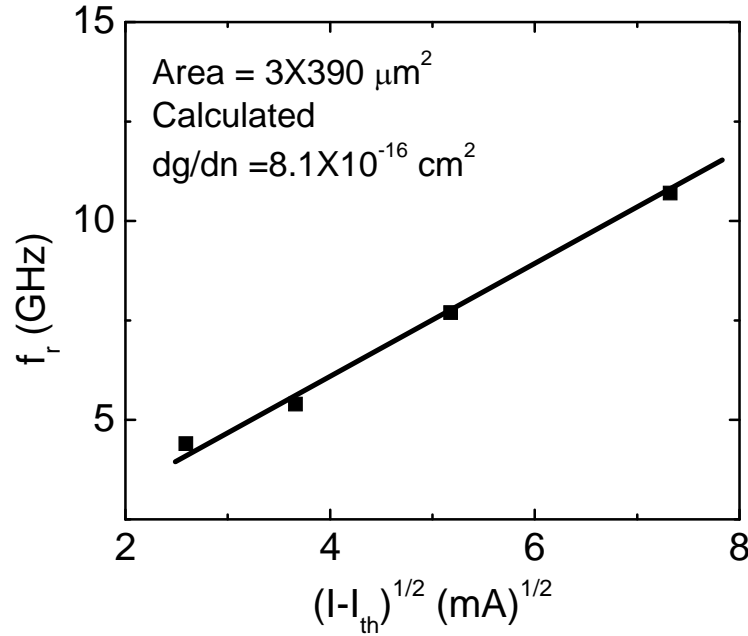
where v_g is the photon group velocity and τ_p is the photon lifetime. The differential gain can also be derived from the small-signal modulation data using the relation:

$$f_r = \frac{1}{2\pi} \left[\frac{v_g \Gamma (I - I_{th}) \frac{dg}{dn} \eta_i}{L w d_{act} q} \right]^{1/2} \quad (6.3)$$

where w is the cavity width and d_{act} is the thickness of the active region. The measured values of f_r is plotted in Fig. 6.8(b) against $(I - I_{th})^{1/2}$ and a value of $dg/dn = 8.1 \times 10^{-16} \text{ cm}^2$ is derived from the slope of this plot. This value of differential gain is in excellent agreement with that derived from the cavity length dependent L - I characteristics (Fig. 6.6(c)). These are amongst the highest values of differential gain measured in $1.55 \mu\text{m}$ quantum well and quantum dot lasers [136]. The value of the gain compression factor is then obtained by the use of Eqn (6.2) as $\varepsilon = 5.42 \times 10^{-17} \text{ cm}^3$. The low value of ε is a direct consequence of p-doping and the tunnel injection mechanism, which minimizes the density of hot carriers due to higher density of states in the QD wetting layer and barrier states than that in the dots.



(a)



(b)

Figure 6.8: (a) Data obtained from analysis of small-signal modulation resonance of QD lasers: (a) variation of damping factor with resonance frequency; (b) variation of resonance frequency with current injection.

One of the consequences of the generation of hot carriers and gain compression in a laser under small-signal modulation is frequency, or wavelength, chirping caused by changes in the refractive index in the gain region. It is therefore of interest to measure this characteristic of the tunnel injection lasers under study. We have measured chirp in the QD lasers during small-signal modulation by measuring the broadening of a single longitudinal mode using an optical spectrum analyzer. The sinusoidal modulation current was superimposed on the pulsed dc bias current above threshold. The envelope of the dynamic shift in the wavelength was recorded and the difference between the half-width of the observed envelope with and without modulation was used to evaluate the chirp. The measurements were done as a function of the frequency of the modulating current. Shown in Fig. 6.9(a) is the measured chirp as a function of the modulation frequency for a peak-to-peak modulation current of 5.5 mA. The chirp is very low, resulting from the large differential gain and small gain compression. An important related parameter is the linewidth enhancement factor, or α -parameter, which is also related to the effects of the change of refractive index with variation of injection current on the dynamic characteristics of the laser. The α -parameter is expressed as: $\alpha = -\frac{4\pi}{\lambda} \left(\frac{dn_r / dn}{dg / dn} \right)$ and

is determined by Hakki- Paoli measurements using the relation:

$$\alpha = \frac{2}{\delta\lambda} \frac{d\lambda_j}{d \left\{ \ln \left[\frac{(\sqrt{r_j} - 1)}{(\sqrt{r_j} + 1)} \right] \right\}} \quad (6.4)$$

where λ_j is the peak wavelength of the j^{th} mode in the near-threshold spectrum, r_j is the peak-to-valley ratio in the spectrum and $\delta\lambda$ is the mode spacing between adjacent

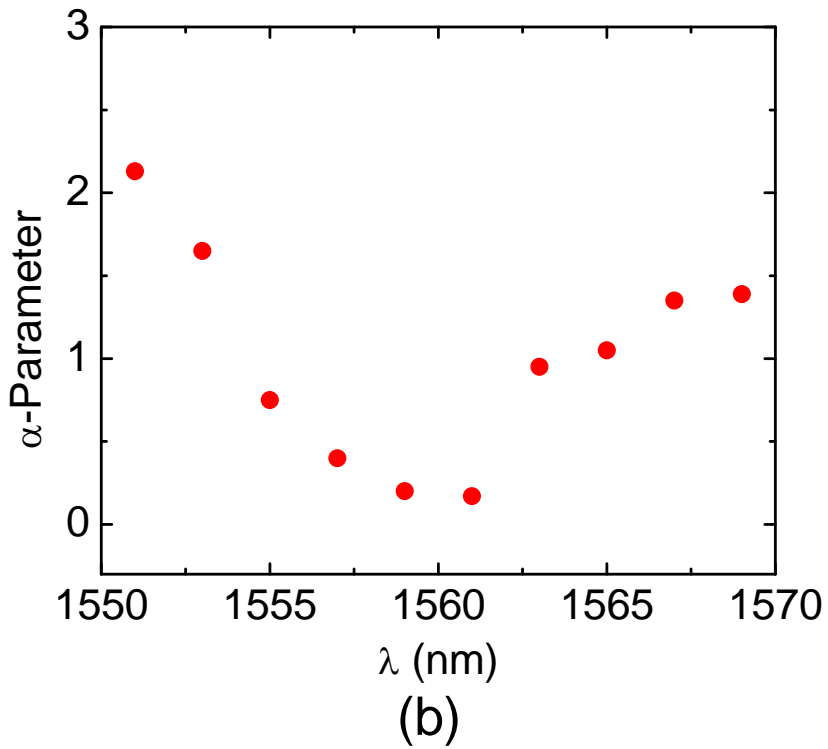
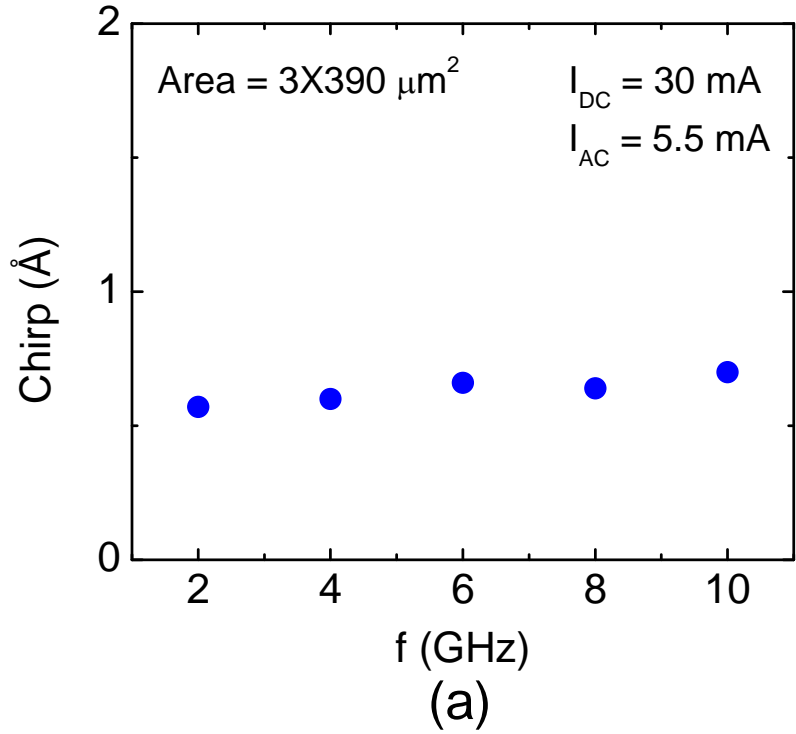


Figure 6.9: Measured chirp of quantum dot laser as a function of small-signal modulation frequency; (b) measured α -parameter as a function of emission wavelength.

modes. The measured α -parameters are plotted against the peak wavelength of the spectrum at threshold in Fig. 6.9(b) and they exhibit a strong wavelength dependence. At and near the peak emission wavelength of $1.56 \mu\text{m}$, $\alpha \sim 0$ and increases to above 1.5 at both shorter and longer wavelengths. It has been shown theoretically that the minimum value of α coincides approximately with the peak gain in quantum dot and quantum wire lasers [147]. A similar trend has also been observed in multi-quantum well and quantum dash lasers [148, 149]. Overall, the extremely low values of chirp and α -factor measured in these p-doped tunnel injection $1.55 \mu\text{m}$ lasers are very favorable characteristics.

6.4 Summary

The growth and application of self-organized InAs quantum dots on InP-based semiconductors is relatively new--- the nanostructures that are formed more easily by self-organization are quantum dashes. However, the characteristics of quantum dash lasers are not suitable for application in optical communication networks due to very high threshold currents and small T_0 . We have therefore made a detailed investigation of self-organized InAs/ $\text{In}_{0.53}\text{Ga}_{0.23}\text{Al}_{0.24}\text{As}/\text{InP}$ quantum dots and QD lasers grown by molecular beam epitaxy. The quantum dots are fairly homogenous in size and have a large aerial density and quantum efficiency. Tunnel injection and p-doping were incorporated in the design of the laser heterostructure to minimize hot-carrier effects. The lasers are characterized by relatively low threshold, very high T_0 , large modulation bandwidth, small chirp and gain compression factor, and near-zero α -parameter. Most of these characteristics result from large gain in the dot layers and

large differential gain. The devices are therefore very attractive for application in long-haul optical communication networks.

Chapter VII

Conclusions and Suggestions for Future Work

7.1 Summary of the Present Work

Due to the superior electronic and optical properties of quantum dots, lasers incorporating quantum dots in the active region are a promising technology in the fields of fiber optic communication and next generation optical interconnects on chips. In this dissertation research, the optical properties of the QDs both on GaAs and InP substrate have been studied and several laser, detector and sensor devices based on these nanostructures have been demonstrated with desirable performance characteristics.

A detailed and systematic growth study has been conducted, as described in chapter 2, in order to optimize the structural and optoelectronic properties of self-organized InAs quantum dots and also to understand the influence of different growth parameters on their properties. Growth of InAs/In_{0.53}Ga_{0.23}Al_{0.24}As quantum dots was achieved on InP substrate at 495 °C under As₂ flux with V/III of 18. Properties of a novel quantum ring, which is derived from in-situ annealing of self-organized quantum dots, has also been investigated and a quantum ring intersubband detector is demonstrated for the 1-3 THz range with a peak responsivity of 25 A/W at 4.2 K.

A rolled-up microtube laser formed by an epitaxial strain-driven mechanism has been demonstrated and discussed in chapter 3. The spectral output has been analyzed and is understood in the framework of mode confinement and scattering in the corrugated

regions at the notches and mode propagation as in a cylindrical ring resonator. Simplified analytical expressions have been derived for the scattering (radiation) loss at the microtube notches, the bending loss and the substrate loss and their values have been calculated as a function of tube diameter. It is seen that the radiation loss is the dominant loss mechanism in these devices. The threshold condition for a microtube laser has been derived from which it is found that the threshold excitation (power) is inversely proportional to the microtube diameter. This result is borne out by the measured data.

A rolled-up microtube directional coupler made of twin microtubes is described in chapter 4. The microtube is made of an InGaAs/GaAs strained bilayer and InAs self-organized quantum dots are inserted in the GaAs layer. The input and coupled microtubes have length and outer diameter ~ 50 and $6 \mu\text{m}$ respectively. The coupling characteristics have been analyzed by the three-dimensional finite difference time domain method. The coupling characteristics have also been measured with isopropyl alcohol, instead of air, as the surrounding media to demonstrate the potential of the device as a sensor

A rolled-up microtube optoelectronic integrated circuit operating as a phototransceiver is described and discussed in chapter 5. The microtube is made of an InGaAs/GaAs strained bilayer with InAs self-organized quantum dots inserted in the GaAs layer. The phototransceiver consists of an optically pumped microtube laser and a microtube photoconductive detector connected by a a-Si/SiO₂ waveguide. The loss in the waveguide and responsivity of the entire phototransceiver circuit are 7.96 dB/cm and 34 mA/W respectively.

The characteristics of $1.55 \mu\text{m}$ InAs self-organized quantum-dot lasers grown on InP (001) substrates, incorporating modulation p-doping of quantum dots and tunnel

injection heterostructure have been discussed and described in chapter 6. The characteristics temperature parameter $T_0 = 227 \text{ K}$ ($5 \text{ }^\circ\text{C}$ – $45 \text{ }^\circ\text{C}$) and 100 K ($45 \text{ }^\circ\text{C}$ – $75 \text{ }^\circ\text{C}$) are measured which is very high compared to quantum well and quantum dot/dash lasers at this wavelength range. The p-doped tunnel injection lasers exhibit a chirp $\sim 0.6 \text{ \AA}$ at 10 GHz , and near zero α -parameter around lasing peak. A maximum 3-dB small signal modulation bandwidth of 14.4 GHz is achieved at 278 K and maximum intrinsic modulation bandwidth of 22.3 GHz has been calculated from the K-factor. The differential gain and gain compression factor of the quantum dot lasers, calculated from the small signal response are $\sim 8.1 \times 10^{-16} \text{ cm}^2$, and $5.42 \times 10^{-17} \text{ cm}^3$ respectively.

7.2 Suggestions for the Future Work

Despite the achievements we have made, challenges exist for those lasers if they are to fulfill their potential as low-cost, portable, high-speed lasers in the field of on-chip or long distance fiber optic communication. For the rolled-up microtube, the primary challenge is electrical injection of carriers. Therefore, future work should focus on electrical injection while maintaining the properties of the microtube laser intact. In the case of the $1.55 \text{ }\mu\text{m}$ quantum dot laser, the main goal of the future work should be on increasing the modulation bandwidth of the laser to compete with state of the art quantum well lasers. Several approaches towards these goals are thus suggested in this chapter.

7.2.2 Electrically Injected Rolled-up Microtube Laser

Optically excited quantum dot rolled-up microtube lasers have been demonstrated by several groups in recent years [39-45, 120]. However, electrically injected rolled-up

devices have not been demonstrated yet. The problem is mainly due to very thin epitaxial layer through which carriers need to be injected which is essentially a fabrication problem.

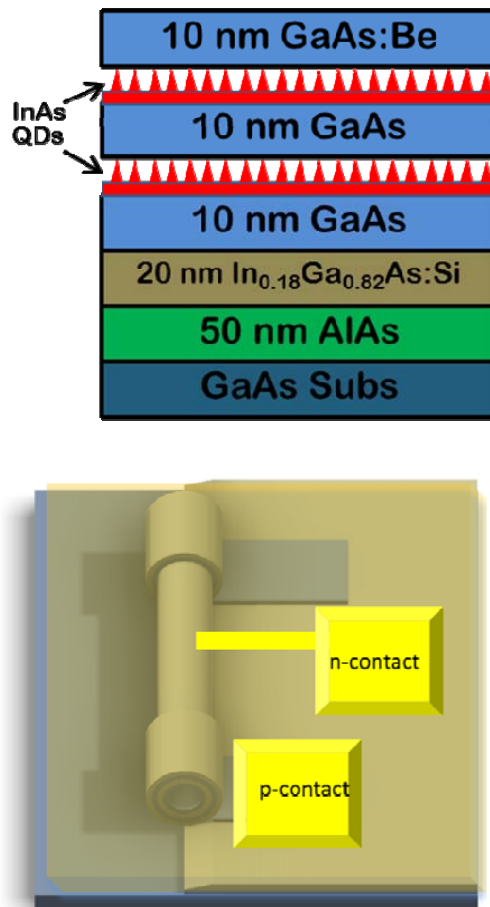


Figure 7.1: (a) Schematic heterostructure of the electrically injected microtube laser; (b) Schematic of the fabrication mechanism.

For electrical injection of carriers, two contact layers (n-type and p-type) need to be grown in the ultrathin device heterostructure. The device heterostructure is shown in Figure 7.1(a). In the proposed heterostructure, the quantum dot active region will be sandwiched between n-type and p-type contact region. Due to diffusion of dopants,

especially Beryllium, the luminescence efficiency of the quantum dot degrades. Therefore growth condition of the epitaxial layers needs to be optimized to reduce the diffusion of the dopants into the active region. The fabrication scheme for the electrically injected microtube lasers is shown in Fig. 7.1(b). A thin p-contact layer will be deposited on the U-shaped mesa which will eventually roll with the tube. Then the rolled up devices will be passivated with a thick layer of SiO₂ to allow further lithography. Finally a thin n-contact layer will be deposited on the tube.

7.2.2 Investigation of Gain-Lever Effect in InAs/In_{0.53}Ga_{0.23}Al_{0.24}As/InP Quantum Dot Laser

The motivation to use quantum dots in the active region of semiconductor lasers is to achieve better temperature stability and large modulation bandwidth. As discussed in chapter 6, with p-doped quantum dot tunnel injection heterostructure, a 3-dB small signal modulation bandwidth of 14.4 GHz was achieved with record $T_0 = 227$ K and 100K for the temperature range of 5 °C.- 45 °C and 45 °C -75 °C respectively. However, 3-dB modulation bandwidth and T_0 are still smaller than those of InAs/GaAs quantum dot lasers. This is mainly due to nonuniformity in the quantum dots and their non ideal shape, bigger size and somewhat connected dot morphology. The uniformity in the dot layer could possibly be achieved by further optimization of growth parameters. Further gain-lever effect is realized by a two-section device as shown in Fig. 7.2 can also be investigated to increase modulation bandwidth of of the laser. Using asymmetric current injection, the short section, which is referred acts as the modulation section is DC-biased at a lower gain level than the larger section termed the gain section. This scheme provides

a high differential gain under small-signal RF modulation as shown in Fig. 7.2. The longer gain section is only DC-biased and supplies most of the amplification but at a relatively smaller differential gain. Due to gain clamping at threshold and the nonlinear

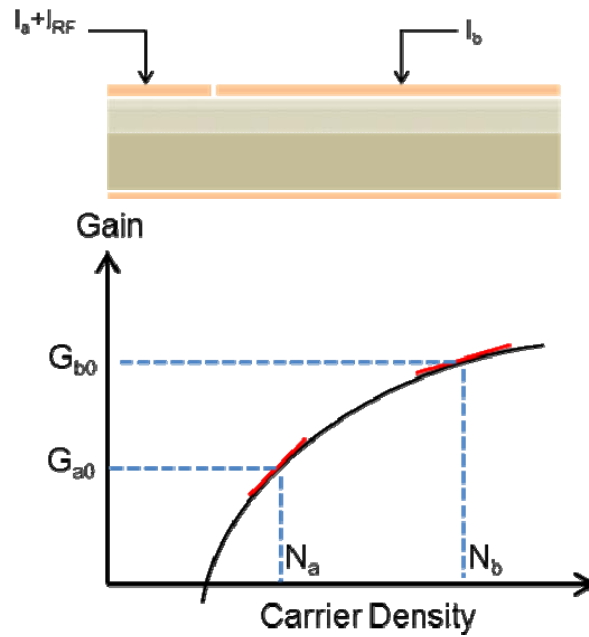


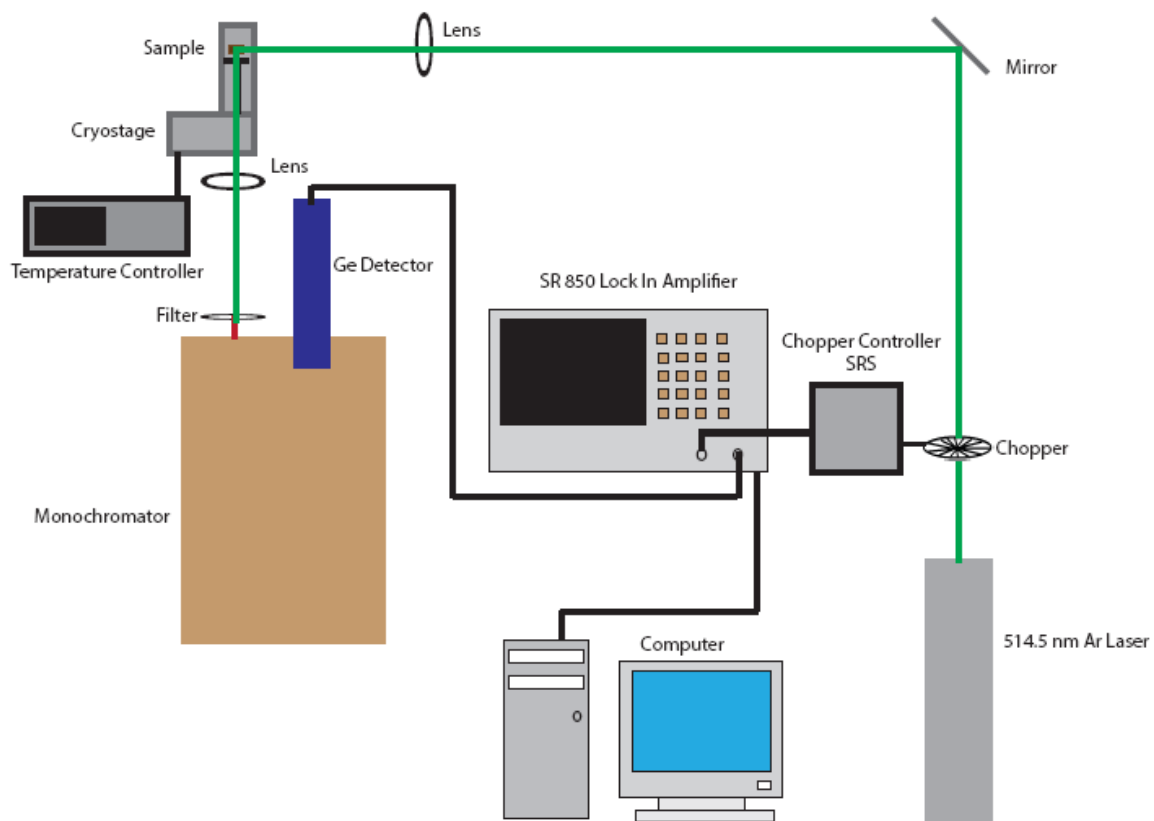
Figure 7.2: Schematic of the multisection laser device for gain lever operation.

dependence of gain with carrier density, small changes in carrier density in the short section produce a drastically larger variation in carrier density in longer section to maintain the threshold gain condition. The outcome is that the modulation efficiency and larger 3-dB bandwidth. The effects of different cavity length for longer and shorter section could also be investigated.

APPENDICES

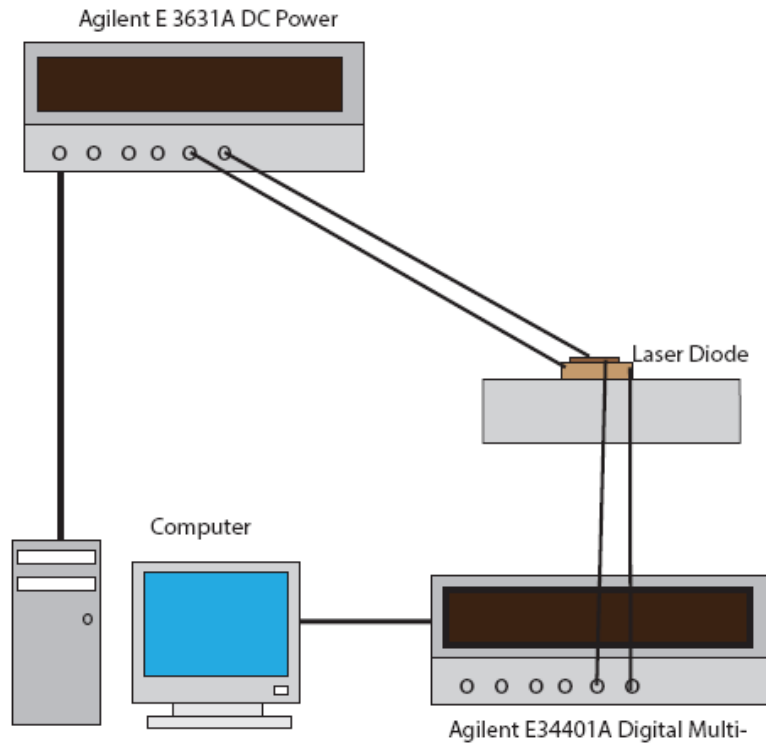
A. Measurement Setups

A1. Photoluminescence Measurement Setup



The sample is excited with a 514.5 nm Ar laser. The laser beam is chopped at 400 Hz and the emission from the sample is guided into the monochromator with proper optics. The signal detected by a liquid nitrogen cooled Ge detector and acquired via lock-in technique. For low temperature measurement the sample is put in a closed loop He cryostat.

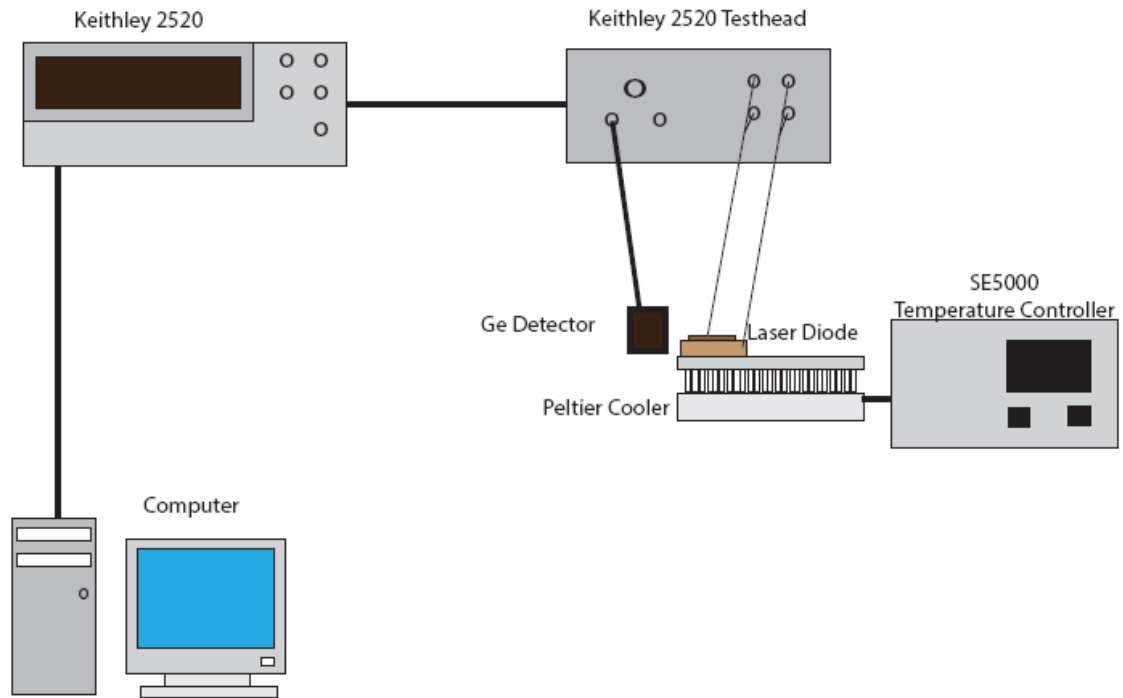
A2. Laser Current-Voltage Characteristics Measurement Setup



The I-V characteristics can be measured in both CW and pulsed mode. The laser diode is biased with a computer controlled dc power supply. The ideality factor of the laser diode can be calculated as:

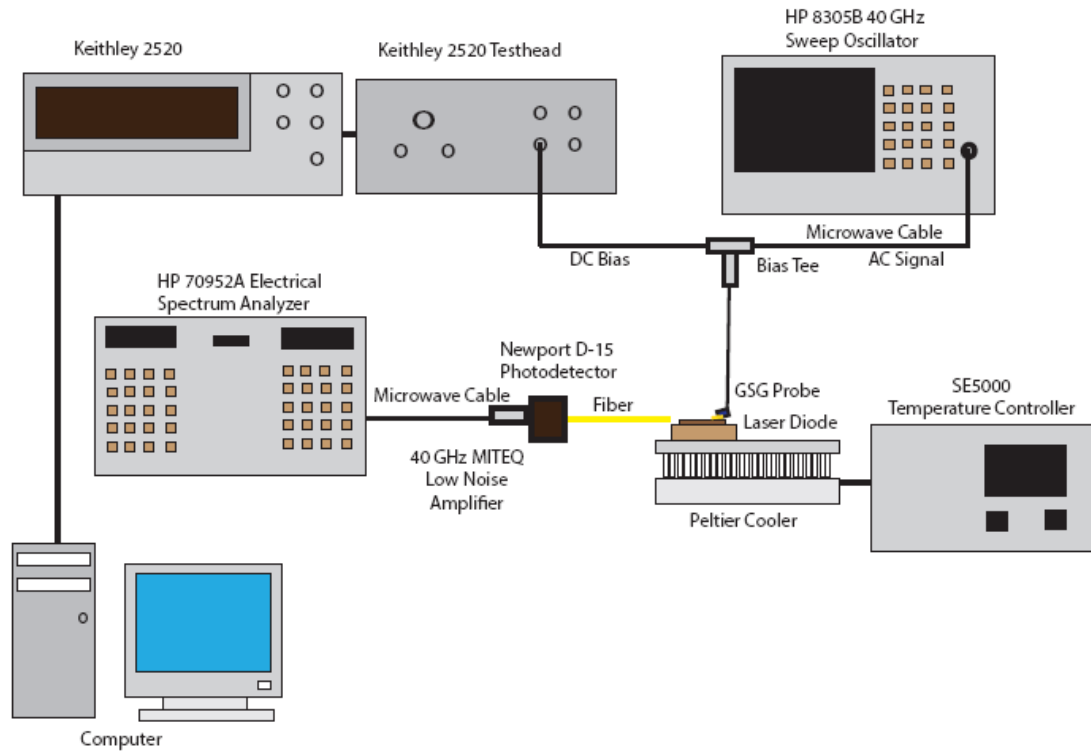
$$n = \frac{kT}{q} \frac{\partial V}{\partial \ln(I)}$$

A3. Laser L-I Measurement Setup



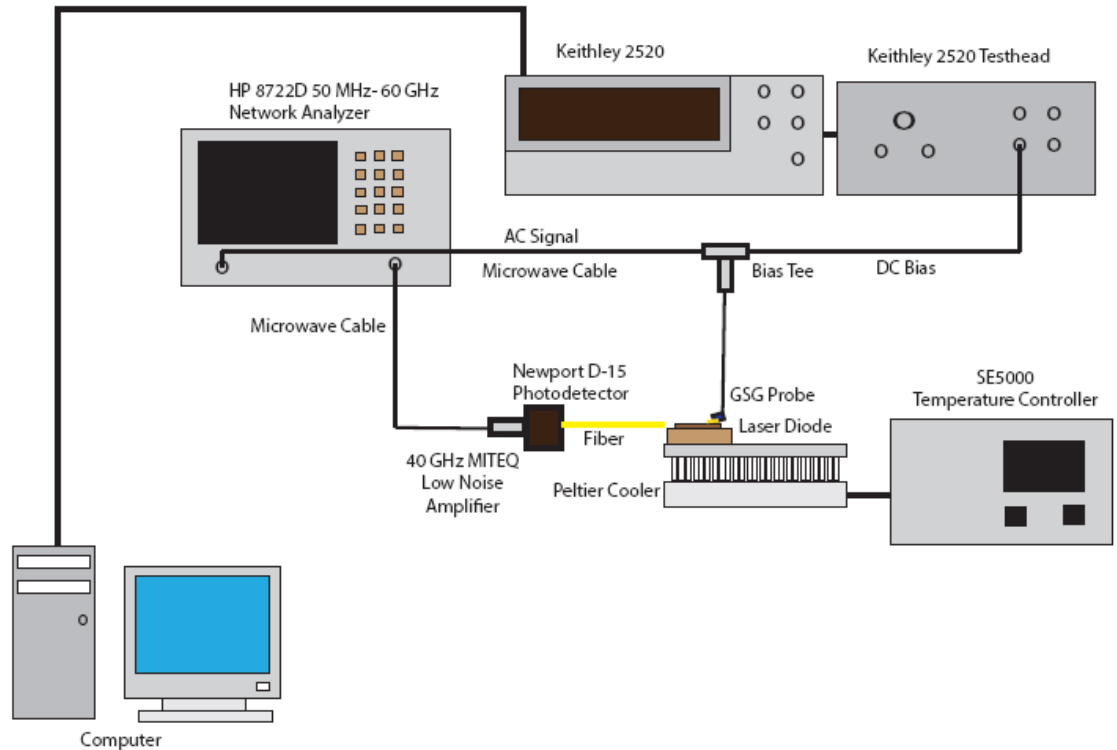
The laser diode is mounted on a Peltier cooler and is biased with a computer controlled dc power supply. Light from the laser diode is collected by an integrated sphere and detected by Ge detector. The laser diode can be biased in both CW and pulsed mode of operation. This measurement setup can be used for temperature dependent threshold measurement to find out T_0 of the laser.

A4. Small Signal Modulation Measurement: Scheme 1



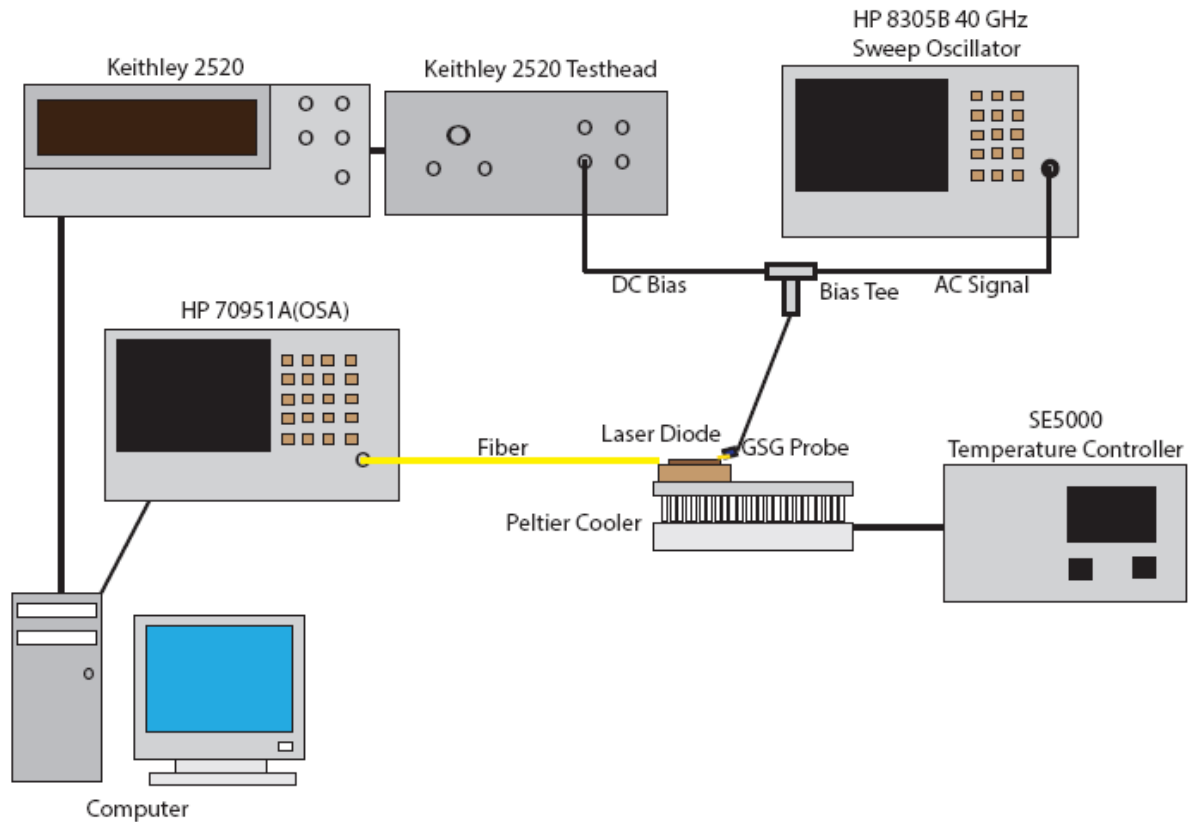
The laser diode is mounted on the Peltier cooler and is biased with a high frequency ac signal on top of a dc bias via a GSG probe. The light output is coupled to a fiber and guided to a high speed detector. The detector output is amplified by a small signal amplifier and is then fed to electrical spectrum analyzer. This measurement setup is used for measuring 3-db bandwidth, K-factor and damping factor γ_d .

A5. Small Signal Modulation Measurement: Scheme 2



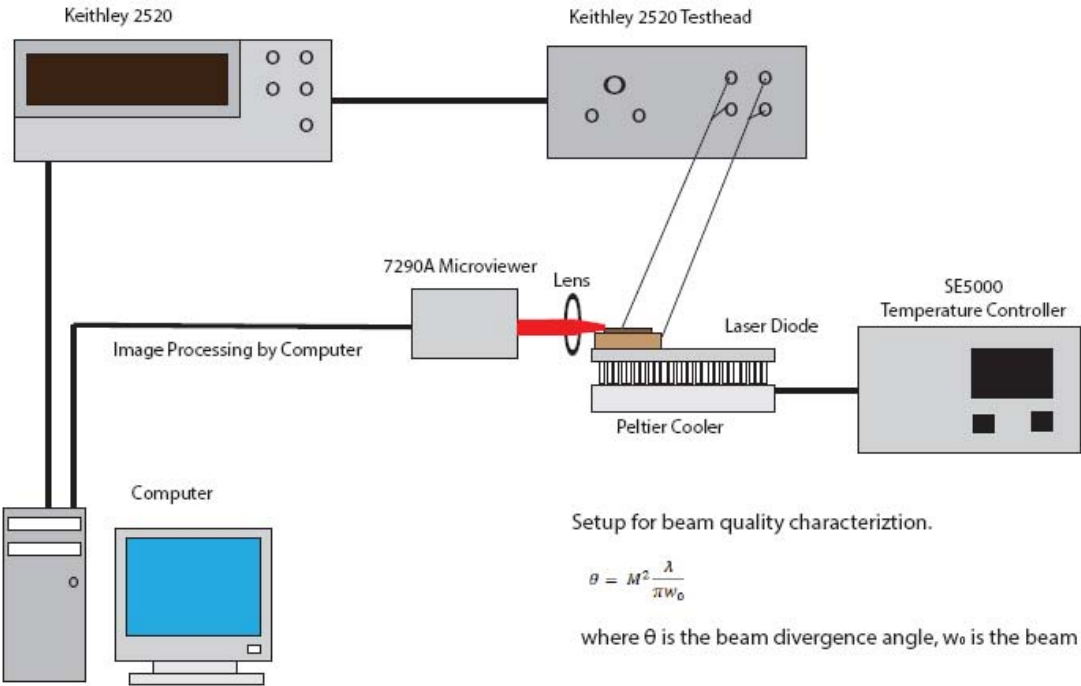
The laser diode is mounted on the Peltier cooler and is biased with a high frequency ac signal on top of a dc bias via a GSG probe. The light output is coupled to a fiber and guided to a high speed detector. The detector output is amplified by a small signal amplifier and is then fed to an electrical network analyzer. This measurement setup is used for measuring 3-db bandwidth, K-factor and damping factor γ_d .

A6. Laser Spectrum, Gain and Chirp Measurement Setup



The laser diode is mounted on the Peltier cooler and is biased with DC power supply. The light output is coupled to a fiber and guided to optical spectrum analyzer. The light spectrum is then captured on the computer. This setup can be used for obtaining lasing spectrum. This can also be used for acquiring sub-threshold spectrum which is used for calculating modal gain. Chirp can be measured using this setup by biasing the laser diode with an ac signal on of dc bias.

A7. Far Field Measurement Setup



B. Quantum Dot Ridge Waveguide Laser Processing

1. Quantum Dot Laser MBE Growth

1.1 Oxide dissolve at 525 °C

1.2 $\text{In}_{0.52}\text{Al}_{0.48}\text{As}$ n-and p-cladding are grown at 515 °C at a growth rate of 2 Å/sec.

1.3 InAs quantum dots and $\text{In}_{0.53}\text{Ga}_{0.23}\text{Al}_{0.24}\text{As}$ waveguide layers are grown at 495°C.

2. Back Surface Indium removal

2.1 Lapping:

Backside planarization using 9 μm alumina grit

2.2 Solvent clean:

Xylenes (hot solution ready): >30 min 105 °C hotplate

Acetone: 10 min, warm

IPA: 10 min

DI Water Rinse: 2 min

3. Alignment Mark Deposition

3.1 Solvent clean:

Acetone: 10 min on hot plate

IPA 10 min

DI water Rinse: 2 min

3.2 Lithography

Dehydrate bake: 2 min, 115 °C hotplate

Resist coating: HMDS, SPR 220-3.0 @ 4.0 krpm, 30 sec

Pre-bake: 90 sec @ 115 °C on hotplate

Exposure: 0.34 sec in projection stepper

Post-bake: 90 sec @ 115 °C

Resist development: AZ 300 MIF 55 sec;

DI water rinse 3 min

3.3 Descum:

30 sec, 80 W, 250mT, 17% O₂

3.4 Metal Deposition

Ti/Au 100 Å /300 Å

3.5 Metal Lift-off

2 hours in Acetone

4. Defining p-Mesa

4.1 Solvent clean:

Acetone: 10 min on hot plate

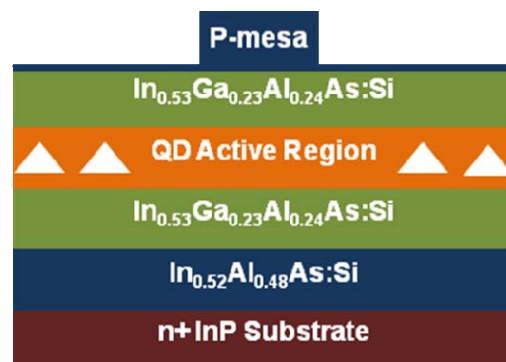
IPA 10 min

DI water Rinse: 2 min

4.2 Lithography

Dehydrate bake: 2 min, 115 °C hotplate

Resist coating: HMDS, SPR 220-3.0 @ 4.0 krpm, 30 sec



Pre-bake: 90 sec @ 115 °C on hotplate

Exposure: 0.34 sec in projection stepper

Post-bake: 90 sec @ 115 °C

Resist development: AZ 300 MIF 55 sec;

DI water rinse 3 min

4.3 Plasma Etching

LAM:

Cl₂ : BCl₃ : Ar = 18 : 12 : 40 sccm, 5mT, 300 W, (rate ~ 360 nm/min)

4.4 Resist Removal

Plasma Asisher: 300 sec, 250 W, O₂ ~17%

Acetone: 10 min on hot plate

IPA: 5 min

DI water rinse: 2 min

4.5 Dektak: measure mesa height

5. Defining n-Mesa

5.1 Solvent clean:

Acetone: 10 min on hot plate

IPA 10 min

DI water Rinse: 2 min

5.2 Lithography

Dehydrate bake: 2 min, 115 °C hotplate

Resist coating: HMDS, SPR 220-3.0 @ 4.0 krpm, 30 sec



Pre-bake: 90 sec @ 115 °C on hotplate

Exposure: 0.34 sec in projection stepper

Post-bake: 90 sec @ 115 °C

Resist development: AZ 300 MIF 55 sec;

DI water rinse 3 min

5.3 Plasma Etching

LAM:

Cl₂ : BCl₃ : Ar = 18 : 12 : 40 sccm, 5mT, 300 W, (rate ~ 360 nm/min)

5.4 Resist Removal

Plasma Asihar: 300 sec, 250 W, O₂ ~17%

Acetone: 10 min on hot plate

IPA: 5 min

DI water rinse: 2 min

5.5 Dektak: measure mesa height

6. n-metal Deposition

6.1 Lithography

Dehydrate bake: 2 min, 115 °C

hotplate

Resist coating: HMDS, SPR

220-3.0 @ 4.0 krpm, 30 sec

Pre-bake: 90 sec @ 115 °C on hotplate

Exposure: 0.34 sec in projection stepper



Post-bake: 90 sec @ 115 °C

Resist development: AZ 300 MIF 55 sec;

DI water rinse 3 min

6.2 Descum:

30 sec, 80 W, 250mT, 17% O₂

6.3 Oxide removal

HCl : DI water = 1:1, 1 min to remove native oxide

DI water rinse: 3 min

6.4 Metal deposition

Ni/Ge/Au/Ti/Au = 250 Å/325 Å/650 Å /200 Å /3000 Å

6.5 Lift-off

Overnight in Acetone

IPA: 10 min

DI water: 2 min

7. Passivation

SiO_x deposition: 1000 nm using

GSI PECVD



8. Oxide Etch (Formation of Via holes)

8.1 Lithography

Dehydrate bake: 2 min, 115 °C hotplate

Resist coating: HMDS, SPR 220-3.0 @ 4.0 krpm, 30 sec

Pre-bake: 90 sec @ 115 °C on hotplate

Exposure: 0.34 sec in projection stepper

Post-bake: 90 sec @ 115 °C

Resist development: AZ

300 MIF 55 sec;

DI water rinse 3 min

8.2 Plasma Etch

LAM:

SF₆ : C₄F₈ : Ar = 8 : 50 :

50 sccm, 10 mT, 300 W (rate ~ 175 nm/min)



8.3 Resist Removal

Plasma Asisher: 300 sec, 250 W, O₂ ~17%

Acetone: 10 min on hot plate

IPA: 5 min

DI water rinse: 2 min

9. p-metal and Interconnect Deposition

9.1 Lithography

Dehydrate bake: 2 min, 115 °C hotplate

Resist coating: HMDS, SPR 220-3.0 @ 4.0 krpm, 30 sec

Pre-bake: 90 sec @ 115 °C on hotplate

Exposure: 0.34 sec in projection stepper

Post-bake: 90 sec @ 115 °C

Resist development: AZ 300 MIF 55 sec;

DI water rinse 3 min

9.2 Descum:

30 sec, 80 W, 250mT, 17% O₂

9.3 Oxide removal

HCl : DI water = 1:1, 1 min to remove native oxide

DI water rinse: 3 min

9.4 Metal deposition

Ti/Pt/Au

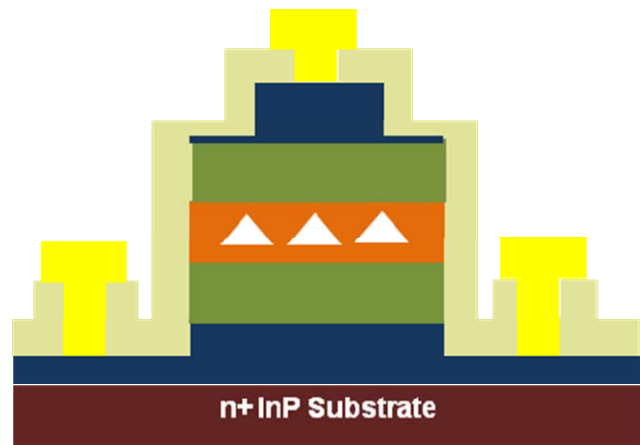
= 200 Å/200 Å/3000 Å

9.5 Lift-off

Overnight in Acetone

IPA: 10 min

DI water: 2 min



10. Annealing

10.1 Rapid thermal annealing: 360 °C, 2 min in N₂ environment

11. Lapping

11.1 Mounting the sample on a glass plate with Paraffin wax (135 °C)

11.2 Lap down sample to ~ 100 μm

11.3 Solvent clean:

Xylenes > 30 min @ 105 °C hotplate

Acetone: 10 min

IPA : 10 min

DI water rinse: 2 min

12. Cleaving

12.1 Scribing: Make 2000 μm long, 400~1200 μm wide, 100 μm deep scribe

12.2 Press the sample gently with a small roller.

C. MATLAB Code for Waveguide Modes and Confinement Factor Calculation

```
clear all;
close all;
clc;
f=0.100;
c=0.005;

n1=3.23; %InAlAs cladding
n2=3.5; %InAlGaAs
n3=3.55; %InGaAs
n4=3.71; %InAs dot

n=[n1 n2 n3 n1 n4 n2 n3 n1 n4 n2 n3 n1 n4 n2 n3 n1 n4 n2 n3
n1 n4 n2 n2 n1]; %Enter index for each layer in here
including outer cladding (probably air)
e=n.^2; %calculates permittivity assuming nonmagnetic
u= ones(1,length(n)) ; %can change permeability if
applicable, otherwise fill with the same number of 1's as
the n vector
active=[0 0 0 0 1 0 0 0 1 0 0 0 1 0 0 0 1 0 0 0 1 0 0 0]; %
mark active layers with "1", others with "0"

confines=0;
i=0;
lengths=0;
for d=0.020:0.002:0.02;
    i=i+1;
    lengths(i)=d;
h=[.1 .008 .0025 .005 .030 .008 .0025 .005 .030 .008 .0025
.005 .030 .008 .0025 .005 .030 .008 .0025 .005 .030 .060];
%height of every layer except outer layers (assumed
infinite)
w=1.56; %wavelength in um

figure(1); %to plot the b11 as a function of kz

minz=waveguide(e, u, h, w); %calculates kz which confine
mode

figure(2);
hold on;
```

```

for j=1:length(minz)
    confines(i)=Eplotter_Mod( sqrt(e.*u), h, minz(j), w,
active);
end

hold off;

```

Solve waveguide

```

function [ minz ] = waveguide( e, u, h, w )
% solves for the values of kz which solve a given waveguide
% geometry
% e-----relative permitvity of each layer
% u-----relative permeability of each layer

n=sqrt(e.*u); %calculates the index of each layer
a=200000; %sets up number of divisions to create

kzmin=2*pi*min(n)./(w*1e-6); %min value of kz that needs to
be checked
kzmax=2*pi*max(n)./(w*1e-6); %max value of kz that needs to
be checked
kzinc=(kzmax-kzmin)/a; %checks a points

k0z=zeros(1, a+1); %sets up matrix of kz points to check
b11=zeros(1,length(k0z)); %sets up empty array of b11
lkz=length(k0z)-1; %length of the kz vector minus 1
for i=1:lkz
    k0z(i)=kzmin+(i-1)*kzinc;
    b11(i)=tmm(e, u, h, k0z(i), w);
end
figure (1);
semilogy(real(k0z),abs(b11)); %plots b11 as a function of
k0z
xlim([kzmin kzmax]);

%====Calculates all times where b11 is approximately
zero=====
j=0; %starts with no points
minz=k0z(1);
for i = 2:lkz

```

```

        if (abs(b11(i-1))>abs(b11(i)) &
abs(b11(i+1))>abs(b11(i)) & b11(i)<0.01)
            minz(j+1)=k0z(i);
            j=j+1;
        end
    end
end

end

```

Transfer Matrix Method Solver

```

function [ b11 ] = tmm( e, u, h, k0z, w)
%TMM Transfer Matrix Method implementation method for an arbitrary
%number of layers at angle a, and wavelength w

%takes in e-relative permittivity in each layer
%    u-relative permeability in each layer
%    h-thickness of each layer (besides, first & last->assumed infinite
%    a- angle of incidence
%    w- wavelength- in micrometers
%for TM propagation, switch e and u

%=====Checks for properly formatted
inputs=====
%if (size(e,2) ~= size(u,2)) %checks that the length of e equals u, else quits
% return
%end
%if ((length(h)+2)~=length(e))%checks there is a thickness for all but end layers
% return
%end

%=====checks for how many layers there are,
etc=====
layers=length(e); %number of layers
middle=length(h); %number of sandwiched layers
waves=length(w); %number of wavelengths

%=====calculates constants in each
layer=====
%e=e+0.75;
n=sqrt(e.*u); %defined refractive index of all layers

```

```

k0=2*pi.*n(1)./(w*1e-6); %defines wavevector in first layer

c=3e8*1e6; %speed of light in um/s
f=c./w; %frequency in hz
ww=2*pi*f; %angular frequency

kx=sqrt(ww.^2.*n.^2./3e8.^2-k0z.^2); %calculates kx in each layer

%=====sets up starting matrix (identity matrix)=====
AB=eye(2); %returns 2x2 identity matrix
AB0=AB;

%=====calculates propagation through all layers except last interface=====
if (length(e)~=2) %if there are more than 2 layers
    for i=1:length(e)-2 %for all but the last interface
        P=u(i)*kx(i+1)./u(i+1)./kx(i);
        T12=1/2*[1+P 1-P; 1-P 1+P];
        P2=[exp(-1i.*kx(i+1)*h(i)*1e-6) 0; 0 exp(1i*kx(i+1)*h(i)*1e-6)];
        M=T12*P2;
        AB=AB0*M;
        AB0=AB;
    end
end

%=====calculates reflections at the final interface=====
P=u(layers-1).*kx(layers)./u(layers)./kx(layers-1);
T12=1/2*[1+P 1-P; 1-P 1+P];

AB=AB0*T12;

%=====returns the value of
b11=====
b11=AB(1,1);

end

```

Plots mode profile given a value of kz and a structure
ONLY works for dielectrics, separate program for METALS

```

function [ a ] = Eplotter_Mod( n1, h, min,w, activ )
%Plots electric field profile,
%n1----list of indices for each layer

```



```

%h-----list of sandwiched layer thicknesses
%min---a value of kz solving the waveguide conditions
%w-----wavelength in microns

%=====Constant
Calcultions=====

Divisions=20000; %how thick to make each layer when
dividing structure
%equal to lum/Divisions, for example if Divisions=1000=>
matlab will divide
%divisions into 1 nm thick slices.
Cladding=1; %thickness to plot cladding in microns
c=3e8*1e6; %speed of light in um/s
f=c./w; %frequency in hz
ww=2*pi*f; %angular frequency
k0=ww/3e8; %wavevector in free space
neff=abs(min)./k0 %neff given the value of kz and k0
d1= [Divisions*Cladding h*Divisions Divisions*Cladding];
%adds cladding to list of thickness

%=====Divides struction into many thin
layers=====
m=0;
for i=1:size(d1,2)
    for j=1:d1(i)
        n(m+1)=n1(i);
        d(m+1)=1e-6/Divisions;
        active(m+1)=activ(i);
        m=m+1;
    end
end

%=====Sets up Boundary
Conditions=====
l=size(d,2);%number of layers (total thickness in nm)
z=1:l;%array of numbers from 1 to l
A=zeros(1,l); %coefficient in positive propagating
wavefunction, sets all to zero
B=A; %coefficient in negatvie propagating wavefunction
phi=A; %wavefunction
phi_d=A; %derivative of the wavefunction
A(1)=1; %sets intial positive to 1
B(1)=0; %sets initial negative to 0
phi(1)=1; %sets E=1 in the first layer

```

```

k=k0*sqrt((neff^2-n.^2)); %sets up the wavevector in each
layer
phi_d(1)=k(1); %sets up the derivative of phi in each layer

%=====Calculates the electric field in each
layer=====
for i=2:l; %start with layer 2, 1st layer is arbitrary set
to 1
    A(i)=(phi(i-1)+phi_d(i-1)/k(i))/2; %calculates A
from previous phi
    B(i)=(phi(i-1)-phi_d(i-1)/k(i))/2; %calculates B
from previous phi
    phi(i)=A(i)*exp(k(i)*d(i))+B(i)*exp(-k(i)*d(i));
%calculates E
    phi_d(i)=A(i)*k(i)*exp(k(i)*d(i))-B(i)*k(i)*exp(-
k(i)*d(i));
end

plot((z/Divisions*1000),phi/max(phi)); %plots the electric
field mode profile

%E==energy in the formula below, phi==electric field, sorry
for the
%confusing notaion

%Power is equal to electric field squared dived by two
times the impedance
%of that layer-----P=E^2./2(eta)
%Since the permeability is equal to 1, eta is proportional
to 1/n where n
%is the index so P is porportional to n*E^2

    QW=0; %energy confined to active region, starts sum at
zero for 1st layer
    for i=2:l
        E(i)=n(i)*phi(i).^2;
        if active(i-1) %if active region, count for
confinement factor
            QW=QW+E(i); %add to previous result
        end
    end
    Total=sum(E);
    confinement=QW/Total

```

```
a=confinment;  
mode=[ (z/Divisions*1000)' phi'/max(phi)];  
csvwrite('Mode_Output.csv', mode);  
end
```

BIBLIOGRAPHY

BIBLIOGRAPHY

- [1] G. Moore, *IEEE IEDM Tech Digest*, p.11 (1975).
- [2] L. Pavesi, D.J. Lockwood, “Silicon Photonics” *Springer* (2004).
- [3] R. Soref, *IEEE Select. Quant. Electron.*, **12**, 1678 (2006).
- [4] B. Jalali and S. Fathpour, *J. Lightwave Tech.*, **24**, 4600 (2006).
- [5] G.T.Reed, and A. P. Knights, Willy Online Library (2008). <http://onlinelibrary.wiley.com/doi/10.1002/9780470994535.fmatter/pdf>
- [6] K. F. MacDonald and N. I. Zheludev, *Laser & Photonics Reviews* **4**, 562 (2010).
- [7] Y. Vlasov, W. M. J. Green, and F. Xia, *Nat Photon* **2**, 242 (2008).
- [8] P. Gourley, J. Hendricks, A. McDonald, R. Copeland, K. Barrett, C. Gourley, and R.Naviaux, *Biomedical Microdevices* **7**, 331 (2005).
- [9] I. A. Young, E. M. Mohammed, J. T. S. Liao, A. M. Kern, S. Palermo, B. A. Block, M. R. Reshotko, and P. Chang, *IEEE Comm. Mag.*, **48**, 184 (2010).
- [10] ITRS-Roadmap Requests Additional Research in Alternative Interconnect Options, www.itrs.net
- [11] J. P. Van der Ziel, R. Dingle, R. C. Miller, W. Wiegmann, and W. A. Nordland Jr., *Appl. Phys. Lett.*, **26**, 463(1975).
- [12] R. D. Dupuis, P. D. Dapkus, N. Holonyak Jr., E. A. Rezek, and R. Chin, *Appl. Phys. Lett.*, **32**, 295 (1978).
- [13] J. Yang, “High-performance quantum dot lasers and integrated guided-wave devices on silicon”. Online at http://deepblue.lib.umich.edu/bitstream/handle/2027.42/60821/junyang_1.pdf?sequence=1
- [14] A. I. Ekimov and A. A. Onushchenko, *JETP Lett.*, **34**, 345 (1981).
- [15] Y. Arakawa and H. Sakaki, *Appl. Phys. Lett.*, **40**, 939(1982).

- [16] M. Asada, Y. Miyamoto, and Y. Suematsu, *IEEE J. Quantum Electron.*, **22**, 1915 (1986).
- [17] M. Sugawara, *Self-Assembled InGaAs/GaAs Quantum Dots.*, Academic Press, (1999).
- [18] I.R. Sellers, H.Y. Liu, K.M. Groom, D.T. Childs, D.Robbins, T.J. Badcock, M.Hopkinson, D.J. Mowbary and M.S. Skolnick, *Electron. Lett.*, **40**, 1412 (2004).
- [19] D.G. Deppe, K. Shavritranuruk, G. Ozgur, H. Chen, and S. Freisem, *Electron Lett.*, **45**, 154, (2009).
- [20] M. Asada, Y. Miyamoto, and Y. Suematsu, *IEEE J. Quantum Electron.*, **22**, 1915 (1986).
- [21] S. Fathpour, Z. Mi, P. Bhattacharya, A. R. Kovsh, S. S. Mikhrin, I. L. Krestnikov, A. V. Kozhukhov, and N. N. Ledentsov, *Appl. Phys. Lett.*, **85**, 5164 (2004).
- [22] S. Fathpour, Z. Mi, and P. Bhattacharya, *J. Appl. Phys. D: Appl. Phys.*, **38**, 2103 (2005).
- [23] N. Kirstaedter, N. N. Ledentsov, M. Grundmann, D. Bimberg, V. M. Ustinov, S. S. Ruvimov, M. V. Maximov, P. K. Kop'ev, Zh. I. Alferov, U. Richter, P. Werner, U. Gosele, and J. Heydenreich, *Electron. Lett.*, **30**, 1416 (1994).
- [24] K. Kamath, P. Bhattacharya, T. Sosnowski, T. Norris, and J. Phillips, *Electron. Lett.*, **32**, 15, 1374 (1996).
- [25] S. Ghosh, S. Pradhan, and P. Bhattacharya, *Appl. Phys. Lett.*, **81**, 3055 (2002).
- [26] G. T. Liu, H. Li, K. J. Malloy, and L. F. Lester, *Electron. Lett.*, **35**, 1163 (1999).
- [27] H. C. Sun, L. Davis, S. Sethi, J. Singh, and P. Bhattacharya, *IEEE Photon. Techn. Lett.*, **5**, 870 (1993)
- [28] M. Geiger, A. Bauknecht, F. Adler, H. Schweizer, F. Scholz, *J. Crystal Growth* **170**, 558 (1997).
- [29] P. Bhattacharya, S. Ghosh, S. Pradhan, J. Singh, Z.-K. W u, J. Urayama, K. Kim, and T. B. Norris, *IEEE J. Quantum Electron.*, **39**, 952 (2003).
- [30] D. Klotzkin, K. Kamath, K. Vineberg, P. Bhattacharya, R. Murty, and J. Laskar, *IEEE Photonic. Tech. Lett.* **10**, 932 (1998).
- [31] D. G. Deppe and D. L. Huffaker, *Appl. Phys. Lett.* **77**, 3325 (2000).
- [32] O. B. Shchekin and D. G. Deppe, *Appl. Phys. Lett.* **80**, 3277 (2002).
- [33] Y. Miyamoto, Y. Miyake, M. Asada, and Y. Suematsu, *IEEE J. Quantum*

- Electron.*, **25**, 2001 (1989).
- [34] L. Asryan, and S. Luryi, *IEEE Journal of Quantum Electronics*, **37**, 905 (2001).
- [35] P. Bhattacharya and S. Ghosh, *Appl. Phys. Lett.*, **80**, 3482 (2002).
- [36] P. Bhattacharya, S. Ghosh, S. Pradhan, J. Singh, Z.-K. Wu, J. Urayama, K. Kim, and T. B. Norris, *IEEE J. Quantum Electron.*, **39**, 952 (2003).
- [37] D. G. Deppe, H. Huang, and O. B. Shchekin, *IEEE J. Quantum Electron*, **38**, 1587 (2002).
- [38] M. Gioannini, *Proc. SPIE*, **5452**, 526 (2004).
- [39] T. Kipp, H. Welsch, Ch. Strelow, Ch. Heyn, and D. Heitmann, *Phys. Rev. Lett.* **96**(7), 077403 (2006).
- [40] S. Mendach, S. Kiravittaya, A. Rastelli, M. Benyoucef, R. Songmuang, and O. G. Schmidt, *Phys. Rev. B* **78**, 035317 (2008).
- [41] S. Vicknesh, F. Li, and Z. Mi, *Appl. Phys. Lett.* **94**(8), 081101 (2009).
- [42] Li, Z. T. Mi, and S. Vicknesh, *Opt. Lett.* **34**(19), 2915–2917 (2009).
- [43] Li and Z. T. Mi, *Opt. Express* **17**(22), 19933–19939 (2009).
- [44] Z. Tian, F. Li, Z. T. Mi, and D. V. Plant, *IEEE Photon. Technol. Lett.* **22**(5), 311–313 (2010).
- [45] C. Deneke, A. Malachias, S. Kiravittaya, M. Benyoucef, T. H. Metzger, and O. G. Schmidt, *Appl. Phys.* **96**, 143101 (2010).
- [46] V. Prinz, V. Seleznev, A. Gutakovskiy, A. Chehovskiy, V. Preobrazhenskii, M. Putyato, and T. Gavrilova, *Phys. E* **6**(1-4), 828–831(2000).
- [47] U. Koren, B. I. Miller, Y. K. Su, T. L. Koch, and J. E. Bowers, *Appl. Phys. Lett.*, **51**, 1744 (1987).
- [48] Peter J. A. Thijs, Luuk F. Tiemeijer, P. I. Kuindersma, J.J. M. Binsma, and Teus Van Dongen, *J. Quant. Electron.*, **21**, 1426 (1991).
- [49] S. J. Caracci, M. R. Krames, N. Holonyak, M. J. Ludowise, and A. FischerColbrie, *J. Appl. Phys.*, **75**, 2706 (1994).

- [50] Xiang Zhu, Daniel T. Cassidy, Michael J. Hamp, D. A. Thompson, B. J. Robinson, Q. C. Zhao, and M. Davies, *Photon. Tech. Lett.*, **9**, 1202 (1997).
- [51] B. I. Miller, U. Koren, M. G. Young, and M. D. Chien, *Appl. Phys. Lett.*, **58**, 1952 (1991).
- [52] D. I. Babic, K. Streubel, R. P. Mirin, N. M. Margalit, J. E. Bowers, E.L. Hu, D. E. Mars, L. Yang, and K. Carey, *Photon Tech. Lett.*, **7**, 1225 (1995).
- [53] P. Bhattacharya, J. Singh, H. Yoon, X. Zhang, A. Gutierrez-Aitken, and Y. Lam, *J. Quant. Electron.*, **32**, 1620 (1996).
- [54] C. Gilfert, E.-M. Pavelescu, and J. P. Reithmaier, *Appl. Phys. Lett.*, **96**, 191903 (2010).
- [55] C. Gilfert, V. Ivanov, N. Oehl, M. Yacob, and J. P. Reithmaier, *Appl. Phys. Lett.*, **98**, 201102 (2011).
- [56] V. Ivanov, C. Gilfert, F. Schnabel, A. Rippien, J.P. Reithmaier, D. Gready, G. Eisenstein, C. Bornholdt, *Proc. Semiconductor Laser Conference*, 1 (2012).
- [57] P. R. Berger, K. Chang, P. Bhattacharya, J. Singh and K. K. Bajai, *Appl. Phys. Lett.*, **53**, 684 (1988).
- [58] D. Leonard, M. Krishnamurthy, C. M. Reaves, S. P. Denbaars, and P. M. Petroff, *Appl. Phys. Lett.*, **63**, 3203 (1993).
- [59] J. Pamulapati, P. K. Bhattacharya, J. Singh, P. R. Berger, C. W. Snyder, B. G. Orr, R. L. Tober, *J. Electron. Mater.*, **25**, 479 (1996).
- [60] F. C. Frank, and J. H. van der Merwe, *Proceedings of Royal Society of London A*, **198**, 205 (1949).
- [61] I. N. Stranski, and L. Krasranow, *Abt. Iib.*, Band, **146**, 146 (1937).
- [62] M. Volmer, and A. Weber, *Z. Phys. Chem.*, **119**, 277 (1926).
- [63] Pimpinelli, Alberto; Jacques Villain (1998). *Physics of Crystal Growth*. Cambridge: Cambridge University Press.

- [64] Oura, K.; V.G. Lifshits, A.A. Saranin, A.V. Zotov, and M. Katayama (2003). *Surface Science: An Introduction*. Berlin: Springer.
- [65] Markov, Ivan V. (1995). *Crystal Growth for Beginners: Fundamentals of Nucleation, Crystal Growth, and Epitaxy*. Singapore: World Scientific.
- [66] R. H.Wang, A. Stintz, P. M.Varangis, T. C. Newell, H. Li, K. J. Malloy, and L. F. Lester, *Photon. Tech. Lett.*, **13**, 767 (2001).
- [67] L. Gonzalez, J. M. Garcia, R. Garcia, F. Briones, J. Martinez-Pastor, and C. Ballesteros, *Appl. Phys. Lett.*, **76**, 1104 (2000).
- [68] Ralf Blossey, and Axel Lorke, *Phys. Rev. E*, **65**, 021603 (2002)
- [69] D. Granados and J. M García, *Appl. Phys. Lett.* **82**, 2401 (2003)
- [70] H. S. Ling, and C. P. Lee, *J. Appl. Phys.* 102, 024314 (2007)
- [71] H. S. Ling, S. Y. Wang, C. P. Lee, and M. C. Lo, *J. Appl. Phys.* **105**, 034504 (2009).
- [72] P.H. Seigel, *IEEE Trans. Microwave Theory Tech.*, **50**, 910 (2002).
- [73] Y. C. Shen, T. Lo, P. F. Taday, B. E. Cole, W. R. Tribe, and M. C. Kemp, *Appl. Phys. Lett.* **86**, 241116 (2005).
- [74] P. H. Siegel, *IEEE Trans. Antennas and Propagation.* **55**, 2957 (2007).
- [75] M. B. M. Rinzan, A. G. U. Perera, S. G. Matsik, H. C. Liu, Z. R. Wasilewski, and M. Buchanan, *Appl. Phys. Lett.* **86** (8), 71112 (2005).
- [76] H. Luo, H. C. Liu, C. Y. Song, and Z. R. Wasilewski, *Appl. Phys. Lett.* **86** (23), 231103 (2005).
- [77] D. Pan, E. Towe, and S. Kennerly, *Appl. Phys. Lett.* **73**, 1937 (1998).
- [78] S. Krishna, S. Raghavan, G. Winckel, A. Stintz, G. Ariyawansa, S. G. Matsik and A. G. U. Perera, *Appl. Phys. Lett.* **83** (14), 2745 (2003).
- [79] J.C. Campbell and A. Madhukar, *Proc. IEEE*, **95** (9), 1815 (2007).
- [80] G. Huang, J. Yang, P. Bhattacharya, G. Ariyawansa, and A.G.U. Perera, *Appl. Phys. Lett.* **92**, 011117 (2008).
- [81] G.Huang, W. Guo, P. Bhattacharya, G. Ariyawansa, and A. G. U. Perera, *Appl. Phys. Lett.* **94**, 101115 (2009).
- [82] A. G. U. Perera, G. Ariyawansa, G. Huang, P. Bhattacharya, *Infrared Phys. Tech.* **52**, 252 (2009)
- [83] A. Lorke, R. J. Luyken, J. M. Garcia, and P. M. Petroff, *Jpn. J Appl. Phys I*, **40**, 1857 (2001).

- [84] D. Granados and J. M. Garcia, *Appl. Phys. Lett.* **82**, 2401 (2003).
- [85] A.D. Stiff, S. Krisna, P. Bhattacharya, and S.W. Kennerly, *IEEE Journal of Quantum Electronics*, **37** (11), 1412 (2001).
- [86] C.H. Lin, H.S. Lin, C.C. Huang, S.K. Su, S.D. Lin, K.W. Sun, C.P. Lee, Y.K. Liu, M.D. Yang, and J.L. Shen, *Appl. Phys. Lett.* **94**, 183101 (2009).
- [87] A. D. Englund, and J. Vuckovic, *Nat. Phys.* **2**(7), 484–488 (2006).
- [88] Q. Song, H. Cao, S. T. Ho, and G. S. Solomon, *Appl. Phys. Lett.* **94**(6), 061109 (2009).
- [89] S. Reitzenstein, A. Bazhenov, A. Gorbunov, C. Hofmann, S. Munch, A. Löffler, M. Kamp, J. Reithmaier, V. Kulakovskii, and A. Forchel, *Appl. Phys. Lett.* **89**(5), 051107 (2006).
- [90] C. Deneke and O. G. Schmidt, *Appl. Phys. Lett.* Vol **85** (10), 2004.
- [91] S. Mendach, R. Songmuang, S. Kiravittaya, A. Rastelli, M. Benyoucef, and O. Schmidt, *Appl. Phys. Lett.* **88**(11), 111120 (2006).
- [92] M. Hosoda and T. Shigaki, *Appl. Phys. Lett.* **90**, 181107 (2007).
- [93] C. Strelow, H. Rehberg, C. M. Schultz, H. Welsch, Ch. Heyn, D. Heitmann, and T. Kipp, *Phys. Rev. Lett.* **101**, 127403 (2008).
- [94] Dikshit, and J.M Pikal, *IEEE J. Quant. Elec.* **40**, 105 (2004).
- [95] Akira Sakamoto, and M. Sugawaraet, *IEEE Photon. Technol. Lett.* **12**, 107 (2000).
- [96] Park, O.B. Shchekin, and D.G Deppe, *IEEE J. Quant. Elec.* **36**, 1065 (2000).
- [97] Y. Takuma, M. Miyagi, and S. Kawakami, *Appl. Opts.* **20**, 2291 (1981).
- [98] P. G. Suchoski, Jr. and V. Ramaswamy, *J. Opt. Soc. Am. A* **1**, 754 (1984).
- [99] E. A. J. Marcatili, *The Bell Sys. Tech. Journal*, 2071 (1969).
- [100] R. A. Bergh, G. Kotler, and H. J. Shaw, *Electron. Lett.*, **16**, 260 (1980).
- [101] R.C. Alfarness and R.V. Schmidt, *Appl. Phys. Lett.*, **33**, 161 (1978).
- [102] J. C. Campbell, F. A. Blum, D. W. Shaw, and K. L. Lawley, *Appl. Phys. Lett.*, **27**, 202, (1975).
- [103] B. J. Luff, R. D. Harris, J. S. Wilkinson, R. Wilson and D. J. Schiffrin, *Opt. Lett.*, **21**, 618 (1996).

- [104] H. Inoue, K. Hiruma, K. Ishida, H. Sato, and H. Matsumura, *Appl. Opts.*, **25** (9), 1484 (1986).
- [105] M. Papuchon, Y. Combemale, X. Mathieu, D. B. Ostrowsky, L. Reiber, A. M. Roy, B. Sejourne, and M. Werner, *Appl. Phys. Lett.*, **27**, 289 (1975).
- [106] O.G.Schmidt, C. Deneke, S. Kiravittaya, R. Songmuang, H. Heidemeyer, Y. Nakamura, R. Zapf-Gottwick, C. Muller, and N. Y. Jin-Phillipp, *IEEE J. Sel. Top. Quant. Electron.* **8**, 1025 (2002).
- [107] G. Huang, Y. Mei, D. J. Thurmer, E. Coric and O. G. Schmidt, *Lab Chip*, **9**, 263 (2009).
- [108] C. C. B. Bufon, J. D. C. Gonzalez, D. J. Thurmer, D. Grimm, M. Bauer, and O. G. Schmidt, *Nano Lett.*, **10**, 2506 (2010).
- [109] Y. Mei, A. A. Solovev, S. Sanchez and O. G. Schmidt, *Chem. Soc. Rev.*, **40**, 2109 (2011).
- [110] E. J. Smith, S. Schulze, S. Kiravittaya, Y. Mei, S. Snchez, and O. G. Schmidt, *Nano Lett.*, **11**, 4037 (2011).
- [111] M. Kuno, T. Sanada, H. Nobuhara, M. Makiuchi, T. Fujii, O. Wada, and T. Sakurai, *Appl. Phys. Lett.*, **49**, 1575 (1986).
- [112] Y. Hasumi, A. Kozen, J. Temmyo, and H. Asahi, *Elect. Dev. Lett.*, **8**, 10 (1987).
- [113] L. M. Lunardi, S. Chandrasekhar, A. H. Gnauck, C. A. Burrus, R. A. Hamm, J. W. Sulhoff, and J. L. Zyskind, *Photon. Tech. Lett.*, **7**, 182 (1995)
- [114] L. M. Lunardi, S. Chandrasekhar, A. H. Gnauck, C. A. Burrus, and R. A. Hamm, *Photon. Tech. Lett.*, **7**, 1201 (1995).

- [115] K. Yang, A. L. Gutierrez-Aitken, X. Zhang, G. I. Haddad, and P. Bhattacharya, *J. Lightwave Tech.*, **14**, 1831 (1996).
- [116] K. Beyzavi, D. Kim, C. Chao, P. Burrows, and S. Forrest, *Photon. Tech. Lett.*, **7**, 1162 (1995).
- [117] T. K. Woodward, A. V. Krishnamoorthy, A. L. Lentine, K. W. Goossen, J. A. Walker, J. E. Cunningham, W. Y. Jan, L. A. D'Asaro, L. M. F. Chirovsky, S. P. Hui, B. Tseng, D. Kossives, D. Dahringer, and R. E. Leibenguth, *Photon. Tech. Lett.*, **8**, 422 (1996).
- [118] O. Qasaimeh, W. Zhou, P. Bhattacharya, D. Huffaker, and D. G. Deppe, *J. Lightwave Tech.*, **4**, 546 (2001).
- [119] J. Shin, P. Bhattacharya, J. Xu, and G. Varo, *Opt. Lett.* **30**, 335 (2005).
- [120] J. Heo, S. Bhowmick, and P. Bhattacharya, *J. Quantum Electron.*, **48**, 927 (2012).
- [121] C. C. B. Bufon, J. D. C. Gonzalez, D. J. Thurmer, D. Grimm, M. Bauer, and O. G. Schmidt, *Nano Lett.*, **10**, 2506 (2010).
- [122] E. J. Smith, S. Schulze, S. Kiravittaya, Y. Mei, S. Sanchez, and O. G. Schmidt, *Nano Lett.*, **11**, 4037 (2011).
- [123] S. Bhowmick, J. Heo, and P. Bhattacharya, *Appl. Phys. Lett.* **101**, 171111 (2012).
- [124] V. M. Ustinov, N. A. Maleev, A. E. Zhukov, A. R. Kovsh, A. Yu. Egorov, A. V. Lunev, B. V. Volovik, I. L. Krestnikov, Yu. G. Musikhin, N. A. Bert, P. S. Kop'ev, Z. I. Alferov, N. N. Ledentsov) and D. Bimberg, *Appl. Phys. Lett.*, **74**, 192815 (1999).
- [125] O. B. Shchekin and D. G. Deppe, *Photon. Tech. Lett.*, **14**, 1231 (2002).

- [126] P. K. Kondratko, S. L. Chuang, G. Walter, T. Chung, and N. Holonyak, *Appl. Phys. Lett.*, **83**, 4818 (2003).
- [127] S. Fathpour, Z. Mi, P. Bhattacharya, A. R. Kovsh, S. S. Mikhlin, I.L. Krestnikov, A. V. Kozhukhov, and N. N. Ledentsov, *Appl. Phys. Lett.*, **85**, 5164 (2004).
- [128] S. Fathpour, Z. Mi, and P. Bhattacharya, *J. Phys. D: Appl. Phys.*, **38**, 2103 (2005).
- [129] Z. Mi, P. Bhattacharya, and S. Fathpour, *Appl. Phys. Lett.*, **86**, 153109 (2005).
- [130] Y. Tanaka, K. Takada, M. Ishida, Y. Nakata, T. Yamamoto, M. Yamaguchi, K. Nishi, M. Sugawara, Y. Arakawa, *Communications and Photonics Conference and Exhibition (ACP), 2010 Asia*, 577 (2010).
- [131] L. Gonzalez, J. M. Garcia, R. Garcia, F. Briones, J. Martinez-Pastor, and C. Ballesteros, *Appl. Phys. Lett.*, **76**, 1104 (2000).
- [132] R. H. Wang, A. Stintz, P. M. Varangis, T. C. Newell, H. Li, K. J. Malloy, and L. F. Lester, *Photon. Tech. Lett.*, **13**, 767 (2001).
- [133] H. Dery and G. Eisenstein, *J. Quant. Electron.*, **40**, 1398 (2004).
- [134] M. Gioannini, *Proc. SPIE*, 526 (2004)
- [135] P. Caroff, C. Paranthoen, C. Platz, O. Dehaese, H. Folliot, N. Bertru, C. Labbé, R. Piron, E. Homeyer, A. Le Corre, and S. Loualiche, *Appl. Phys. Lett.*, **87**, 243107 (2005).
- [136] J. P. Reithmaier, A. Somers, S. Deubert, R. Schwertberger, W. Kaiser, A. Forchel, M. Calligaro, P. Resneau, O. Parillaud, S. Bansropun, M. Krakowski, R. Alizon, D. Hadass, A. Bilenca, H. Dery, V. Mikhelashvili, G. Eisenstein, M.

- Gioannini, I. Montrosset, T. W. Berg, M. van der Poel, J. Mørk, and B. Tromborg, *J. Phys. D: Appl. Phys.*, **38**, 2088 (2005).
- [137] D. Hadass, V. Mikhelashvili, G. Eisenstein, A. Somers, S. Deubert, W. Kaiser, J. P. Reithmaier, A. Forchel, D. Finzi, and Y. Maimon, *Appl. Phys. Lett.*, **87**, 021104 (2005).
- [138] J. H. Wei and K. S. Chan, *J. Appl. Phys.*, **97**, 123524 (2005).
- [139] Zetian Mi and Pallab Bhattacharya, *IEEE J. Quan. Electron.*, 1224 (2006).
- [140] I.P. Marko, S.J. Sweeney, A.R. Adams, S.R. Jin, B.N. Murdin, R. Schwertberger, A. Somers, J.P. Reithmaier, and A. Forchel, *Phys. Stat. Sol. (b)*, **241**, 3427 (2004).
- [141] F. Ielarge, B. Rousseau, B. Dagens, F. Poingt, F. Pommereau, and A. Accard, *Photon. Tech. Lett.*, **17**, 1369 (2005).
- [142] X. Zhang, A. Gutierrez-Aitken, D. Klotzkin, P. Bhattacharya, C. Caneau, and R. Bhat, *J. Select. Quan. Electron*, **3**, 309 (1997).
- [143] B. W. Hakki and T. L. Paoli, *J. Appl. Phys.*, **46**, 1299 (1975).
- [144] V. Sichkovskiy, V. Ivanov, J. P. Reithmaier, *Proc. SPIE*, **8640**, 864004 (2013).
- [145] N. A. Jahan, C. Hermannstädter, J.H. Huh, H. Sasakura, T. J. Rotter, *J. Appl. Phys.* **113**, 033506 (2013).
- [146] M. Sugawara, N. Hatori, M. Ishida, H. Ebel, Y. Arakawa, T. Akiyama, K. Otsubo, T. Yamamoto, and Y. Nakata, *J. Phys. D: Appl. Phys.*, **38** 2126 (2005).
- [147] T. C. Newell, D. J. Bossert, A. Stintz, B. Fuchs, K. J. Malloy, and L. F. Lester, *Photon. Tech. Lett.* **11**, 1527 (1999).
- [148] Y. Miyake and M. Asada, *Jpn. J. Appl. Phys.*, **28**, 1280 (1989).

- [149] P. J. A. Thijs, T. Dongen, L. F. Tiemeijer, and J. J. M. Binsma, *J. Lightw. Technol.*, **12**, 28 (1994).